



Uio • University of Oslo

Using MicMac to determine JRC of rock joints

Tord Buvik

Thesis for the degree of Master in Geohazards and
Geomechanics

60 credits

Department of Geosciences

Faculty of mathematics and natural sciences

University of Oslo

15 August 2021

Abstract

The aim of this thesis is to examine the viability of using the open-source photogrammetry software MicMac to determine the JRC value of rock joints. This was done by imaging both plaster molds of a sandstone joint and real sandstone samples, before and after the samples were put through a shear test. A total of 27 samples was imaged and then sheared (20 plaster samples and 7 sandstone samples).

Using MicMac DEMs were created for the samples and then profiles in the direction of shear was extracted using MATLAB. JRC values were then determined for these profiles using statistical parameters such as Z_2 , SF and R_p . These JRC values were then compared to JRC values derived from back calculations from the shear test results using the formula devised by Barton.

Comparing the back calculated JRC values with the JRC values derived from the DEMs, it appears that the DEM derived JRC values generally underestimated the JRC value for the majority of the samples

Unfortunately, due to issues encountered with the z-axis scaling of the DEMs, most likely caused by inconsistencies with the lighting used during image acquisition, it proved impossible to accurately determine the viability of using MicMac in determining joint JRC. There was also issues with the plaster samples when shearing. Due to what seem like insufficient drying time the samples exhibited stick-slip behavior just before and after reaching peak shear stress, leading to some uncertainty around the back calculated JRC values as well.

Acknowledgements

I would like to express my deep gratitude to my supervisors, Francois Renard (UiO), Bahman Bohloli (NGI), and Halvard Smith (NGI) for their guidance and advice throughout the process of creating this work. A special thanks to Halvard Smith for his help getting me up to speed with the equipment in the NGI lab. Thanks also to the team in the NGI lab for their warm welcome and for making me feel a little less like an outsider.

A special thanks also to my parents for their support throughout this period.

Contents

Abstract	i
Acknowledgements	iii
Contents	v
Figure List	viii
Table List.....	xi
1.0 Introduction	1
2.0 Background	2
2.1 Joint Roughness.....	2
2.1.1 Patton (1966)	2
2.1.2 Barton-Bandis.....	2
2.1.3 The impact of joint scale	4
2.2 Other ways to quantify joint roughness.....	5
2.2.1 Statistical	5
2.2.2 Fractals	6
2.2.3 3D roughness.....	7
2.3 Ways of recording surface roughness	9
2.3.1 Mechanical	9
2.3.2 Surface recording	9
2.3.3 3D	10
2.4 Photogrammetry	11
2.4.1 Error sources	11
3.0 Methods.....	13
3.1 Sample preparation.....	13
3.1.1 Plaster	13

3.1.2 Sandstone	14
3.2 Uniaxial tests	15
3.2.1 Plaster	15
3.2.2 Sandstone	16
3.3 Shear test	17
3.3.1 Shear-test sample preparation	17
3.4 Shear-box testing	17
3.4.1 Consolidation	17
3.4.2 Shear test	18
3.5 Photogrammetry	19
3.5.1 Image collection & image settings	19
3.5.2 MicMac workflow	20
3.6 Data processing	22
3.6.1 Loading DEMs and selecting profiles	22
3.6.2 Calculating Z_2 , SF & R_p	23
3.6.3 Calculating JRC	23
4.0 Data	25
4.1 Uniaxial	25
4.2 Shear tests	26
4.3 JRC	29
4.4 Anisotropy	32
4.5 Photogrammetry	33
5.0 Discussion	35
5.1 Issues with the shear tests	35
5.2 Issues with the photogrammetry	37
6 Conclusions	38
References	39

Appendix I: Surface profiles in shear direction 42

Figure List

Figure 1: Profiles used to estimate JRC values. from Barton & Choubey (1977).	4
Figure 2: ATS measuring head. The projector can be seen in the middle, flanked by the two cameras. Image from (Grasselli, 2001).	10
Figure 3: a) The beta sandstone, with what appears to be a compaction band running through it. b) The alpha sandstone.....	14
Figure 4: Figure showing how the samples were mounted for shear testing.	17
Figure 5: Shear box used for shear testing. the image on the left shows the horizontal and vertical LVDT sensors. In the image on the right the entire shear box setup can be seen. The lever arm used to apply the normal load can be seen in the bottom half of the image.	18
Figure 6: Setup used to collect photogrammetry data. the setup consisted of a digital camera mounted perpendicular to the sample surface. An additional light, mounted at a 45 degree angle to the sample, was needed to ensure sufficient image quality.....	19
Figure 7: General workflow using MicMac	21
Figure 8: A) The area from which the surface profiles were extracted. B) Overview of the position of the created profiles. C) examples of the profiles created from the DEM. JRC a-g corresponds to formula 18-24 in order.	23
Figure 9: A) Compressive strength of the plaster samples. B) Compressive strength of the sandstone samples.	25
Figure 10: A) Figure shows the development of the shear stress on three plaster samples, at differing normal loads. all three samples had similar geometry and orientation. B) Similar to the previous figure, however, this time the normal load was kept the same across the three tests. C) Results of the shear tests using the alpha sandstone with differing normal loads. Sample SA1 and SA2 had a similar shape (Rounded) and Sample SA3 and SA4 had a similar shape (Rectangular). D) The shear test results using the beta sandstone, this time not varying the normal load.....	26
Figure 11: The shear stress results from all the plaster test performed at 1 MPa normal load, with each sample being rotated by 30 degrees from the previous test (except M1, M2, and M3, who all had the same orientation). A majority of the samples displayed a stick-slip like behavior during testing.....	27
Figure 12: The results from shear tests performed on two plaster samples with a very smooth surface. One of the samples was run three times consecutively.	28

Figure 13:a) The JRC back calculated from the shear tests compared to the JRC calculated from the photogrammetric data using the different formulas. B) The peak friction value and residual friction value for the rotational plaster tests.	32
Figure 14: Before and after 3D models of a plaster and sandstone sample created using MicMac.	33
Figure 15: A & B) Comparing the before (red) and after (green) 3D models of one of the plaster samples highlights a significant difference between the two models in the vertical axis. C) Measuring the distance between the two models using CloudCompares cloud distance tool.	34
Figure 16: A) The distance between the two models after defocusing and refocusing the lens focus. B) The distance when nothing was done to the camera.	35
Figure 17: M2 Profiles Bottom	42
Figure 18: M2 Profiles Top.....	43
Figure 19: M3 Profiles Bottom	44
Figure 20: M3 Profiles Top.....	45
Figure 21: Q1 Profiles Bottom.....	46
Figure 22: Q1 Profiles Top.....	47
Figure 23: R2 Profiles Bottom	48
Figure 24: R2 Profiles Top.....	49
Figure 25: S1 Profiles Bottom.....	50
Figure 26: S1 Profiles Top	51
Figure 27: T2 Profiles Bottom	52
Figure 28: T2 Profiles Top	53
Figure 29: U2 Profiles Bottom	54
Figure 30: U2 Profiles Top.....	55
Figure 31: V1 Profiles Bottom	56
Figure 32: V1 Profiles Top.....	57
Figure 33: W1 Profiles Bottom	58
Figure 34: W1 Profiles Top.....	59
Figure 35: X1 Profiles Bottom	60
Figure 36: X1 Profiles Top.....	61
Figure 37: Y1 Profiles Bottom	62
Figure 38: Y1 Profiles Top.....	63
Figure 39: Z1 Profiles Bottom	64

Figure 40: Z1 Profiles Top	65
Figure 41: ZZ1 Profiles Bottom	66
Figure 42: ZZ1 Profiles Top.....	67
Figure 43: Smooth plaster Profiles Bottom.....	68
Figure 44: Smooth plaster Profiles Top	69
Figure 45: SA1 Profiles Bottom.....	70
Figure 46: SA1 Profiles Top	71
Figure 47: SA2 Profiles Bottom.....	72
Figure 48: SA 2 Profiles Top	73
Figure 49: SA3 Profiles Bottom.....	74
Figure 50: SA3 Profiles Top	75
Figure 51: SB1 Profiles Bottom	76
Figure 52: SB1 Profiles Top.....	77
Figure 53: SB2 Profiles Bottom	78
Figure 54: SB2 Profiles Top.....	79
Figure 55: SB3 Profiles Bottom	80
Figure 56: SB3 Profiles Top.....	81

Table List

Table 1: List of photogrammetric error sources and their effect. (Dai et al., 2014)	13
Table 2: Summary of the sandstone samples	15
Table 3: Overview of the plaster samples used in the uniaxial tests. Drying times greater than 24 hours are an approx. estimate.	16
Table 4: Overview of the sandstone samples used in the uniaxial tests.....	16
Table 5: The different load steps used on the samples during the consolidation of the shear samples.	18
Table 6: Camera settings used during photogrammetry data collection.	20
Table 7: Overview of the jrc values for all the samples, part 1. * value either exceeded max jrc value of 20, or min value of 0. a-g corresponds to formula 18-24 in order.	30
Table 8: Overview of the jrc values, part 2. * value either exceeded max jrc value of 20, or min value of 0. a-g corresponds to formula 18-24 in order.....	31

1.0 Introduction

Determining the shear strength of the bedrock is of critical importance when one is building a dam or tunnel. The consequences of getting it wrong could potentially cost thousands of lives. Therefore a lot of work has been put into finding ways to quickly and cheaply determine the shear strength of rock joints. Initially the main way of finding the shear strength of joints involved performing tilt tests on rock samples, a method that was expensive both in terms of labor and money. Then along comes Barton and his Joint Roughness Coefficient (JRC), allowing determination of shear strength by comparing rock joints to 10 standard profiles. In the years since, JRC has become the dominating method to determine shear strength. However, the original process of comparing profiles did have one big drawback. It was done by eye, which meant that the accuracy of the estimate was heavily affected by the experience and judgment of the person doing the comparison.

Therefore, several authors throughout the years have come up with alternative ways to quantify the roughness of the profiles, whether through statistical means (Hsiung et al., 1993, Maerz et al., 1990, Tse and Cruden, 1979, Yu and Vayssade, 1991), using fractals (Brown and Scholz, 1985, Kulatilake et al., 1995, Lee and Juang, 1991), or even branching out into three-dimensions (Grasselli and Egger, 2003).

In addition to alternative ways of quantifying roughness, new ways of recording the surface were also devised. Using technologies like laser scanners, harnessing light to record surface topography (Huang et al., 1992, Lanaro, 2000), or using the lack of light to do the same (Maerz et al., 1990). Some however, chose to use a technique called photogrammetry. Photogrammetry uses a patchwork of overlapping images taken of a surface to create depth, in much the same way as our eyes allow us to have depth perception.

One of the big advantages that photogrammetry has over the other methods, is cost. While things like 3D laser scanners have gotten cheaper in the last few years, they still can cost thousands, if not tens of thousands of dollars. Photogrammetry on the other hand, can be done using relatively inexpensive consumer grade cameras and lenses, meaning that the cost of entry is far lower.

On the software side there are several options, like Autodesk ReCap. Of course, a lot of them also come with the drawback of licensing cost, and that is where MicMac comes in. MicMac

is an open source, free photogrammetry software developed by a joint effort of the IGN (French National Geographic Institute) and ENSG (French national school for geographic sciences) that has been used successfully in the past to explore other aspects of the earth sciences (Galland et al., 2016). It does not however, appear that anyone has tried using it to determine joint roughness.

And so that will be the goal of this thesis, employing MicMac on images taken of both artificial plaster joints and real sandstone joints in an attempt to determine the viability and accuracy of using MicMac to determine JRC.

2.0 Background

2.1 Joint Roughness

2.1.1 Patton (1966)

Using direct shear tests on plaster joints with different geometries. (F.D.Patton, 1966) used the following formula for the maximum strength envelope for the specimens.

$$\tau = \sigma_n \tan (\Phi_b + i) \quad (1)$$

Where τ is the shear stress, σ_n is the normal load, Φ_b is the basic angle of friction, and i is the angle of surface asperities. This formula was itself taken from the earlier work of (Newland and Allely, 1957).

Based on the results of the shear tests, Patton came to the following conclusions: The failure envelopes of the samples with irregular surfaces was curved. This curvature was caused by changes in the mode of failure involved. And these changes in the mode of failure was itself caused by the physical properties of the irregularities along the failure surface.

2.1.2 Barton-Bandis

A weakness in Patton's model is that it only allows a relatively low normal stress, based around the idea of the two halves of the joint sliding past each other. As the normal stress is increased however, this becomes gradually harder and harder to accommodate, and eventually the rock with shear brittlely.

To account for this behavior (Barton, 1973) proposed the following formula for the shear strength of saturated rock.

$$\tau / \sigma'_n = \tan \left[JRC \log_{10} \left(\frac{JCS}{\sigma'_n} \right) + \Phi_b \right] \quad (2)$$

Where JCS is the effective joint wall compressive strength, σ' is the effective normal stress, and JRC is the joint roughness coefficient. Barton concluded that JCS was equivalent of the compressive strength, σ_c , if the rock was unweathered, down to $\frac{1}{4}$ of σ_c if the rock is weathered. The JCS value of a sample can be easily determined using a Schmidt hammer. The advantage of (2) is that it can be used not only to fit data, but also to predict the peak shear strength of a sample.

The joint roughness coefficient was defined as a range of values from 0 to 20, used to quantify the roughness of a joint surface. The higher the value, the rougher the surface. Barton divided the JRC into three classes. Class A described the roughest joints and have a JRC value of 20. Class B joints are smoother and undulating and have a JRC value of 10. Class C joints describe the smoothest joints and have a JRC value of 5.

In (Barton and Choubey, 1977) the authors used data from 136 rock samples to further refine (2). They determined that for weathered and unweathered joints (2) could be expressed as.

$$\tau = \sigma_n \tan \left[JRC \log_{10} \left(\frac{JCS}{\sigma_n} \right) + \Phi_r \right] \quad (3)$$

Where Φ_r is the residual angle of friction, with the residual angle representing the minimum shear strength value for the joint. Φ_r can be found by.

$$\Phi_r = (\Phi_b - 20^\circ) + 20 (r/R) \quad (4)$$

Where r is the Schmidt rebound on a wet joint, and R is the Schmidt rebound on a dry joint.

Barton and Choubey also further refined the process for determining the JRC value of a joint by presenting 10 representative surface profiles for comparison (Fig. 1).

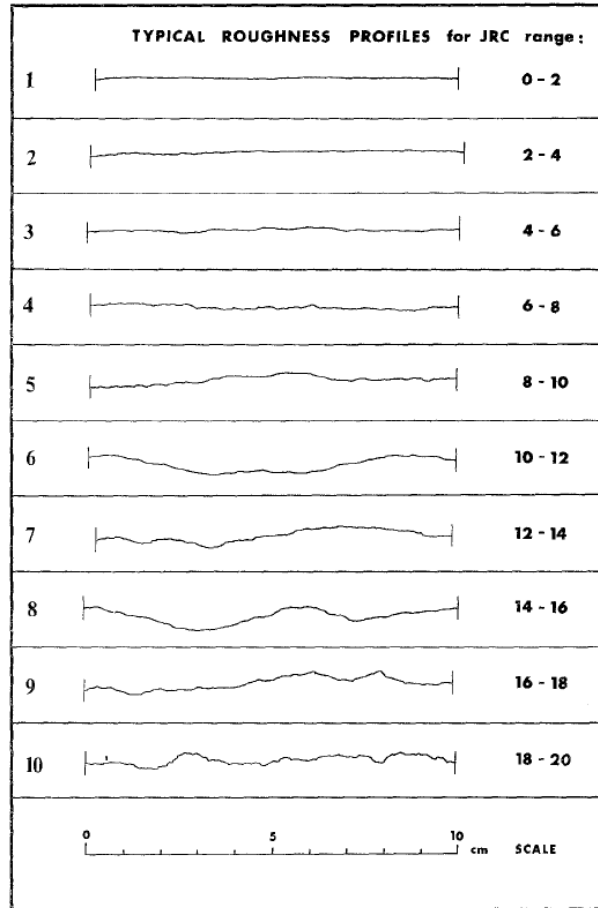


FIGURE 1: PROFILES USED TO ESTIMATE JRC VALUES. FROM BARTON & CHOUBEY (1977).

2.1.3 The impact of joint scale

Already in (Barton and Choubey, 1977), a reduction in the shear strength of joints with increasing joint length was observed. After looking into the phenomenon further in (Bandis et al., 1981) and (Barton and Bandis, 1982), it was concluded that there was a significant decrease in the peak shear strength of a joint with increasing joint length, with a diminishing impact as the length of the joint increased. They also found a significant decrease in both JRC and JCS with increasing joint length.

In (Bandis et al., 1981) the authors proposed the following equations to adjust the JRC and JCS values in the field, based on joint length.

$$JRC_n = JRC_o \left(\frac{L_n}{L_o} \right)^{-0.02 JRC_o} \quad (5)$$

$$JCS_n = JCS_o \left(\frac{L_n}{L_o} \right)^{-0.03 JRC_o} \quad (6)$$

Where JRC_n , JCS_n , and L_n represent the field conditions of the joint roughness coefficient, joint compressive strength, and joint length. And JRC_o , JCS_o , and L_o represent the values found in the lab.

2.2 Other ways to quantify joint roughness

2.2.1 Statistical

Barton's JRC parameter for quantifying joint roughness has faced criticism throughout the years for being hard to objectively determine (Maerz et al., 1990, Hsiung et al., 1993, Beer et al., 2002). Therefore, other methods for determining joint roughness have been proposed. One of these methods involve using statistical parameters derived from 2D profiles of the joint. (Tse and Cruden, 1979) looked at eight of these parameters to investigate their usefulness in determining joint roughness. By applying the different parameters on a digitized version of Barton's reference profiles, that had been upscaled by a factor of 2.5, Tse and Cruden were able to determine that there was a strong correlation between the listed JRC value of the profiles and the root mean square of the first derivative of the profile, Z_2 , and the structure function, SF. They did however point out that the parameters work best in situations where the joints are rough, and the normal stresses are small. To account for this, they proposed the following formulas be used when determining the JRC of joints.

$$JRC = 32.2 + 32.47 \log Z_2 \quad (7)$$

$$JRC = 37.28 + 16.58 \log SF \quad (8)$$

Tse & Cruden has been criticized by (Yang et al., 2001) for failing to account for the self-affinity transformation concept when upscaling the profiles. Yang et al. instead reconstructed the original Barton & Choubey profiles using a Fourier transform method to derive an even better fitting relationship between Z_2 and JRC.

$$JRC = 32.69 + 32.98 \log_{10} Z_2 \quad (9)$$

Determination of the JRC values of a profile is also susceptible to changes caused by sampling intervals as was shown by (Yu and Vayssade, 1991).

(Maerz et al., 1990) linked the roughness profile, R_p , parameter, first proposed by (El-Soudani, 1978) to JRC using the following formula.

$$JRC = 411(R_p - 1) \quad (10)$$

Over the years a lot of different relationships between various statistical parameters and JRC has been proposed. In fact, when (Li and Zhang, 2015) investigated just how many there were, they found 47 different ways to relate JRC to different statistical parameters. To make things even more complicated there was no unifying symbology between all the different literature. Li & Zhang therefore proposed rewritten versions using a unified symbology. They also “culled the herd” by comparing the JRC values produced by the different formulas against JRC values back calculated from 112 profiles. Based on this they were able to reduce the number of formulas from 47 down to 15.

2.2.2 *Fractals*

The first person to propose using fractal geometry to describe joint surfaces was (Mandelbrot, 1983). Since then, several others have looked into using fractals to determine joint roughness (Lee et al., 1990, Hsiung et al., 1993, Kulatilake et al., 1995). Fractal geometry is an alternative to the traditional Euclidian geometry that uses perfectly smooth spheres, planes, and cylinders to describe an object. However, if one looks to nature one will find plenty of examples of things that doesn't fit this clean, neat definition of shape. Clouds are not made out of perfect spheres, mountains are not cones, tetrahedrons or pyramids, and trees are not made up of smooth cylinders. Fractal geometry tries to bridge the gap between the Euclidean shapes and the real-world topographies. Mandelbrot proposed using what he referred to as the fractal dimension, D , to describe the roughness of rock joints. The fractal dimension is a fraction between the surface topography and the Euclidian shapes, and describes the degree to which the two matches. Typically, the fractal dimension increases as the surface gets rougher. For a smooth surface the fractal dimension might have a value near 1, were as a rough surface might have a value near or in excess of 2.

Several ways of determining the fractal dimension from surface profiles have been proposed. The divider method (Lee et al., 1990, Kulatilake et al., 1995), involves taking a divider with a fixed distance, r , and “walking” it along the profile, noting how many steps it takes to cover the entire profile. Then the number of steps required to cover the profile is multiplied by r , to get the approximate length of the profile L . This process is then repeated several more times to determine a relationship between the profile length and the divider spacing. When the $\log L$

and $\log r$ is plotted against each other, one finds that their relationship is linear and that the slope of the line is $1 - D$ (Lee et al., 1990).

Another way of determining the fractal dimension of a profile involves using boxes. The box-counting method (Kulatilake et al., 1995) uses rectangular boxes with set dimensions to cover the profile. By comparing the number of divisions (p) in the x and y directions (rows and columns) and the total number of boxes needed to cover the profile, N , the fractal dimension can be determined by plotting $\log N$ against $\log p$. The slope of the resulting line is equal to the fractal dimension, D .

It should be noted that the relationships described above are only valid for self-similar fractals. A self-similar fractal is a fractal that maintains its statistical properties at different scales. This is not necessarily similar to how things are in the real world, where there can be significant differences between the large-scale topography and the small-scale topography of a surface (Brown and Scholz, 1985). This brings us to the other type of profiles. Self-affine fractals are fractals where the x - and y -axis needs to be scaled differently to maintain the statistical properties. (Grasselli, 2001) points out that some care needs to be taken when dealing with papers on fractal geometry, as not all authors differentiate between self-similar and self-affine fractals.

(Lee et al., 1990) found the following empirical relationship between the fractal dimension and JRC.

$$JRC = -0.87804 + 37.7844 \left(\frac{D-1}{0.015} \right) - 16.9304 \left(\frac{D-1}{0.015} \right)^2 \quad (11)$$

2.2.3 3D roughness

All the methods of describing joint roughness so far have been based on information from 2D profiles of the joint surface. However, some researchers in more recent years have proposed that this gives an incomplete picture of the joint roughness (Kulatilake et al., 1995, Grasselli, 2001, Grasselli et al., 2002). They have therefore proposed using parameters derived from three-dimensional information of the joint surface to describe surface roughness. (Grasselli et al., 2002) used triangulated surface scans of 39 joint surfaces, captured using an ATS system. Doing this allowed for the determination of the apparent dip and azimuth of each individual surface triangle. Assuming that, only those surfaces with an apparent dip angle over a certain threshold θ^* , in the direction of shear are affected by the shearing, it would be possible to

determine the affected area size A_{θ^*} . Using these two parameters Grasselli proposed the following relationship between the dip angle and the disturbed area.

$$A_{\theta^*} = A_0 \left(\frac{\theta_{max}^* - \theta^*}{\theta_{max}^*} \right)^C \quad (12)$$

Where A_0 is the maximum possible contact area, θ^* is the required threshold value for the dip angle, θ_{max}^* is the maximum apparent dip angle of the surface, Grasselli found that θ_{max}^* typically ranges between 20 and 90 degrees, with a point-spacing of 250 μm . C is dimensionless fitting parameter determined by a best-fit regression analysis of the dip angles of the surface. Since the joint surface changes during the shearing process, Grasselli proposed using (θ_{max}^*/C) as a quantitative measure of roughness.

(Tatone and Grasselli, 2009) further refined the determination of roughness by connecting (12) to the area under the cumulative distribution of the apparent dip angles of the joint.

$$A_0 \int_0^{\theta_{max}^*} \left(\frac{\theta_{max}^* - \theta^*}{\theta_{max}^*} \right)^C d\theta^* = A_0 \left(\frac{\theta_{max}^*}{C+1} \right) \quad (13)$$

Lastly, (Tatone and Grasselli, 2010) applies the $(\theta_{max}^*/C + 1)$ roughness parameter to 2D profiles with length standing in for area.

$$L_0 \int_0^{\theta_{max}^*} \left(\frac{\theta_{max}^* - \theta^*}{\theta_{max}^*} \right)^C d\theta^* = L_0 \left(\frac{\theta_{max}^*}{C+1} \right) \quad (14)$$

Using the $(\theta_{max}^*/C + 1)_{2D}$ parameter for roughness, (Tatone and Grasselli, 2010) were able to derive the following relationships to JRC.

$$JRC = 3.95(\theta_{max}^*/[C + 1]_{2D})^{0.7} - 7.98 \quad (\text{for } 0.5\text{mm sampling interval}) \quad (15)$$

$$JRC = 2.40(\theta_{max}^*/[C + 1]_{2D})^{0.85} - 4.42 \quad (\text{for } 1.0\text{mm sampling interval}) \quad (16)$$

2.3 Ways of recording surface roughness

2.3.1 Mechanical

For a long time, the way of recording a surface involved some sort of mechanical profilometer. These can involve thin pieces of metal that slide past each other, which can be placed on a joint surface and then clamped together to preserve a cast of the surface topography. This type of profile gauge typically has a sampling interval of about 0.5-1 mm, and can typically cover profile lengths between 5 – 20 cm.

When a higher degree of accuracy is required more advance types of profilometers are employed. These typically involve a stylus moving along the joint surface measuring the vertical displacement. These machines are usually bigger and therefore reserved for work in lab settings. They do however allow for sampling intervals as low as 0.03 mm (Kim, 2016). One problem these of machines can have is related to the interaction between the stylus and the surface, as noted by (Grasselli, 2001), either by minor deformation of the surface by the stylus or by flexing of the stylus caused by moving over asperities, leading to differences in the recorded profile in the forward and reverse direction.

2.3.2 Surface recording

Using mechanical profilometers can be time consuming, and when taking into account the potential to damage the surface, a need for methods of surface recording without direct contact arose. One of the methods devised was laser profilometry (Huang et al., 1992, Belem et al., 2000, Lanaro, 2000), which uses laser beams projected onto the surface to determine the distance from the sensor to the surface by recording the strength of the reflected light. (Rousseau et al., 2012) does point out a problem with using this method. If the surface contains very reflective minerals like quartz or micas, then this can result in erroneous recordings of the surface height.

Another way of determining the surface roughness that involves using light, or in this case the lack of light, is shadow profilometry (Maerz et al., 1990). This method involves shining a light at a 45° angle onto a straight edge, and then recording the difference in the shadow pattern created on the surface. using this method does require consistent lighting conditions and care needs to be taken with camera placement.

2.3.3 3D

All the methods previously mentioned have one thing in common, they all measure the surface in 2 dimensions. However, in more recent times the approach of measuring joint surfaces just in 2D has come under fire. Several authors have proposed that in order to get a true representation of the roughness of a joint surface a three-dimensional approach is needed (Kulatilake et al., 1995, Grasselli and Egger, 2003, Tatone and Grasselli, 2010).

(Grasselli, 2001) chose to solve the issue by using an ATS (Advanced Topographic Sensor) system. The system uses a measuring head, that contains a projector and two cameras offset at an angle (see Fig. 2)

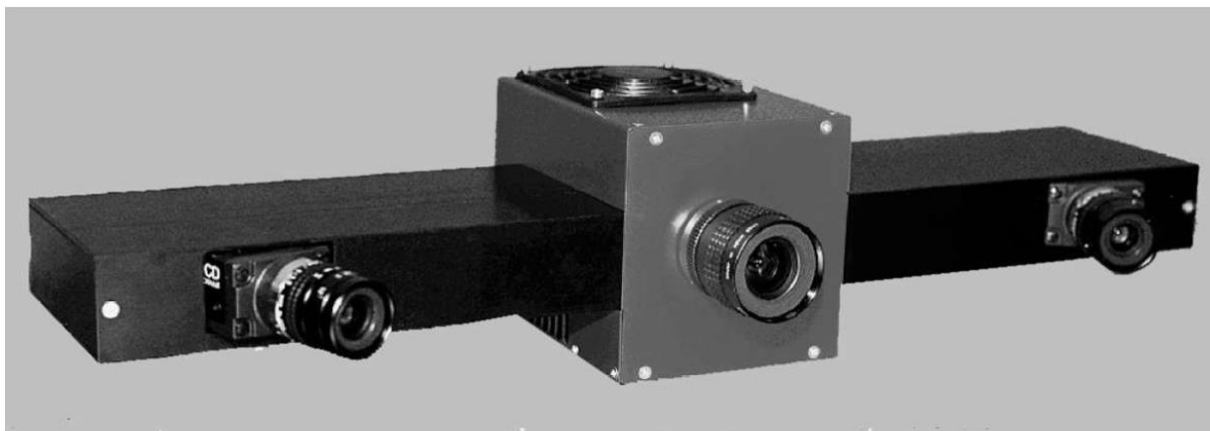


FIGURE 2: ATS MEASURING HEAD. THE PROJECTOR CAN BE SEEN IN THE MIDDLE, FLANKED BY THE TWO CAMERAS. IMAGE FROM (GRASSELLI, 2001).

The system works by having the projector project different white-light fringe patterns onto the surface and recording them with the two cameras. This then allows for triangulation of 3D coordinates on the surface used for creation of a point cloud. The system has a reported accuracy of $\pm 50 \mu\text{m}$ and creates a point cloud with over 400,000 points (Grasselli, 2001).

In recent years the use of laser scanners (also referred to as LiDAR) in geosciences has increased. While multiple different manufacturers and models exist, they all operate on the same principle. A light pulse gets sent out by the system, travels to the surface, gets reflected, travels back to the system, and gets recorded. Based on the time of travel, the system can calculate the distance. The system also tracks pitch, yaw, and roll. When all of this is combined with positional data, often acquired from onboard GPS systems, it's possible to create high density point clouds of surfaces quickly (up to 5000 points/s (Candela et al., 2009)).

2.4 Photogrammetry

Due to the relatively low cost of entry, photogrammetry has been gaining in popularity in the geosciences for quite some time. Photogrammetry allows for collection of 3D data at different scales, using a multitude of different platforms, including UAVs (Lucieer et al., 2014) and even cellphones (Micheletti et al., 2015). When it comes to using photogrammetry to investigate the roughness of surfaces, several authors throughout the years have looked into the possibility (Wickens and Barton, 1971, Jessell et al., 1995, Lee and Ahn, 2004, Unal et al., 2004, Sturzenegger and Stead, 2009, Bistacchi et al., 2011, Nilsson et al., 2012). (Kim, 2016) gives a good review of these papers.

The basic principle behind photogrammetry involves taking two or more images of an object or surface with a slight offset between each image. This allows for triangulation of identifiable points to find the position relative to the camera. Often, there will be points with a known position, called ground control points or GCPs included in the images to facilitate orientation of the images in a predefined coordinate system.

Back in the days of analog cameras, the photogrammetric process would require considerable experience and knowledge on the part of the operator. These days the process has gotten significantly easier, with the use of digital cameras and computer algorithms. Both commercial and open-source photogrammetric software exists to make the process easier than ever.

2.4.1 Error sources

There are a couple of potential sources of errors when it comes to photogrammetry, some are related to the equipment used to collect the data, like lens distortion and image noise. Others are related to experimental setup. (Dai et al., 2014) lists several of the errors that can affect photogrammetry and the impact of the different error sources (see Table 1).

Broadly speaking, since each pixel in an image used for photogrammetry represents a data point, the distance between the camera and the surface being photographed affects the level of detail one can capture. (Kim, 2016) gives the following relationship between the distance and the area each pixel covers. $Ground\ Pixel\ Size\ (GPS) = \frac{d}{f} * Sensor\ pixel\ size\ (SPS)$ (17)

Where d is the camera distance and f is the focal length of the lens. Another factor that effects how much detail that can be captured, is the resolution. The higher the resolution is then more pixels there are in the image, and by extension the smaller the individual pixels are. While use of the highest possible resolution is recommended, it should be noted that increasing image

resolution also results in larger file sizes. Which in turn results in longer processing times on the images.

Another big error source is lens distortion. Lens distortion generally falls into two types: radial and decentering. Radial distortion is caused by the lenses themselves and increases with distance from the center of the lens. The light essentially enters the camera lens as parallel beams, but due to the lens shape, the light towards the edges of the lens gets deflected more than the light hitting the center, causing distortion. Decentering distortion arises from the fact that most camera lenses consist of more than one lens. Due to flex in the lens housing and manufacturing imperfections, the lenses are slightly out of alignment with each other, leading to distortions.

(Poropat, 2009) investigated the effect that noise has on surface measurements by looking into previously published data and conducting their own experiments using a laser scanner. Their conclusion was that noise does have an effect, often leading to an overestimation of surface roughness, especially when using fractals. The conclusion therefore was that some sort of smoothing of the data is necessary for accurate estimation of surface roughness.

The other type of errors that can affect the results of photogrammetry are tied to how the data is collected. The biggest of these is probably the degree of overlap between images. (Dai and Lu, 2013) found that having an overlap percentage between images of about 55% resulted in the best accuracy, when at 15 m with a 4 m interval between the cameras, and desiring to use the smallest number of photos to cover the object. (Dai et al., 2014) does however note that having a higher number of overlapping images does lead to a higher accuracy (Table 2). The offset to this is of course that using a higher number of images does lead to longer processing times, especially when the image resolution is high (> 12 MP) (Westoby et al., 2012, Mosbrucker et al., 2017).

Another issue related to planning is the problem related to occlusion. Care needs to be taken when choosing light and camera placement to ensure maximum coverage. Failing to do so could result in cast shadows covering parts of the surface one is trying to record, leading to loss of data in those areas. The angle of the surface relative to the camera also an important factor, whenever possible the camera should be placed as perpendicular to the surface as possible to avoid issues with perspective shifts.

TABLE 1: LIST OF PHOTOGRAMMETRIC ERROR SOURCES AND THEIR EFFECT. (DAI ET AL., 2014)

Factor	Behavior
Distance	Farther distance, lower accuracy (40 m: 6 ~ 10 cm)
Number of overlapping photos	The larger number of overlapping photos, the better accuracy
Intersection angle	The closer to 90°, the better accuracy
Angle of incidence	The closer to 0°, the better quality of images, so the better accuracy
Camera model	Higher end, higher accuracy
Resolution	Strong correlation with accuracy (raise by 1.6% per 1 MB increase)
Features (texture)	More features, higher accuracy; higher accuracy by colorful texture than grey/plain texture
Focal length	Longer focal length, higher accuracy; set to obtain optimum coverage
Camera lens	Less distortion, higher accuracy

3.0 Methods

3.1 Sample preparation

3.1.1 Plaster

In addition to the Sandstone samples, several samples made from plaster were prepared and sheared. These samples were made by placing a fractured sandstone sample inside a brass pipe with an inner diameter roughly equal to the diameter of the sandstone sample. The sandstone sample had a diameter of ~50 mm. To prevent the plaster from sticking to the brass and sandstone surface, making non-destructive removal of the plaster cast nearly impossible, a silicone-based grease (Molykote® 111 compound) was applied to the surface of the sandstone surface and the inside of the brass pipe. It was possible to remove this grease afterwards using rubbing alcohol by gently rubbing, taking care not to damage the surface too much.

Plaster powder was mixed with water at a ratio of 2:1 determined by weight. Once the plaster had been poured into the mold, it was gently shaken in order to try to remove any trapped air bubbles. Once the plaster had hardened the sample was gently removed from the brass pipe and the two halves separated. The plaster cast was then placed back inside the brass pipe and

a second casting was made. This was done because it turned out that making a cast of each half of the sandstone joint resulted in very poor fit between the two halves of the plaster casts.

Plaster was chosen as the test material since it is cheap, readily available, and easy to work with. Several different authors have used plaster to model soft sedimentary rocks (Indraratna, 1990, Indraratna et al., 1998, Babanouri et al., 2011, Indraratna et al., 2014, Indraratna et al., 2015, Liu et al., 2020).

3.1.2 Sandstone

To have some data using actual rock in addition to the plaster, several sandstone samples were also prepared. These consisted of two different types of sandstone: One, going forwards referred to as the α -sandstone was medium-grained with a reddish grey color, and in at least one of the samples containing layers of mica. The other sandstone, referred to as the β -sandstone, was also medium grained and had a red coloration. It also contained what appeared to be compaction bands in some of the samples. The β -sandstone was very crumbly to the touch compared to the α -sandstone.

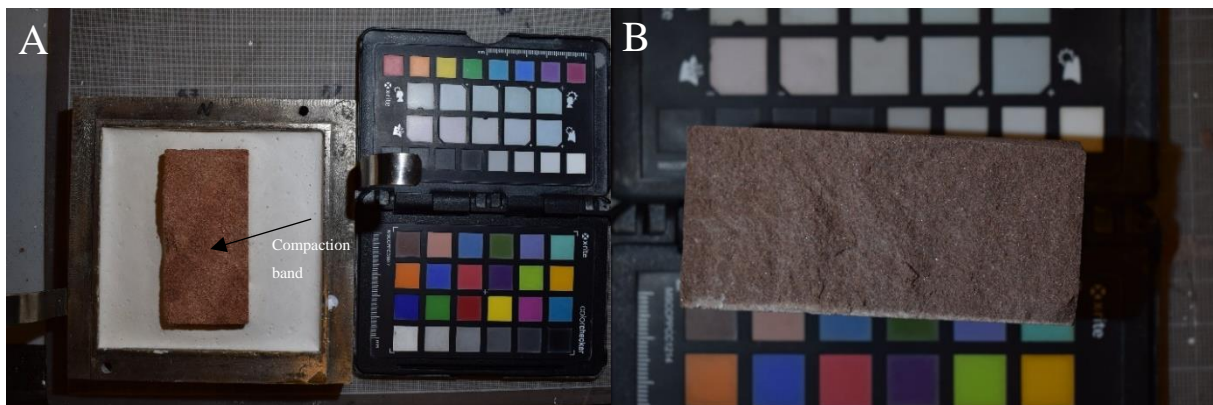


FIGURE 3: A) THE BETA SANDSTONE, WITH WHAT APPEARS TO BE A COMPACTION BAND RUNNING THROUGH IT. B) THE ALPHA SANDSTONE

All the samples were prepared from drill-cores with a diameter of roughly 50 mm. Some of them were broken along the layering creating circular samples, and some of them were broken across the grain creating rectangular samples.

TABLE 2: SUMMARY OF THE SANDSTONE SAMPLES

Sample	Shape	Height/ Width [mm]	Diameter/ Length [mm]	Weight [g]	Density [g/cm ³]
SA1	Round	30.04	49.72	116.18	1.992
SA2	Round	30.33	49.70	116.80	1.985
SA3	Rectangular	38.02	80.80	181.11	1.974
SA4	Rectangular	38.10	80,77	180.76	1.963
SB1	Rectangular	37.90	79,87	166.07	1.843
SB2	Rectangular	37.94	77,68	164.06	1.868
SB3	Rectangular	37.87	77,57	165.70	1.897

3.2 Uniaxial tests

In order to apply the Barton-Bandis method to determine the shear strength of the samples, it was necessary to first determine the compressive strength of the samples. To determine this uniaxial testing was performed on several samples. The samples were prepared to a diameter of $25 \text{ mm} \pm 0.5 \text{ mm}$ and cut to lengths of between 50-55 mm. 3 plaster samples were prepared for the uniaxial test, as well as 3 α -sandstone samples and 6 β -sandstone samples. An overview of the samples used can be seen in Table 3 and 4.

3.2.1 Plaster

The 3 plaster samples were allowed to dry for roughly 24 hours before testing, just like the shear samples. In addition to the three samples where the drying time was more strictly controlled, another 6 plaster samples were tested. However, these samples had a drying time of anywhere between 2-3 days to upwards of a month. Due to this the compressive strength of the plaster was determined only using the 3 samples with a similar drying time to the samples being sheared.

TABLE 3: OVERVIEW OF THE PLASTER SAMPLES USED IN THE UNIAXIAL TESTS. DRYING TIMES GREATER THAN 24 HOURS ARE AN APPROX. ESTIMATE.

Sample	Diameter [mm]	Height [mm]	Weight [g]	Density [g/cm ³]	Dry time
1	25.03	52.54	36.49	1.41	~ 24 h
2	25.05	54.92	38.00	1.40	~ 24 h
3	25.00	51.93	37.14	1.46	~ 24 h
4	24.94	52.82	29.1	1.13	~ 2-3 days
5	24.87	51.69	37.59	1.50	~ 2-3 days
6	24.97	57.45	41.63	1.48	~ 2-3 days
7	25.04	56.27	34.95	1.26	~ 3-4 weeks
8	25.02	54.38	40.20	1.50	~ 3-4 weeks
9	25.02	52.70	33.06	1.28	~ 3-4 weeks

3.2.2 Sandstone

TABLE 4: OVERVIEW OF THE SANDSTONE SAMPLES USED IN THE UNIAXIAL TESTS

Sample	Diameter [mm]	Height [mm]	Weight [g]	Density [g/cm ³]
A1	24.89	51.60	50.08	1.99
A2	24.83	51.61	50.05	2.00
A3	24.81	51.62	49.88	2.00
B1	24.88	60.83	55.35	1.87
B2	24.76	51.59	46.87	1.89
B3	24.63	51.75	46.40	1.88
B4	24.63	51.73	46.39	1.88
B5	24.13	51.61	44.10	1.87
B6	24.48	51.60	45.95	1.89

3.3 Shear test

3.3.1 Shear-test sample preparation

Each half of both the plater and sandstone samples was incased in plaster, mixed at a ratio of 1:1.75 water to plaster by weight. About 5 mm of free space was left between the incasing material and the joint surface (Figure 4). Care was taken to ensure that the joint plane was placed roughly equidistant between the two halves of the shear-box frame, with 3-6 mm of space separating the two halves to ensure that only the joint surfaces were in contact with each other.

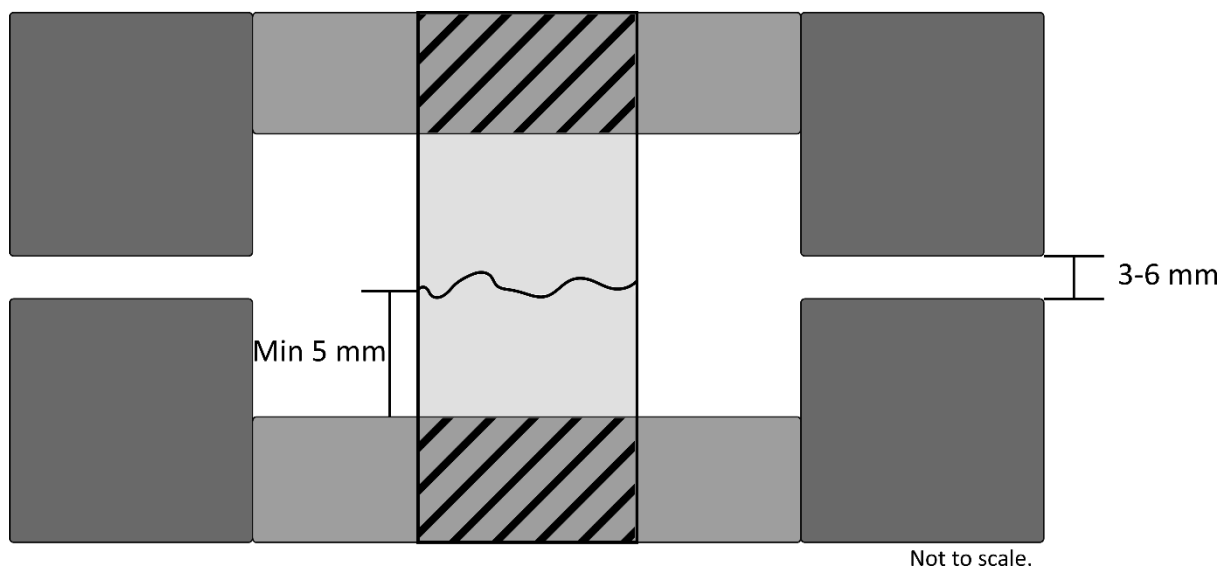


FIGURE 4: FIGURE SHOWING HOW THE SAMPLES WERE MOUNTED FOR SHEAR TESTING.

3.4 Shear-box testing

3.4.1 Consolidation

In order to ensure proper mating of the two halves during testing, the samples were pre-loaded prior to shearing. This was done by incrementally adding load to the system and then allowing the sample to settle before commencing with the shear test. The load was applied by adding weights to a lever arm that multiplied the applied load by a factor of 10. The weight was added in three steps, waiting roughly 10 minutes between each step, and then waiting an additional 25-30 minutes after the last step before shearing. The amount of weight added per step would vary based on the desired final normal load. Table 5 gives a breakdown of the weight added per step for the different final normal loads.

TABLE 5: THE DIFFERENT LOAD STEPS USED ON THE SAMPLES DURING THE CONSOLIDATION OF THE SHEAR SAMPLES.

	1 MPa	2 MPa	3MPa
1 st step	5 kg	10 kg	20 kg
2 nd step	5 kg	10 kg	20 kg
3 rd step	10 kg	20 kg	20 kg

3.4.2 Shear test

Once the consolidation was done the next step was to perform the shear test. The shear box is calibrated to have a shear rate of 0.001 mm/s. Horizontal and vertical displacement was recorded using LVDT sensors and the shear stress was recorded using a 10kN force sensor. The test was set-up so that the shearing would stop once the horizontal deformation reached 5 mm. The horizontal and vertical deformation as well as the shear force was recorded using CRS Modlab and written into a text file.

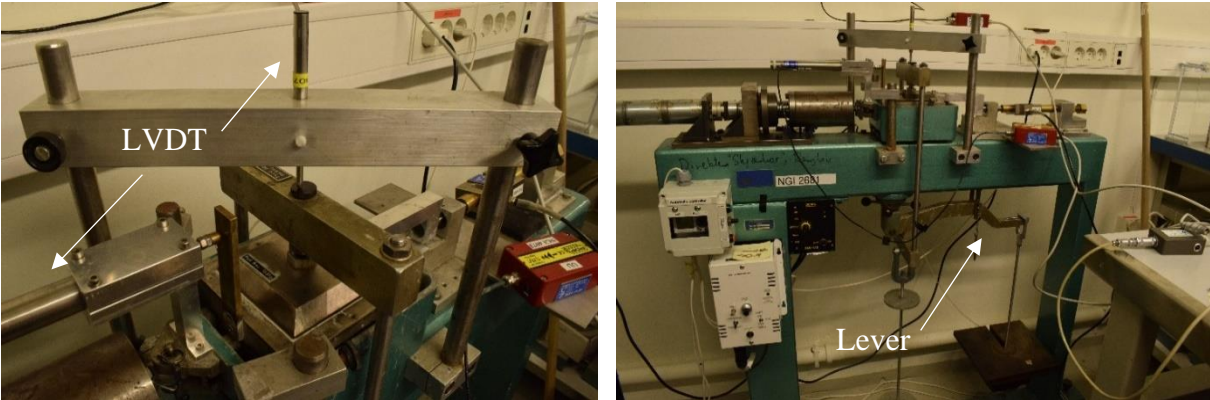


FIGURE 5: SHEAR BOX USED FOR SHEAR TESTING. THE IMAGE ON THE LEFT SHOWS THE HORIZONTAL AND VERTICAL LVDT SENSORS. IN THE IMAGE ON THE RIGHT THE ENTIRE SHEAR BOX SETUP CAN BE SEEN. THE LEVER ARM USED TO APPLY THE NORMAL LOAD CAN BE SEEN IN THE BOTTOM HALF OF THE IMAGE.

3.5 Photogrammetry

3.5.1 Image collection & image settings

All samples in this thesis were photographed using either a Nikon D7200 camera with a 18-65 mm macro lens, or a Nikon D3300 camera with a 18-55 mm general lens. Table 6 lists the camera settings used. The low ISO setting necessitated the use of additional light in order to get usable images. This was accomplished by using a single LED-lamp mounted at a 45-degree angle to the surface of the sample. The additional directional light also helped by creating small cast shadows on the surface of the samples, giving the photogrammetric software more tie points to work with. Between 14-18 images were taken of both the top and bottom surface, to ensure good coverage of the sample, with care being taken to ensure that each of the ground control points (GCPs) were visible in at least 3 separate images. Images were taken both before and after testing. Figure 6 shows the setup.

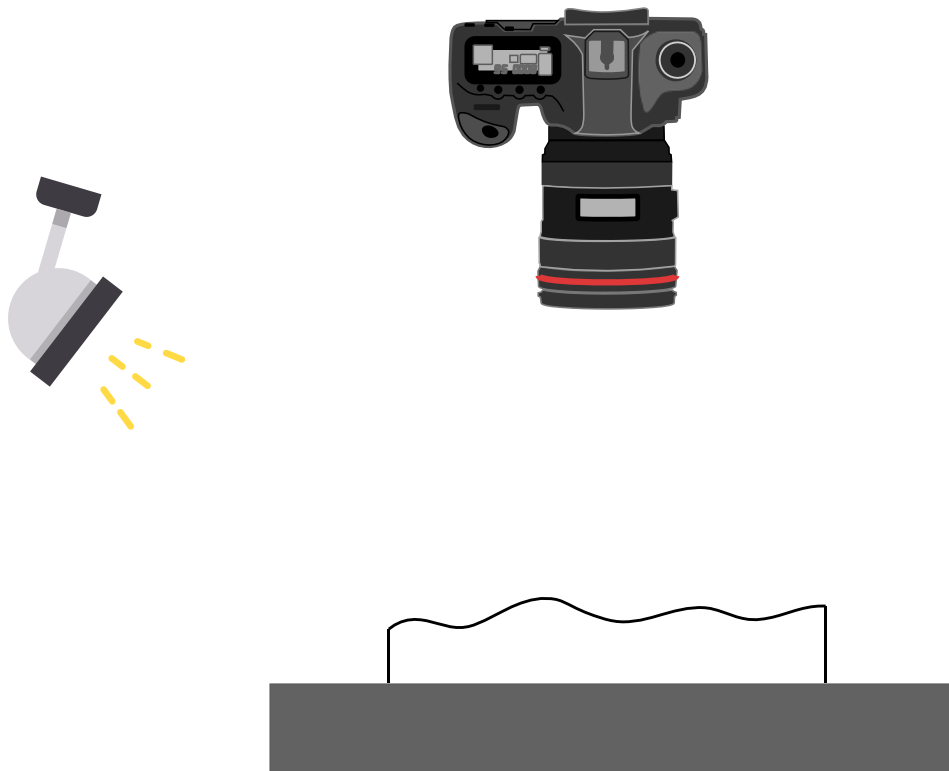


FIGURE 6:SETUP USED TO COLLECT PHOTOGAMMETRY DATA. THE SETUP CONSISTED OF A DIGITAL CAMERA MOUNTED PERPENDICULAR TO THE SAMPLE SURFACE. AN ADDITIONAL LIGHT, MOUNTED AT A 45 DEGREE ANGLE TO THE SAMPLE, WAS NEEDED TO ENSURE SUFFICIENT IMAGE QUALITY.

TABLE 6: CAMERA SETTINGS USED DURING PHOTOGRAMMETRY DATA COLLECTION.

Camera setting	Value
ISO	100
F-Stop	F8-F10
Shutter speed	1/200-1/400
Focal length	55 mm

3.5.2 MicMac workflow

MicMac is an open-source photogrammetry software package developed by scientists at the IGN (French National Geographic Institute) and ENSG (French national school for geographic sciences). It's controlled through the command window on the computer, meaning that it isn't necessarily the most user-friendly experience right out of the box. But it compensates by being flexible due to its open-source nature.

The general workflow when MicMac for this thesis was as follows (also shown in Figure 7):

1. Use the Tapioca command to find matching tie points in the images using a SIFT algorithm and finds their position in a relative coordinate system.
2. The Tapas command uses the ties points found in the previous step to find the camera position and to correct for camera distortion, using a FraserBasic algorithm.
3. Apericloud creates a sparse point-cloud, allowing the user to check if the position of the tie points and the camera makes sense and that there aren't any strange artifacts in the data.
4. If things look good, then the next step is to pick out the ground control points (GCPs) in the images using the SaisieAppuisInitQT function. This opens a graphical interphase that allows the user to select the position of GCPs in an image. A GCP is a point in an image is a point with a known position in 3D space. At least 3 GCPs needs to be identified a minimum of 3 images for the process to work. However, all the GCPs don't have to be visible in every image for the process to work. The inside corners of the shear-box frame were used as GCPs in this case.
5. Next the GCPBascoule command uses the positions of the GCPs in the previous step to orient and scale the model in a calibrated coordinate system.

6. The Campari function allows for further refinement of the orientation and scaling by using both the 2D positions of the GCPs found using SaisieAppuisInitQT and the 3D positions of the GCPs from a .xml file.
7. The Malt command uses this to create a DEM of the imaged surface.
8. The Tawny command uses all the data from the previous steps to create an orthorectified image of the surface. The orthorectified image has a uniform scale across the entire image, allowing for accurate measurements based on it.
9. Lastly the Nuage2Ply command creates a ply. point cloud based on the DEM and orthorectified image.

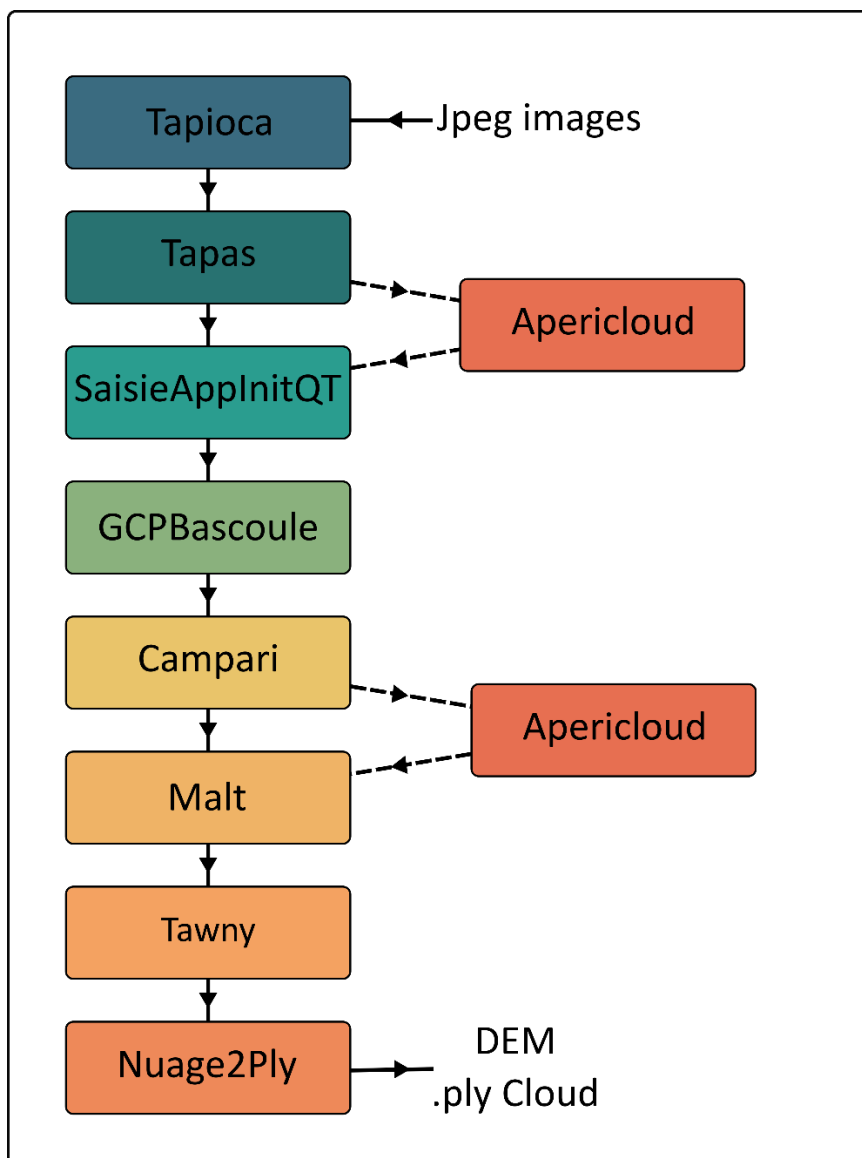


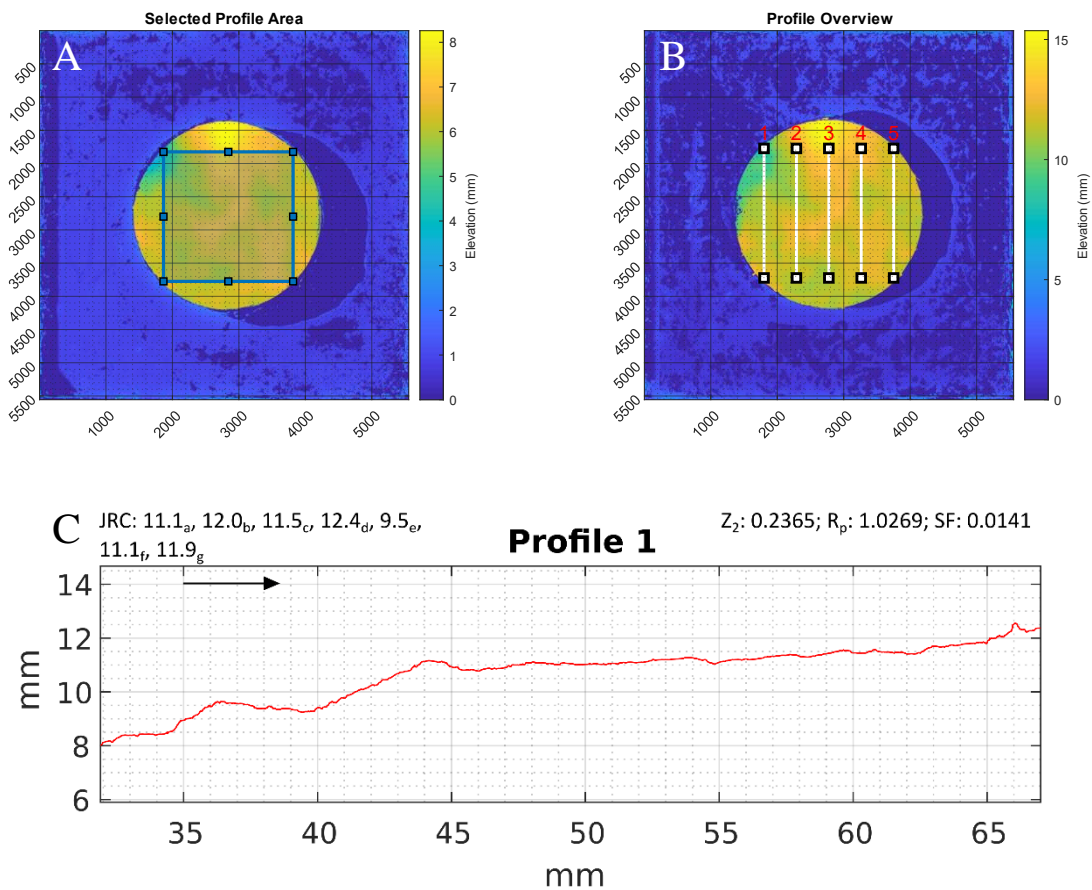
FIGURE 7: GENERAL WORKFLOW USING MICMAC

3.6 Data processing

3.6.1 Loading DEMs and selecting profiles

The DEM produced by the MicMac workflow was loaded into MATLAB in order to create the profiles used to calculate the JRC values. With the DEM loaded, the next step was to select the area that the profiles would cover, this was done manually by drawing a square covering the sample surface (Figure 8a). In order to ensure that the profile all had a similar length, the square had to be kept inside the surface of the sample. This means that parts of the sample surface could not be covered.

With the profile area selected, five profiles were extracted from the area along the direction of shear (Figure 8b). Examples of the profiles created can be seen in Figure 8c.



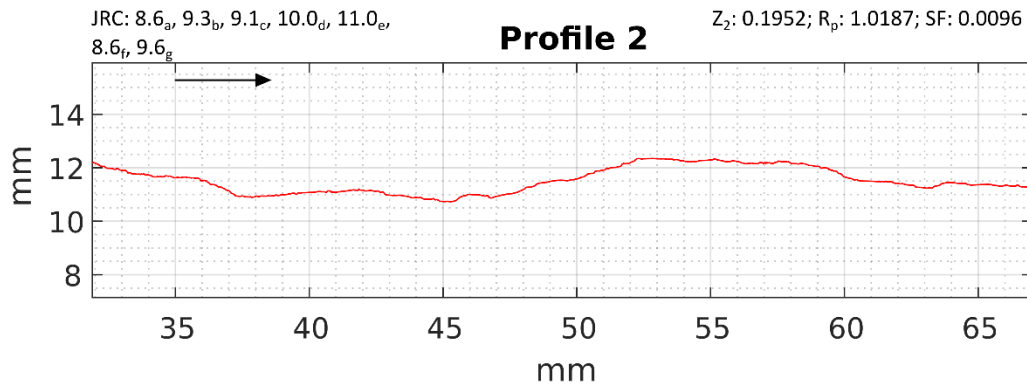


FIGURE 8: A) THE AREA FROM WHICH THE SURFACE PROFILES WERE EXTRACTED. B) OVERVIEW OF THE POSITION OF THE CREATED PROFILES. C) EXAMPLES OF THE PROFILES CREATED FROM THE DEM. JRC A-G CORRESPONDS TO FORMULA 18-24 IN ORDER.

3.6.2 Calculating Z_2 , SF & R_p

In order to calculate the statistical parameters used to determine JRC for the profiles, the profiles first had to have any tilt in them removed. This was done by first finding the best fit line using linear regression, and then determining the tilt of that line. Once the tilt was determined the profile could then be un-tilted using a simple rotation matrix.

With the profiles leveled, it was then possible to determine the statistical parameters needed to calculate the JRC value for the profile. In order to calculate the Z_2 , SF & R_p value for the profile, the profile was sampled at an interval of 0.5 mm and then the different parameters were calculated in accordance to their formulas listed in (Li and Zhang, 2015).

3.6.3 Calculating JRC

With the different statistical parameters calculated the last step to determine the profile JRC was to calculate it using various formulas, all but two of which are conveniently collected in (Li and Zhang, 2015), with the last two coming from (Liu et al., 2017) and (Jang et al., 2014). Five formulas using Z_2 were used, as well as one formula using SF and one formula using R_p , for comparison. All the formulas used, except the one by (Liu et al., 2017) were based around a sampling interval of 0.5 mm. The formula by (Liu et al., 2017) also used a sampling interval of 5 mm.

The formulas used are as follows.

Z₂

$$JRC = 61.79 * Z_2 - 3.47; \text{ originally from (Yu and Vayssade, 1991)} \quad (18)$$

$$JRC = 32.69 + 32.98 * \log(Z_2); \text{ originally from (Yang et al., 2001)} \quad (19)$$

$$JRC = 51.85(Z_2)^{0.60} - 10.37; \text{ originally from (Tatone and Grasselli, 2010)} \quad (20)$$

$$JRC = 51.16(Z_2)^{0.531} - 11.44; \text{ (Jang et al., 2014)} \quad (21)$$

$$JRC = 16.09 Z_2^{1st} + 12.70 \log Z_2^{2nd} + 33.75; \text{ (Liu et al., 2017)} \quad (22)$$

SF

$$JRC = 121.13\sqrt{SF} - 3.28; \text{ originally from (Yu and Vayssade, 1991)} \quad (23)$$

R_p

$$JRC = \left(0.036 + \frac{0.00127}{\ln(R_p)}\right)^{-1}; \text{ originally from (Tatone and Grasselli, 2010)} \quad (24)$$

In order to have something to compare the photogrammetric JRC estimates with, JRC was also back calculated from the shear test results. This was accomplished by using formula (3), solving for JRC. Given that the joint surface was unweathered, the compressive strength of the sample could be used instead of JCS, as stated by (Barton, 1973). The residual friction, Φ_r , used was chosen by taking an average of the last 2-300 friction values of the test. Since there was a little bit of fluctuation in the friction values, JRC was also calculated using the highest and the lowest friction value in the chosen range. That way it was also possible to get an idea of the upper and lower boundary of the back calculated JRC values and the spread between them.

4.0 Data

4.1 Uniaxial

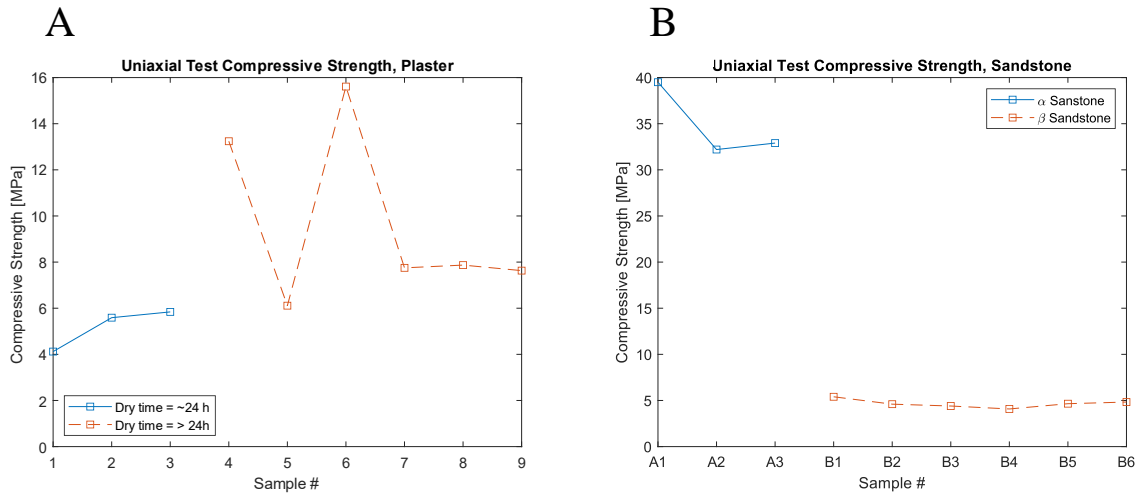


FIGURE 9:A) COMPRESSIVE STRENGTH OF THE PLASTER SAMPLES. B) COMPRESSIVE STRENGTH OF THE SANDSTONE SAMPLES.

Figure 9 shows the results from the uniaxial tests. In Fig. 9a, one can see that the compressive strength of the three plaster samples that were allowed to dry for 24 hours is somewhat lower than for most of the samples that had longer drying times. As can be seen the longer dried samples also has a much more significant spread in terms of the compressive strength.

Fig. 9b shows the compressive strength for the sandstone samples. The α -sandstone samples do have a significant spread, with an upper value of 39.5 MPa and a lower value of 32 MPa. The β -sandstone samples are much more consistent, only ranging from a little over 5 MPa to around 4.5 MPa. This does also mean that the β -sandstone is a weaker material than the plaster, something that is backed up by the experience of handling the samples, where the β -sandstone samples were quite crumbly.

4.2 Shear tests

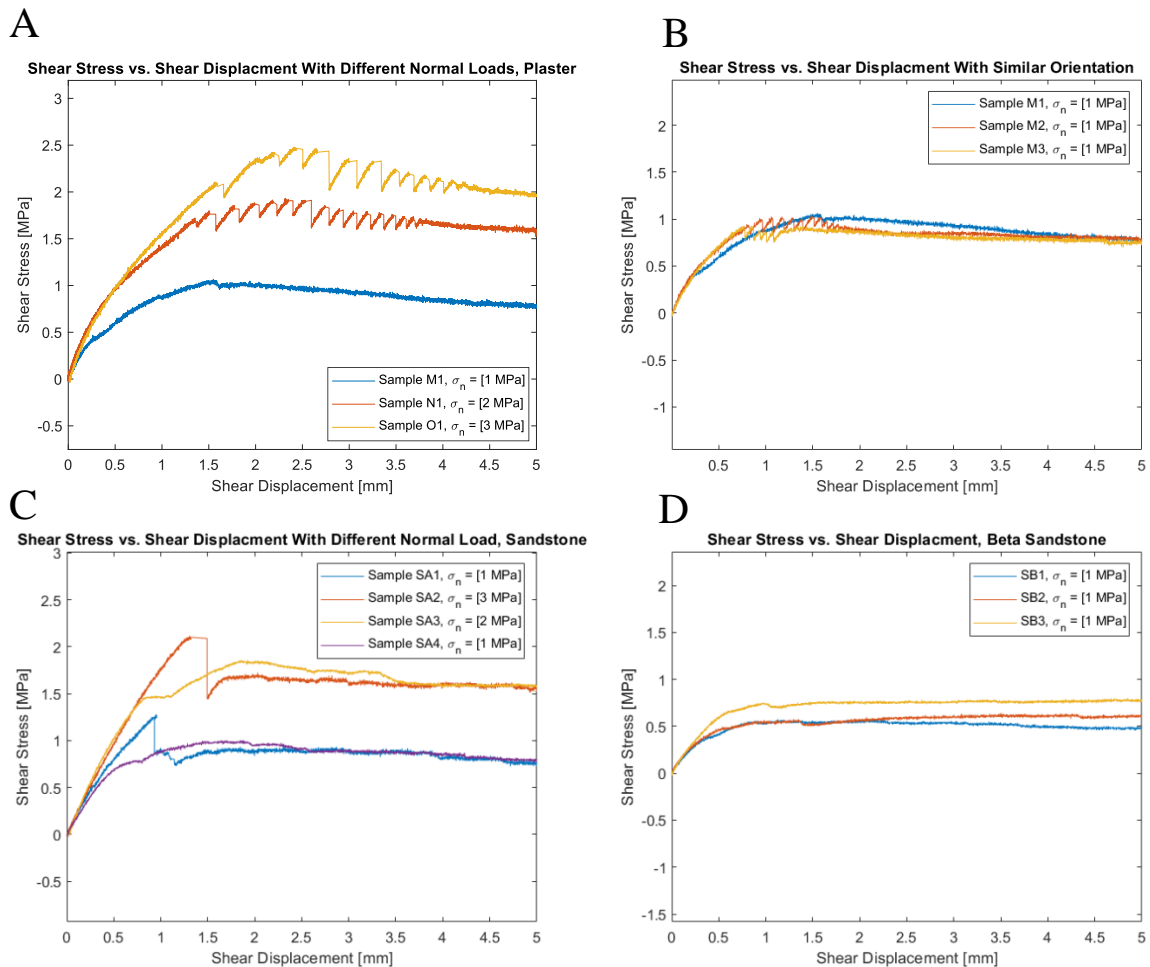


FIGURE 10: A) FIGURE SHOWS THE DEVELOPMENT OF THE SHEAR STRESS ON THREE PLASTER SAMPLES, AT DIFFERING NORMAL LOADS. ALL THREE SAMPLES HAD SIMILAR GEOMETRY AND ORIENTATION. B) SIMILAR TO THE PREVIOUS FIGURE, HOWEVER, THIS TIME THE NORMAL LOAD WAS KEPT THE SAME ACROSS THE THREE TESTS. C) RESULTS OF THE SHEAR TESTS USING THE ALPHA SANDSTONE WITH DIFFERING NORMAL LOADS. SAMPLE SA1 AND SA2 HAD A SIMILAR SHAPE (ROUNDED) AND SAMPLE SA3 AND SA4 HAD A SIMILAR SHAPE (RECTANGULAR). D) THE SHEAR TEST RESULTS USING THE BETA SANDSTONE, THIS TIME NOT VARYING THE NORMAL LOAD.

The results of the shear tests are shown in Figure 10. Fig. 10a and Fig. 10b show the results using plaster samples, both with varying normal load and without. As expected, increasing the normal load results in an increase in the maximum shear stress. When the normal load is kept constant the maximum shear stress is much closer to each other. A more interesting observation is the fact that all but one of the tests displays a “sawtooth” pattern leading up to, and following peak shear stress. The pattern is defined by a sharp dropoff in the shear stress followed by a gradual increase before dropping off again. The pattern attenuates over time eventually disappearing.

Fig. 10c shows the difference in peak shear stress for the α -sandstone under different normal loads. Again, increasing the normal load results in a higher peak shear stress value. It is worth noting for the sake of comparison that the first two samples (SA1 & SA2) have a different surface geometry than the latter two samples (SA3 & SA4), where the latter two have a rectangular geometry vs a circular geometry for the first two.

Fig. 10d shows the shear stress for the β -sandstone, for these tests the normal load was kept the same between tests and as such display a similar behavior to the plaster shear tests where normal load was kept the same. There is however, a slightly larger spread in the peak shear stress for the sandstone samples compared to the plaster samples, most likely caused by differences in the joint surfaces found in the sandstone samples.

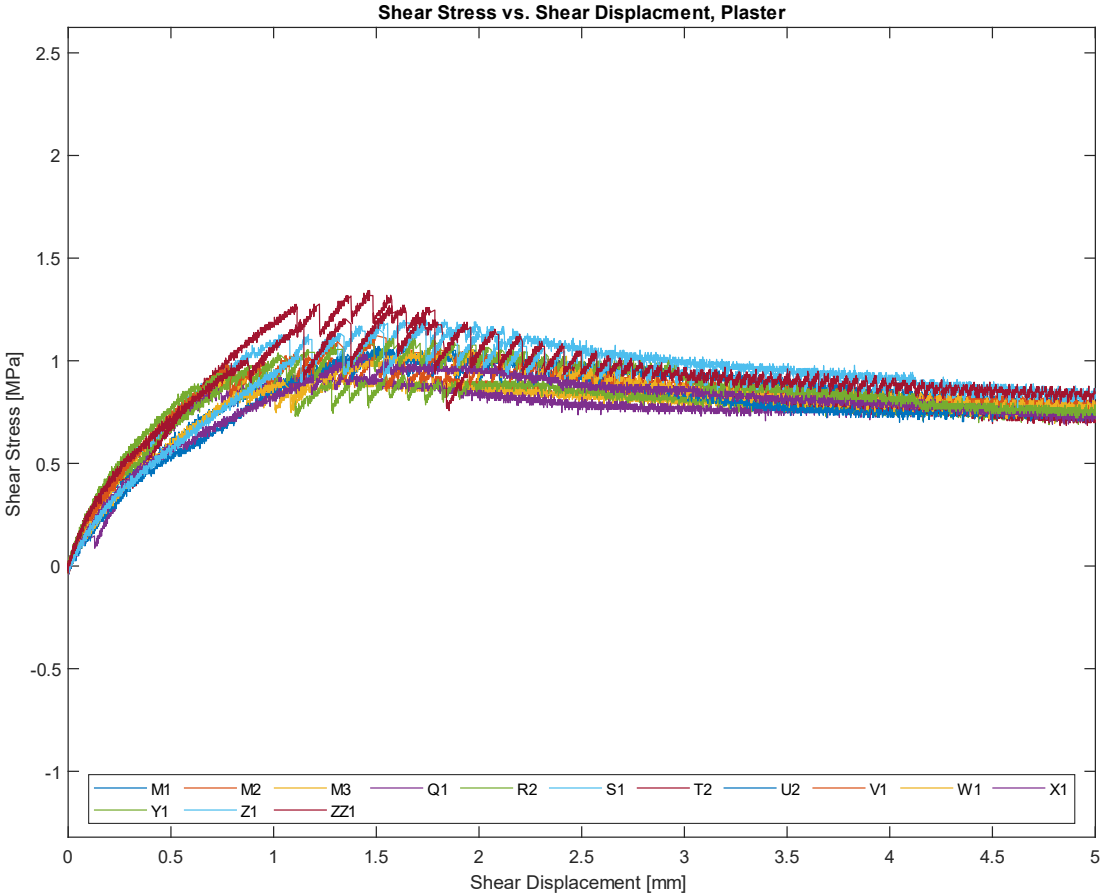


FIGURE 11: THE SHEAR STRESS RESULTS FROM ALL THE PLASTER TEST PERFORMED AT 1 MPA NORMAL LOAD, WITH EACH SAMPLE BEING ROTATED BY 30 DEGREES FROM THE PREVIOUS TEST (EXCEPT M1, M2, AND M3, WHO ALL HAD THE SAME ORIENTATION). A MAJORITY OF THE SAMPLES DISPLAYED A STICK-SLIP LIKE BEHAVIOR DURING TESTING.

Figure 11 shows the shear test results for the plaster samples when the samples were rotated. Rotating the samples by 30 degrees in between tests results in a difference in peak shear stress of about 0.4 MPa between the highest peak shear stress and the lowest. Again, a majority of the tests displayed the “sawtooth” pattern mentioned earlier, before reaching a residual shear stress that was relatively close together towards the end of the tests.

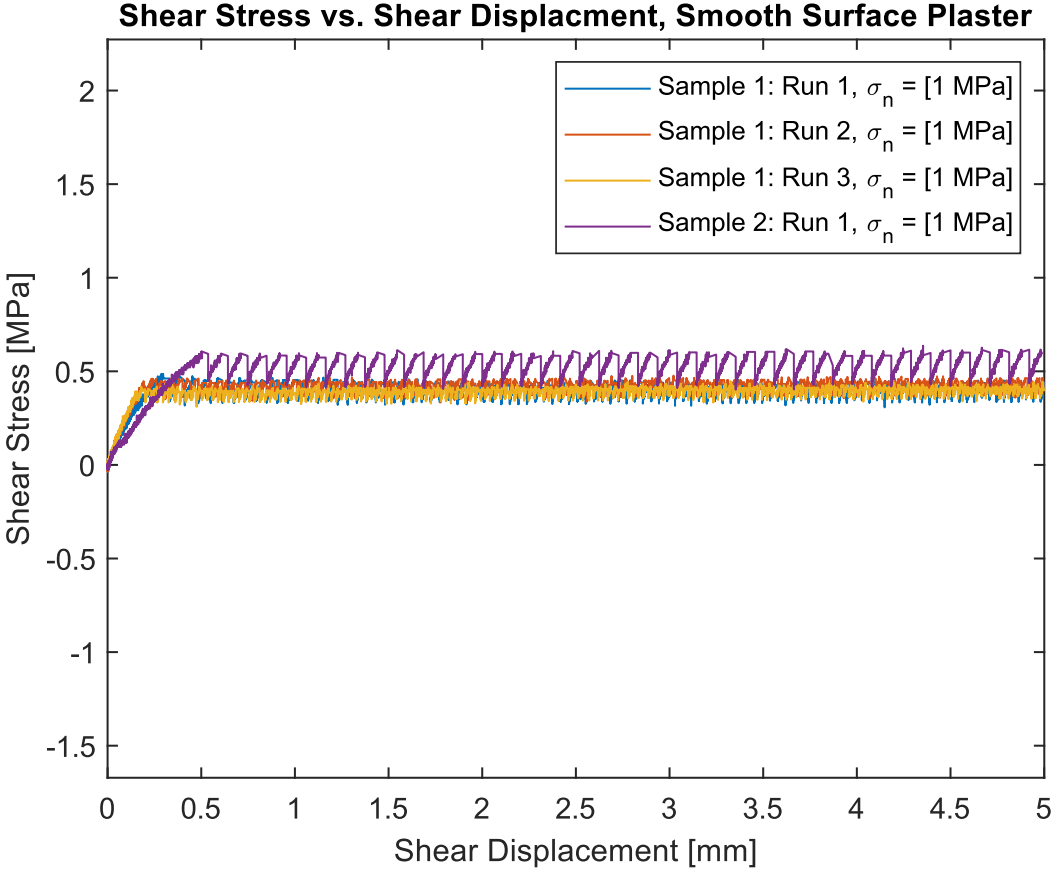


FIGURE 12: THE RESULTS FROM SHEAR TESTS PERFORMED ON TWO PLASTER SAMPLES WITH A VERY SMOOTH SURFACE. ONE OF THE SAMPLES WAS RUN THREE TIMES CONSECUTIVELY.

Figure 12 shows the results from shear tests done on two plaster samples that had very smooth surfaces, to see how having no asperities would affect the results. As can be seen the results from the first sample, which was run three times, the results are very consistent between tests. The result from the second sample is slightly higher in terms of peak shear stress, but otherwise displays similar behavior as the first sample.

The thing to note with these tests is that, while they display a similar sawtooth pattern as the other plaster tests, with a completely smooth and level surface the pattern doesn’t attenuate.

Instead, returning again and again to shear stress levels at or just below peak shear stress levels.

4.3 JRC

Table 7 & 8 give a complete overview of the JRC values for all the samples, both the JRC back calculated from the shear tests and the JRC values calculated using the various formulas. As can also be seen in Fig. 13a, the back calculated JRC values are quite a bit higher than the JRC values calculated from the photogrammetry profiles. There is also a noticeable difference between the top and bottom half JRC values, in some cases more than double.

Also noticeable, is the JRC values for the smooth surfaced sample. Given the flat nature of the joint surface, one could expect that the JRC value would be close to 0. However, looking at the back calculated JRC value, it becomes apparent that the JRC value is very much not 0, instead varying between 4 and 9.5. Looking at the photogrammetric JRC values for the smooth sample, things look more like one would expect. Obviously the formulas based around the Z_2 parameter end up returning negative JRC values, but that is expected, as does the SF formula. The R_p formula however, does return a JRC value of 0.

TABLE 7: OVERVIEW OF THE JRC VALUES FOR ALL THE SAMPLES, PART 1. * VALUE EITHER EXCEEDED MAX JRC VALUE OF 20, OR MIN VALUE OF 0. A-G CORRESPONDS TO FORMULA 18-24 IN ORDER.

Sample	Normal Load [MPa]	Z2						
		Back calculated JRC			Yu & Vayssade ^a		Yang et al. ^b	
		Min JRC	Avg. JRC	Max JRC	Bottom	Top	Bottom	Top
M1	1	10.95	12.59	14.02	2.55	6.7	0*	6.39
M2	1	9.3	10.54	12.33	8.41	8.42	8.98	8.89
M3	1	7.27	8.69	9.86	6.27	11.24	6.17	12.12
N1	2	10.98	12.2	13.23	7.47	6.12	7.63	5.76
O1	3	18.01	18.96	20	6.2	5.17	6.07	4.45
Q1	1	6.42	9.02	10.49	7.71	5.02	8.1	4.16
R2	1	11.14	12.62	14.32	6.46	6.68	6.42	6.71
S1	1	12.75	14.2	15.67	9.93	10.16	10.52	10.68
T2	1	20*	20*	20*	7.38	12.39	7.42	12.8
U2	1	12.31	13.93	15.43	5.81	8.85	5.36	9.48
V1	1	12.29	13.78	15.33	5.76	6.41	5.22	6.32
W1	1	10.33	11.84	13.91	5.78	3.57	5.4	2.64
X1	1	11.28	12.74	14.45	9.07	7.93	9.84	7.82
Y1	1	13.09	14.33	15.68	7.92	7.89	8.19	8.16
Z1	1	11.1	12.71	13.98	8.76	6.79	9.23	6.49
ZZ1	1	13.88	15.28	16.77	8.26	6.34	8.73	6.2
SA1	1	9.92	10.65	11.4	4.95	4.43	3.97	3.19
SA2	3	8.06	8.6	9.29	7.59	14.04	7.96	14.46
SA3	2	4.64	4.96	5.32	11.02	11.41	11.51	11.91
SA4	1	11.55	12.57	14.11	20*	13.79	20*	14.25
SB1	1	7.47	8.51	10.29	15.73	14.06	16.52	14.25
SB2	1	3.32	4.67	5.94	4.11	10.71	2.46	11.51
SB3	1	2.7	4.07	4.98	7.29	6.27	7.6	6.19
Smooth	1	3.97	6.37	9.46	0*	0*	0*	0*

TABLE 8: OVERVIEW OF THE JRC VALUES, PART 2. * VALUE EITHER EXCEEDED MAX JRC VALUE OF 20, OR MIN VALUE OF 0. A-G CORRESPONDS TO FORMULA 18-24 IN ORDER.

Sample	Z2				SF		R _p			
	Tatone & Grasselli ^c		Jang et al. ^d		Liu et al. ^e		Yu & Vayssade ^f		Tatone & Grasselli ^g	
	Bottom	Top	Bottom	Top	Bottom	Top	Bottom	Top	Bottom	Top
M1	2.43	7.05	3.4	8.02	0*	6.56	2.64	6.73	3.3	7.46
M2	8.88	8.85	9.84	9.81	8.44	8.01	8.41	8.42	9.33	9.26
M3	6.73	11.54	7.72	12.43	5.65	12.81	6.31	11.2	7.14	12.11
N1	7.9	6.52	8.87	7.5	7.62	6.34	7.49	6.16	8.33	6.98
O1	6.65	5.54	7.65	6.54	5.44	3.94	6.24	5.22	7.08	5.97
Q1	8.19	5.37	9.16	6.36	8.71	5.7	7.73	5.08	8.62	5.83
R2	6.92	7.14	7.91	8.13	7.15	7.43	6.49	6.71	7.35	7.58
S1	10.25	10.43	11.17	11.34	10.44	10.54	9.9	10.13	10.72	10.84
T2	7.78	12.4	8.75	13.23	8.21	13.21	7.4	12.33	8.19	12.62
U2	6.21	9.29	7.2	10.25	6.46	9.38	5.86	8.84	6.67	9.77
V1	6.13	6.86	7.12	7.85	4.57	5.75	5.81	6.44	6.59	7.27
W1	6.2	3.7	7.2	4.68	6.12	4.57	5.83	3.65	6.62	4.31
X1	9.55	8.23	10.5	9.17	9.5	8.42	7.69	7.94	9.84	8.67
Y1	8.34	8.31	9.3	9.27	8.77	9.44	7.93	7.9	8.79	8.76
Z1	9.16	7.14	10.11	8.11	8.55	6.49	8.75	6.82	9.6	7.58
ZZ1	8.71	6.78	9.67	7.77	8.33	6.28	8.27	6.37	9.18	7.22
SA1	5.26	4.71	6.26	5.71	0*	0*	5	4.49	5.73	5.2
SA2	8.07	13.89	9.05	14.67	7.32	13	7.6	13.96	8.51	14.1
SA3	11.2	11.56	12.08	12.43	7.53	8.35	10.98	11.37	11.55	11.9
SA4	20*	13.68	20*	14.47	19.49	11.99	20*	13.7	19.88	13.92
SB1	16.1	13.82	16.76	14.59	16.19	14.57	16.65	13.97	15.6	13.47
SB2	4.31	11.03	5.3	11.93	2.07	10.87	4.18	12.67	4.83	11.46
SB3	7.78	6.73	8.76	7.73	4.56	2.84	7.31	6.31	8.19	7.14
Smooth	0*	0*	0*	0*	0*	0*	0*	0*	0.2	0.13

4.4 Anisotropy

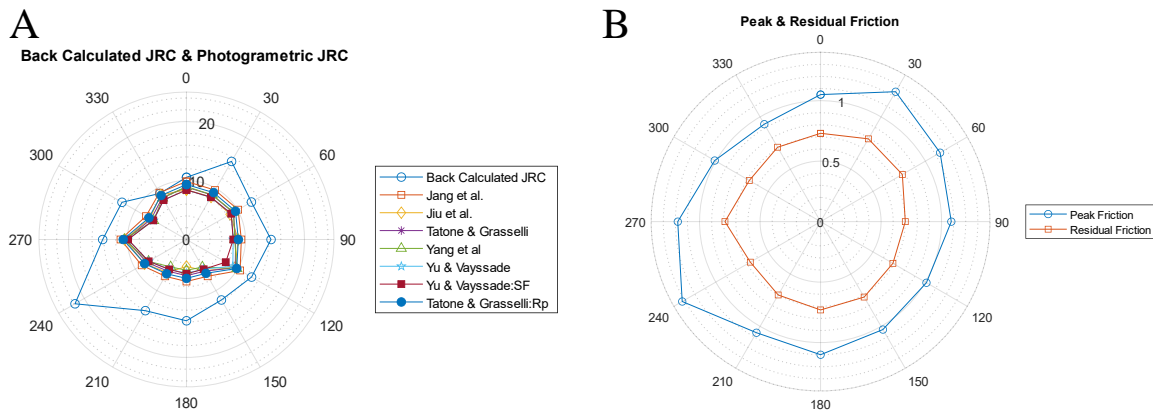


FIGURE 13:A) THE JRC BACK CALCULATED FROM THE SHEAR TESTS COMPARED TO THE JRC CALCULATED FROM THE PHOTOGRAMMETRIC DATA USING THE DIFFERENT FORMULAS. B) THE PEAK FRICTION VALUE AND RESIDUAL FRICTION VALUE FOR THE ROTATIONAL PLASTER TESTS.

Figure 13a shows the comparison between the JRC calculated from the shear tests using formula (3) and the JRC calculated using the different formulas on the rotated plaster samples to investigate the degree of anisotropy. Looking at the results it's clear that there is a significant difference between the back calculated JRC values and the JRCs calculated from the photogrammetry. With the exception of two points, the back calculated JRC values are noticeably higher than the JRC values calculated from the photogrammetry. Comparing the photogrammetric JRCs with each other shows that there isn't much difference between the different formulas in terms of calculating JRC.

Looking at the figure again, it also becomes clear that there is a significant degree of anisotropy in the back calculated JRC values, with the value for the 240-degree shear direction maxing out the scale at a JRC value of 20. There is also a degree of anisotropy for the photogrammetric JRC values, where the 120-degree and 270-degree results being noticeably higher than the surrounding values.

Figure 13b shows that there is also a degree of anisotropy present when looking at the peak friction values for the rotational plaster tests, again favoring the 240-degree shear direction. When it comes to the residual friction values there is hardly any anisotropy to speak of, a result that is supported by looking at the shear stress values towards the end of Figure 11.

4.5 Photogrammetry

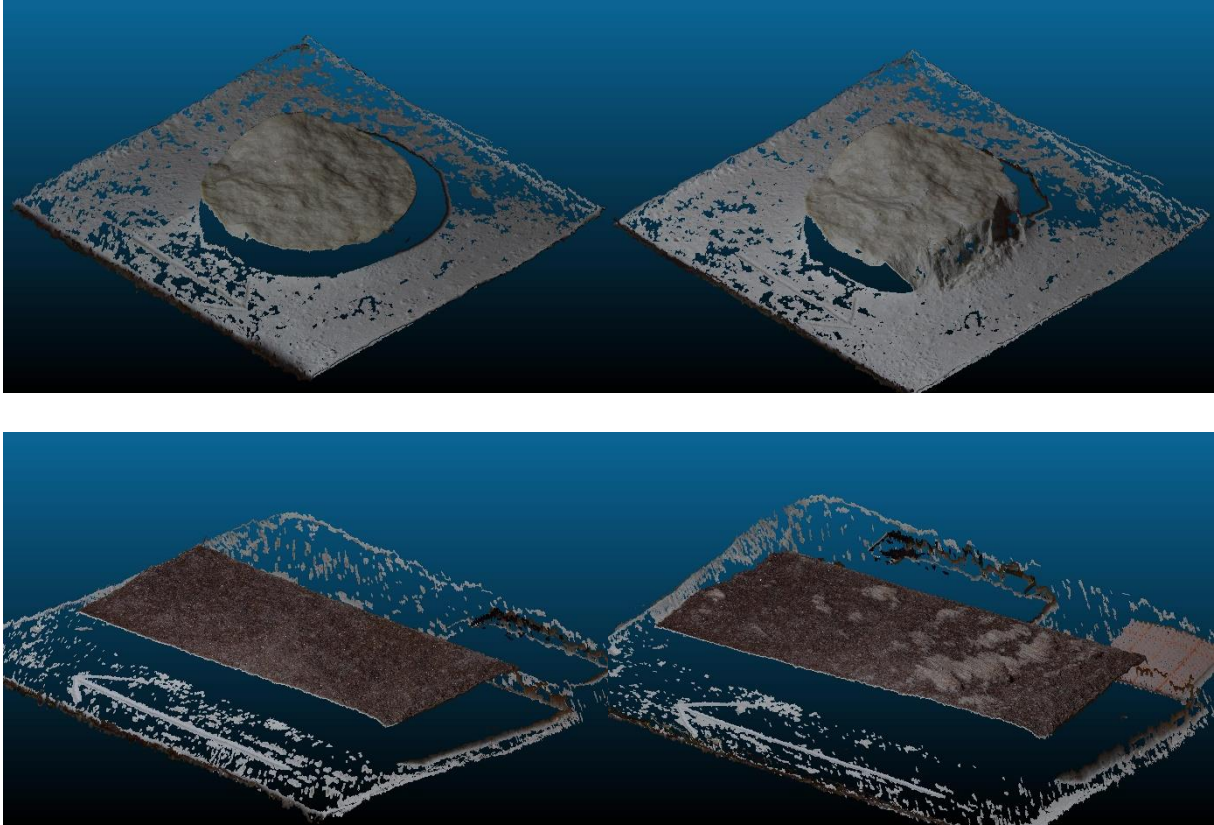


FIGURE 14: BEFORE AND AFTER 3D MODELS OF A PLASTER AND SANDSTONE SAMPLE CREATED USING MICMAC.

As far as the quality of the 3D models produced using MicMac, at least from a visual standpoint they appear to be excellent. Each point cloud produced consists of between 12 and 18 million points and have a high enough spatial resolution to allow for easy identification of the areas affected by the shearing, especially on the sandstone samples (as can be seen in Figure 14). The spatial accuracy of the models appears to be very good in the XY plane (sub mm scale), but this is to be expected considering the fact that XY scale is defined using GCPs during the photogrammetry process.

Where the problems start however is with the scaling in the Z-axis. Figure 15a & b shows two 3D models of the same sample, one before shearing (red) and one after shearing (green). The two models have been aligned with each other using CloudCompare, a free software that can be used to view mesh clouds. What the images show is that there is a discrepancy between the two models of several millimeters in the vertical axis. Figure 15c shows the results using

CloudCompare's cloud distance tool, revealing that there is a roughly 2.5 mm difference between the two models, with a maximum discrepancy of around 4-4.5 mm on the surface of the sample.

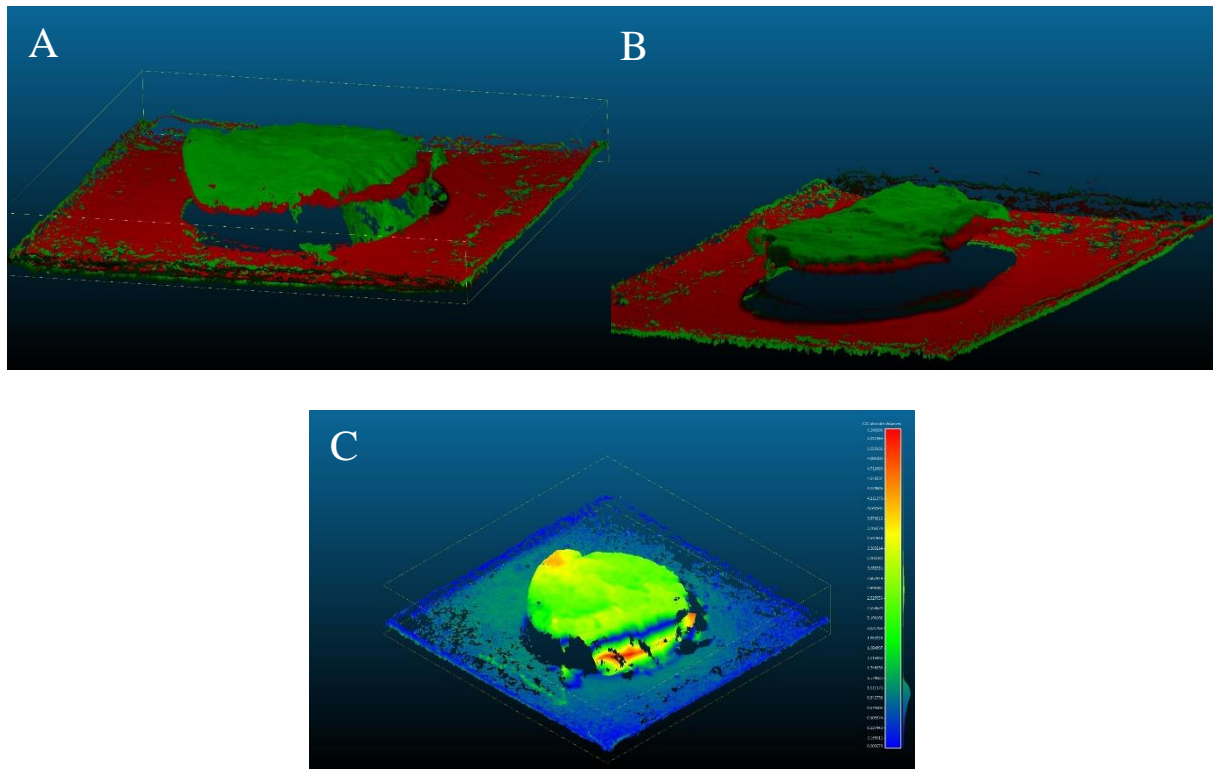


FIGURE 15: A & B) COMPARING THE BEFORE (RED) AND AFTER (GREEN) 3D MODELS OF ONE OF THE PLASTER SAMPLES HIGHLIGHTS A SIGNIFICANT DIFFERENCE BETWEEN THE TWO MODELS IN THE VERTICAL AXIS. C) MEASURING THE DISTANCE BETWEEN THE TWO MODELS USING CLOUDCOMPARES CLOUD DISTANCE TOOL.

In an attempt to identify the cause of the Z-axis scaling issue a couple of tests were performed using a roughly 75 mm x 75 mm piece of 80 grit sandpaper glued to a 100 mm x 100 mm piece of aluminum plate. In the first test a series of images was taken of the sandpaper and then the focus of the lens was pulled far out of focus and then returned to focus, before a second set of images was taken. Both of these image sets were then run through the MicMac process described earlier, and the resulting 3D-models aligned using CloudCompare and then the distance between the two were measured (Figure 16a). For the second test nothing was done to the camera between the two image sets.

Looking at the result of the first test it becomes apparent that there is very little distance between the two models, only 8-150 μm , ignoring some artifacts along the edges. For the

second test there actually is more distance between the two models, this time measuring between 10 μm and 500 μm .

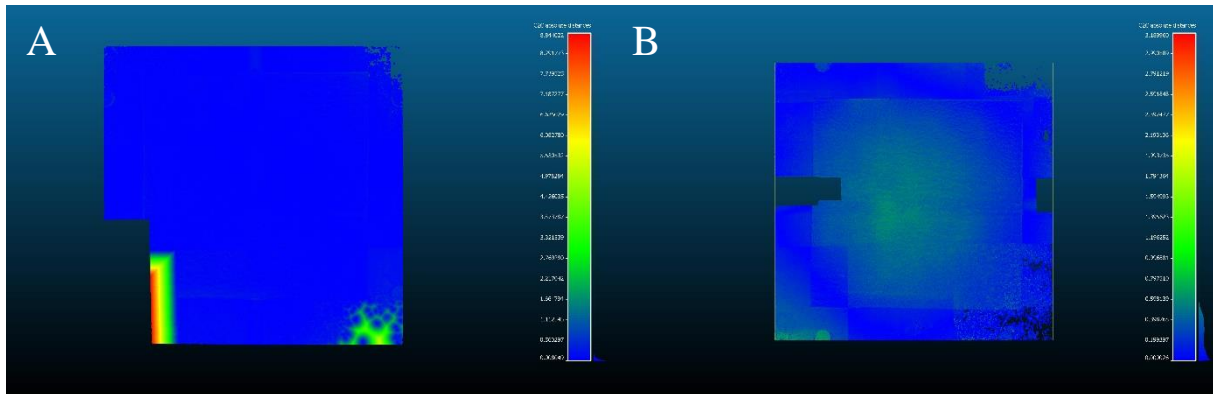


FIGURE 16: A) THE DISTANCE BETWEEN THE TWO MODELS AFTER DEFOCUSING AND REFOCUSING THE LENS FOCUS. B) THE DISTANCE WHEN NOTHING WAS DONE TO THE CAMERA.

5.0 Discussion

5.1 Issues with the shear tests

So, as can clearly be seen in the results from the shear tests, the majority of the plaster samples exhibited what appears to be stick-slip behavior, where the halves would move a little bit and then stop until the shear stress becomes high enough for the two halves to slip again. This happened again and again, gradually attenuating until relatively smooth sliding was achieved. Now, as to the cause for this behavior there are a couple options. First, there is the possibility that the test rig wasn't strong enough to handle the test. Either due to the motor applying the shear force not being strong enough to ensure smooth shearing after peak shear stress has been achieved, or secondly, because the shear box itself not being stiff enough to keep from flexing during the test and thereby absorbing some of the stress itself.

As for evidence supporting this conclusion, there isn't a lot apart from the stick-slip behavior itself, but that could be caused by other factors in the test. One way to test the degree to which the motor affected the tests would be to replace it with a more powerful unit and seeing if that resolves the issue. Alternatively, one could try using two very smooth pieces of steel and see if they slide smoothly.

As far as shear box flex is concerned, that is a bit harder to test. It would probably involve mounting a lot of sensors around the shear box, and then applying shear force on a solid block of steel to see how much flex there is.

There is also evidence pointing towards other factors than there being an issue with the test setup, the main one being the fact that the sandstone samples don't exhibit the same stick-slip behavior as the plaster samples do, despite being on either side of the plaster samples in terms of compressive strength. This suggests that the issue is with the plaster samples instead.

As far as the plaster samples are concerned there are several possible factors that could affect the results. A big one is how the samples themselves were produced. In order to accommodate a relatively tight testing schedule, the samples were only given roughly 24 hours to dry in a room temperature environment. A fact that may have allowed the plaster to behave in a more ductile manner due to residual water in the pore spaces within the samples. A possible solution to this potential problem would be to either let the samples dry for a longer period of time, or to use an oven or dehumidifier to help reduce the water content of the sample faster. Another possible reason for the plaster samples behavior during testing is the silicone grease used to ensure separation during the molding of the samples. While being a lubricating substance, the grease is rather sticky to the touch, a fact that might have affected the samples during testing if not sufficiently removed from the contact surfaces. It is possible that some of the grease was left behind during the cleaning of the sample surfaces, in an attempt to preserve the micro-scale features from abrasion during cleaning. Unfortunately, short of using a different type of mold release agent, which may come with its own set of potential issues, there isn't really any way to alleviate the issue caused by the grease without also losing some of the finer details of the joint surface in the process. This is just an unfortunate side effect of the soft nature of plaster itself.

5.2 Issues with the photogrammetry

The shear tests were not the only source of issues during this thesis. The perhaps bigger issue is with the vertical scaling of the model produced using MicMac, which are the source of the profiles used to calculate the JRC values. The fact that the vertical scaling varies from image set to image set means that it becomes functionally impossible to make comparisons between the results. It also means that it's difficult to know how close the models are to reality.

Now, as far as the cause for the discrepancy it appears that the position of the light relative to the sample that is getting photographed has a significant impact on the final result. Given that the results of the testing shown in Figure 14 shows that changes in lens focus between tests has a minimal impact on the vertical scaling, which is good considering that the camera lens needed refocusing every time the camera was turned on, that really only leave the lighting as a likely source of issues with the photogrammetric setup. While the position of the samples was kept pretty consistent (to within a millimeter or two), the light used during testing was not fixed, instead using an improvised mounting point that had the potential to change in between tests. This means that there is a chance that the position and angle of the light could have changed slightly between each photo session, possibly resulting in the changes in vertical scaling observed.

The other alternative is that the problem originates from MicMac. Now, given that, if the issues experienced during the work for this thesis was widespread, it likely would get fixed by the developers, that leaves user error as the most likely cause of any problems caused on the software side. With limited documentation (at least in English), it is difficult to determine which setting, if any might be causing an issue.

6 Conclusions

So then, in the end what conclusions can be drawn from the results of the work that has been done? How viable is using photogrammetry derived from MicMac in order to determine JRC? Well, glancing on the results themselves it seems that using MicMac for this purpose doesn't work. With the JRC values derived from the MicMac photogrammetry either overestimating or underestimating compared to the back calculated JRC values, and with the JRC values of the top and bottom half of the same joint also wildly varying when one would expect them to be mostly the same, it leaves one with only one logical conclusion. Using MicMac in the process of determining JRC does not work.

However, when looking deeper at the results it becomes apparent that the quality of the data produced is highly questionable. It becomes clear that there are significant issues with both the shear test results, particularly for the plaster samples, and with the vertical scaling of the models produced using MicMac. As a result of this it becomes clear that it is virtually impossible to conclude one way or the other in regard to the viability of using MicMac to determine JRC.

In the end there are only a couple conclusions that can be made from the work that has been done.

- Care needs to be taken when working with plaster to ensure that the samples are allowed a sufficient degree of drying before being sheared. This can be accomplished either by longer drying times or the use of things like ovens to speed up the drying process. Doing this will hopefully help reduce the stick-slip behavior observed during shear testing.
- When acquiring images used for photogrammetry, it is very important that the setup used is kept constant. This is especially important if one wishes to compare one image set with another. It appears that the positioning of any additional lighting used can have a significant impact on the z-axis scaling of the models produced.
- MicMac is a powerful program given its open-source nature and has proven itself to have uses in an academic setting. However, due to the somewhat lacking nature of the documentation and its non-user-friendly interface, it is perhaps not the best suited program for beginners looking to get into photogrammetry.

References

- BABANOURI, N., NASAB, S. K., BAGHBANAN, A. & MOHAMADI, H. R. 2011. Over-consolidation effect on shear behavior of rock joints. *International journal of rock mechanics and mining sciences*, 48, 1283-1291.
- BANDIS, S., LUMSDEN, A. & BARTON, N. Experimental studies of scale effects on the shear behaviour of rock joints. *International journal of rock mechanics and mining sciences & geomechanics abstracts*, 1981. Elsevier, 1-21.
- BARTON, N. & BANDIS, S. 1982. Effects Of Block Size On The Shear Behavior Of Jointed Rock. *23rd US Symp. on Rock Mechanics*. Berkley: American Rock Mechanics Association.
- BARTON, N. & CHOUBEY, V. J. R. M. 1977. The shear strength of rock joints in theory and practice. 10, 1-54.
- BARTON, N. J. E. G. 1973. Review of a new shear-strength criterion for rock joints. 7, 287-332.
- BEER, A., STEAD, D. & COGGAN, J. 2002. Technical note estimation of the joint roughness coefficient (JRC) by visual comparison. *Rock mechanics and rock engineering*, 35, 65-74.
- BELEM, T., HOMAND-ETIENNE, F. & SOULEY, M. 2000. Quantitative parameters for rock joint surface roughness. *Rock mechanics and rock engineering*, 33, 217-242.
- BISTACCHI, A., GRIFFITH, W. A., SMITH, S. A., DI TORO, G., JONES, R. & NIELSEN, S. 2011. Fault roughness at seismogenic depths from LIDAR and photogrammetric analysis. *Pure and Applied Geophysics*, 168, 2345-2363.
- BROWN, S. R. & SCHOLZ, C. H. 1985. Broad bandwidth study of the topography of natural rock surfaces. *Journal of Geophysical Research: Solid Earth*, 90, 12575-12582.
- CANDELA, T., RENARD, F., BOUCHON, M., BROUSTE, A., MARSAN, D., SCHMITTBUHL, J. & VOISIN, C. 2009. Characterization of fault roughness at various scales: Implications of three-dimensional high resolution topography measurements. *Mechanics, structure and evolution of fault zones*. Springer.
- DAI, F., FENG, Y. & HOUGH, R. 2014. Photogrammetric error sources and impacts on modeling and surveying in construction engineering applications. *Visualization in Engineering*, 2, 1-14.
- DAI, F. & LU, M. 2013. Three-dimensional modeling of site elements by analytically processing image data contained in site photos. *Journal of construction engineering and management*, 139, 881-894.
- EL-SOUDANI, S. 1978. Profilometric analysis of fractures. *Metallography*, 11, 247-336.
- F.D.PATTON 1966. Multiple modes of shear failure In rock. In: ENGINEERING, I. S. F. R. M. A. R. (ed.) *1st ISRM Congress, 25 September-1 October*. Lisbon, Portugal: International Society for Rock Mechanics and Rock Engineering.
- GALLAND, O., BERTELSEN, H. S., GULDSTRAND, F., GIROD, L., JOHANNESSEN, R. F., BJUGGER, F., BURCHARDT, S. & MAIR, K. 2016. Application of open-source photogrammetric software MicMac for monitoring surface deformation in laboratory models. *Journal of Geophysical Research: Solid Earth*, 121, 2852-2872.
- GRASSELLI, G. 2001. Shear strength of rock joints based on quantified surface description. EPFL.
- GRASSELLI, G. & EGGER, P. 2003. Constitutive law for the shear strength of rock joints based on three-dimensional surface parameters. *International Journal of Rock Mechanics and Mining Sciences*, 40, 25-40.
- GRASSELLI, G., WIRTH, J. & EGGER, P. 2002. Quantitative three-dimensional description of a rough surface and parameter evolution with shearing. *International Journal of Rock Mechanics and Mining Sciences*, 39, 789-800.

- HSIUNG, S., GHOSH, A., AHOLA, M. & CHOWDHURY, A. Assessment of conventional methodologies for joint roughness coefficient determination. The 34th US Symposium on Rock Mechanics (USRMS), 1993. American Rock Mechanics Association.
- HUANG, S., OELFKE, S. & SPECK, R. Applicability of fractal characterization and modelling to rock joint profiles. International journal of rock mechanics and mining sciences & geomechanics abstracts, 1992. Elsevier, 89-98.
- INDRARATNA, B. 1990. Development and applications of a synthetic material to simulate soft sedimentary rocks. *Geotechnique*, 40, 189-200.
- INDRARATNA, B., HAQUE, A. & AZIZ, N. 1998. Laboratory modelling of shear behaviour of soft joints under constant normal stiffness conditions. *Geotechnical & Geological Engineering*, 16, 17-44.
- INDRARATNA, B., THIRUKUMARAN, S., BROWN, E. & ZHU, S.-P. 2015. Modelling the shear behaviour of rock joints with asperity damage under constant normal stiffness. *Rock Mechanics and Rock Engineering*, 48, 179-195.
- INDRARATNA, B., THIRUKUMARAN, S., BROWN, E. T., PREMADASA, W. N. & WINTON GALE, W. 2014. A technique for three-dimensional characterisation of asperity deformation on the surface of sheared rock joints.
- JANG, H.-S., KANG, S.-S. & JANG, B.-A. 2014. Determination of joint roughness coefficients using roughness parameters. *Rock mechanics and rock engineering*, 47, 2061-2073.
- JESSELL, M. W., COX, S. J., SCHWARZE, P. & POWER, W. L. 1995. The anisotropy of surface roughness measured using a digital photogrammetric technique. *Geological Society, London, Special Publications*, 92, 27-37.
- KIM, D. H. H. 2016. *Study on the Accuracy of Rock Surface Roughness Data using Close Range Photogrammetry*. Doctor of Philosophy (PhD), Griffith School of Engineering.
- KULATILAKE, P., SHOU, G., HUANG, T. & MORGAN, R. New peak shear strength criteria for anisotropic rock joints. International Journal of Rock Mechanics and Mining Sciences & Geomechanics Abstracts, 1995. Elsevier, 673-697.
- LANARO, F. 2000. A random field model for surface roughness and aperture of rock fractures. *International Journal of Rock Mechanics and Mining Sciences*, 37, 1195-1210.
- LEE, D.-H. & JUANG, C. H. 1991. A new technique for measuring the roughness profile of rock joints. *Geotechnical testing journal*, 14, 320-322.
- LEE, H.-S. & AHN, K.-W. 2004. A prototype of digital photogrammetric algorithm for estimating roughness of rock surface. *Geosciences Journal*, 8, 333-341.
- LEE, Y.-H., CARR, J., BARR, D. & HAAS, C. The fractal dimension as a measure of the roughness of rock discontinuity profiles. International journal of rock mechanics and mining sciences & geomechanics abstracts, 1990. Elsevier, 453-464.
- LI, Y. & ZHANG, Y. 2015. Quantitative estimation of joint roughness coefficient using statistical parameters. *International Journal of Rock Mechanics and Mining Sciences*, 100, 27-35.
- LIU, R., LOU, S., LI, X., HAN, G. & JIANG, Y. 2020. Anisotropic surface roughness and shear behaviors of rough-walled plaster joints under constant normal load and constant normal stiffness conditions. *Journal of Rock Mechanics and Geotechnical Engineering*, 12, 338-352.
- LIU, X., ZHU, W., YU, Q., CHEN, S. & LI, R. 2017. Estimation of the joint roughness coefficient of rock joints by consideration of two-order asperity and its application in double-joint shear tests. *Engineering Geology*, 220, 243-255.
- LUCIEER, A., JONG, S. M. D. & TURNER, D. 2014. Mapping landslide displacements using Structure from Motion (SfM) and image correlation of multi-temporal UAV photography. *Progress in Physical Geography*, 38, 97-116.
- MAERZ, N. H., FRANKLIN, J. A. & BENNETT, C. P. Joint roughness measurement using shadow profilometry. International Journal of Rock Mechanics and Mining Sciences & Geomechanics Abstracts, 1990. Elsevier, 329-343.
- MANDELBROT, B. B. 1983. *The fractal geometry of nature*, New York, Freeman.

- MICHELETTI, N., CHANDLER, J. H. & LANE, S. N. 2015. Investigating the geomorphological potential of freely available and accessible structure-from-motion photogrammetry using a smartphone. *Earth Surface Processes and Landforms*, 40, 473-486.
- MOSBRUCKER, A. R., MAJOR, J. J., SPICER, K. R. & PITLICK, J. 2017. Camera system considerations for geomorphic applications of SfM photogrammetry. *Earth Surface Processes and Landforms*, 42, 969-986.
- NEWLAND, P. & ALLELY, B. 1957. Volume changes in drained triaxial tests on granular materials. *Geotechnique*, 7, 17-34.
- NILSSON, M., EDELBRO, C. & SHARROCK, G. Small scale joint surface roughness evaluation using digital photogrammetry. Eurock 2012: Rock Engineering and Technology for Sustainable Underground Construction 25/05/2012-27/05/2012, 2012.
- POROPAT, G. 2009. Measurement of surface roughness of rock discontinuities. *Rock Engineering in Difficult Conditions*.
- ROUSSEAU, B., RIVARD, P., MARACHE, A., BALLIVY, G. & RISS, J. 2012. Limitations of laser profilometry in measuring surface topography of polycrystalline rocks. *International journal of rock mechanics and mining sciences (Oxford, England : 1997)*, 52, 56-60.
- STURZENEGGER, M. & STEAD, D. 2009. Close-range terrestrial digital photogrammetry and terrestrial laser scanning for discontinuity characterization on rock cuts. *Engineering Geology*, 106, 163-182.
- TATONE, B. S. & GRASSELLI, G. 2009. A method to evaluate the three-dimensional roughness of fracture surfaces in brittle geomaterials. *Review of scientific instruments*, 80, 125110.
- TATONE, B. S. & GRASSELLI, G. 2010. A new 2D discontinuity roughness parameter and its correlation with JRC. *International Journal of Rock Mechanics and Mining Sciences*, 47, 1391-1400.
- TSE, R. & CRUDEN, D. Estimating joint roughness coefficients. *International journal of rock mechanics and mining sciences & geomechanics abstracts*, 1979. Elsevier, 303-307.
- UNAL, M., YAKAR, M. & YILDIZ, F. Discontinuity surface roughness measurement techniques and the evaluation of digital photogrammetric method. *Proceedings of the 20th international congress for photogrammetry and remote sensing, ISPRS*, 2004. Citeseer, 1103-1108.
- WESTOBY, M. J., BRASINGTON, J., GLASSER, N. F., HAMBREY, M. J. & REYNOLDS, J. M. 2012. 'Structure-from-Motion' photogrammetry: A low-cost, effective tool for geoscience applications. *Geomorphology*, 179, 300-314.
- WICKENS, E. & BARTON, N. 1971. The application of photogrammetry to the stability of excavated rock slopes. *The Photogrammetric Record*, 7, 46-54.
- YANG, Z., LO, S. & DI, C. 2001. Reassessing the joint roughness coefficient (JRC) estimation using Z 2. *Rock mechanics and rock engineering*, 34, 243-251.
- YU, X. & VAYSSADE, B. Joint profiles and their roughness parameters. *International journal of rock mechanics and mining sciences & geomechanics abstracts*, 1991. Elsevier, 333-336.

Appendix I: Surface profiles in shear direction

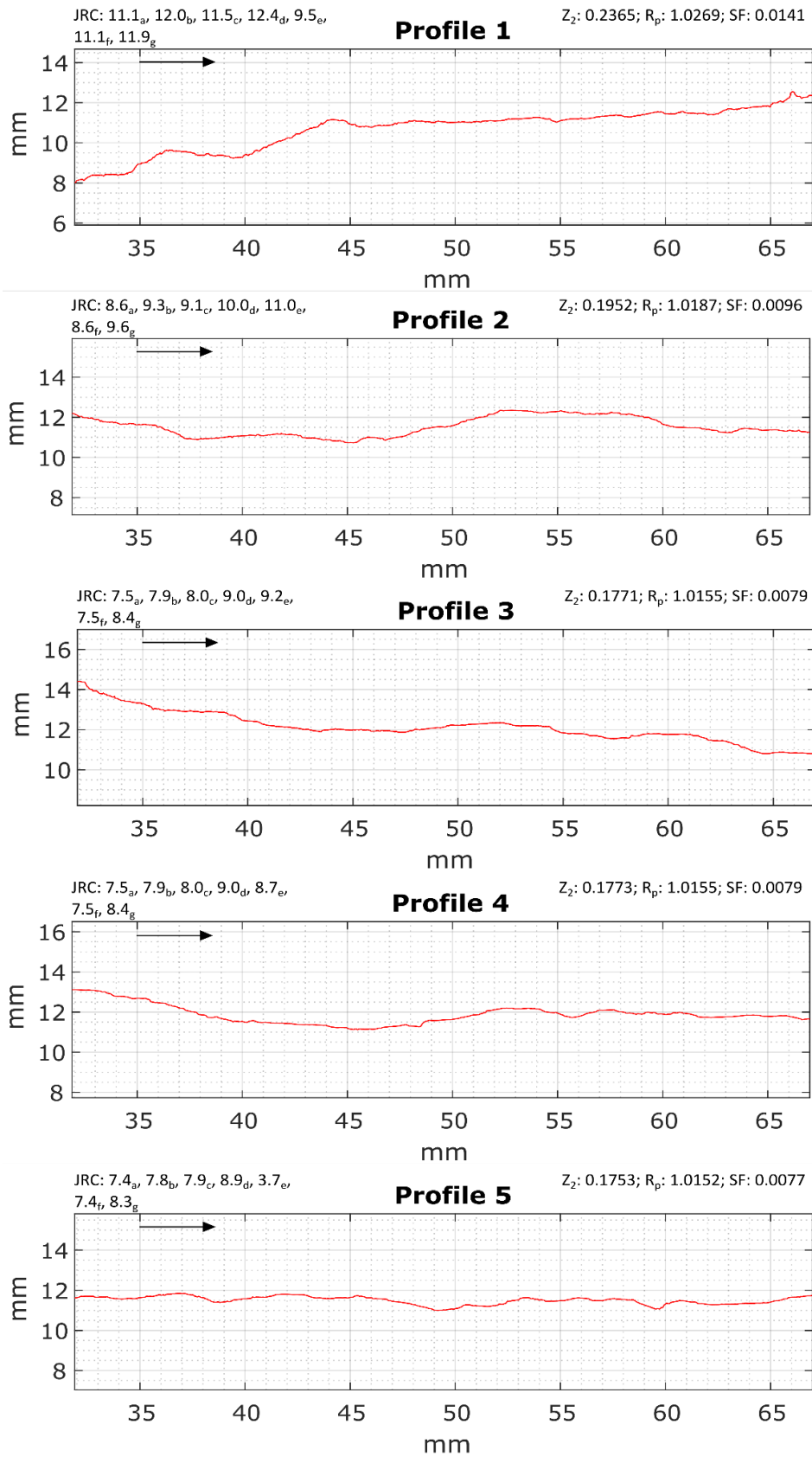


FIGURE 17: M2 PROFILES BOTTOM

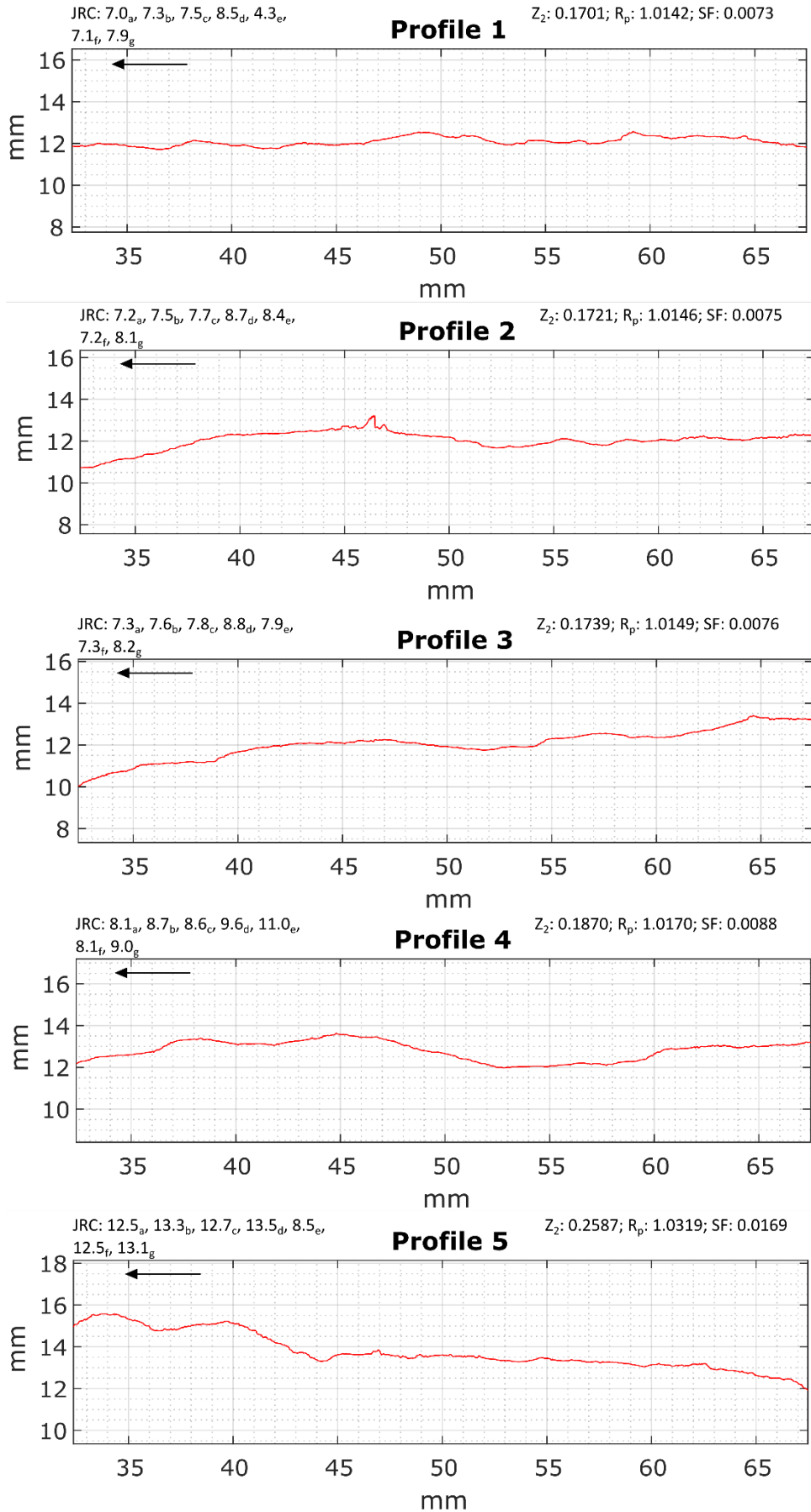


FIGURE 18: M2 PROFILES TOP

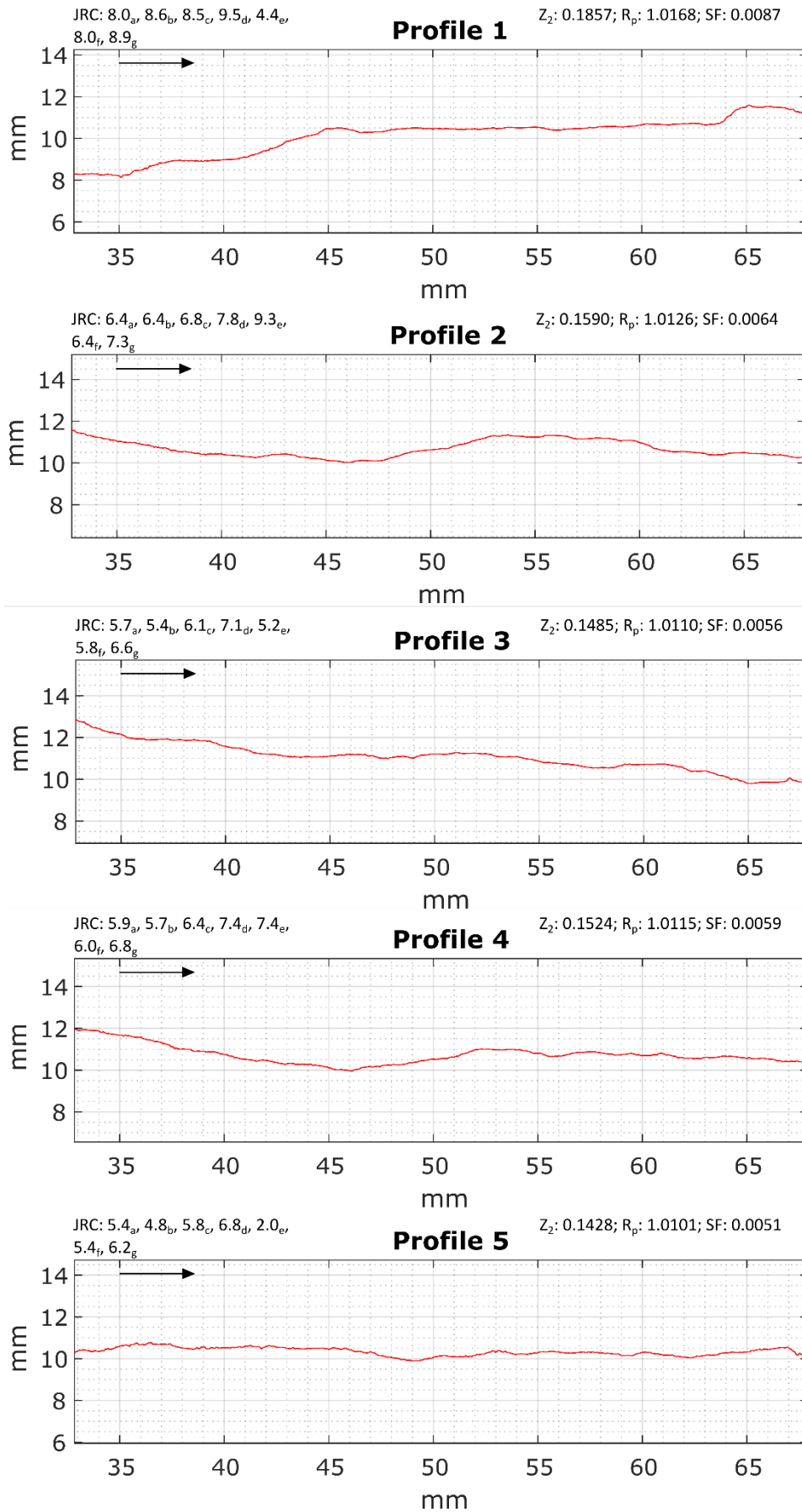


FIGURE 19: M3 PROFILES BOTTOM

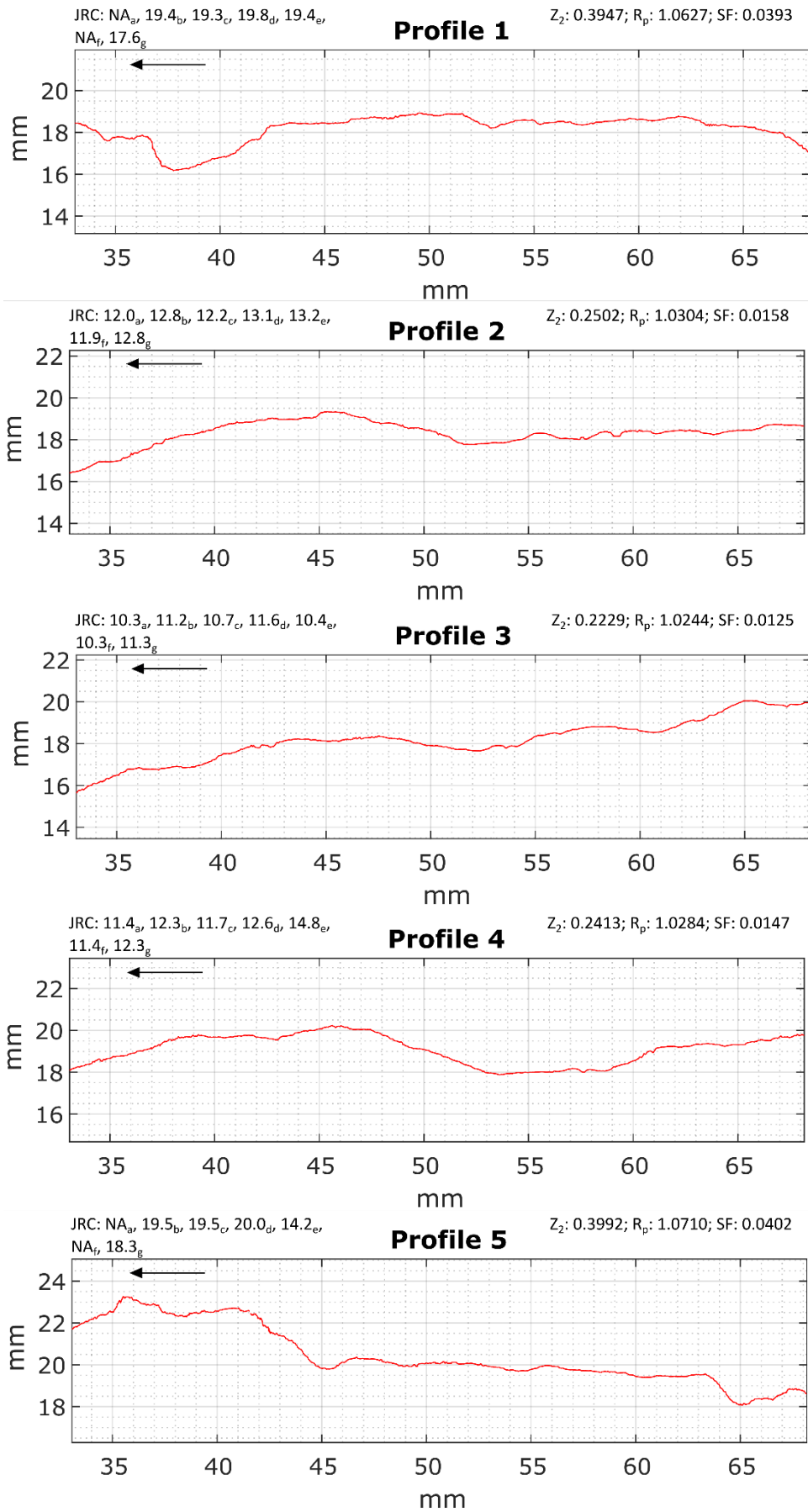


FIGURE 20: M3 PROFILES TOP

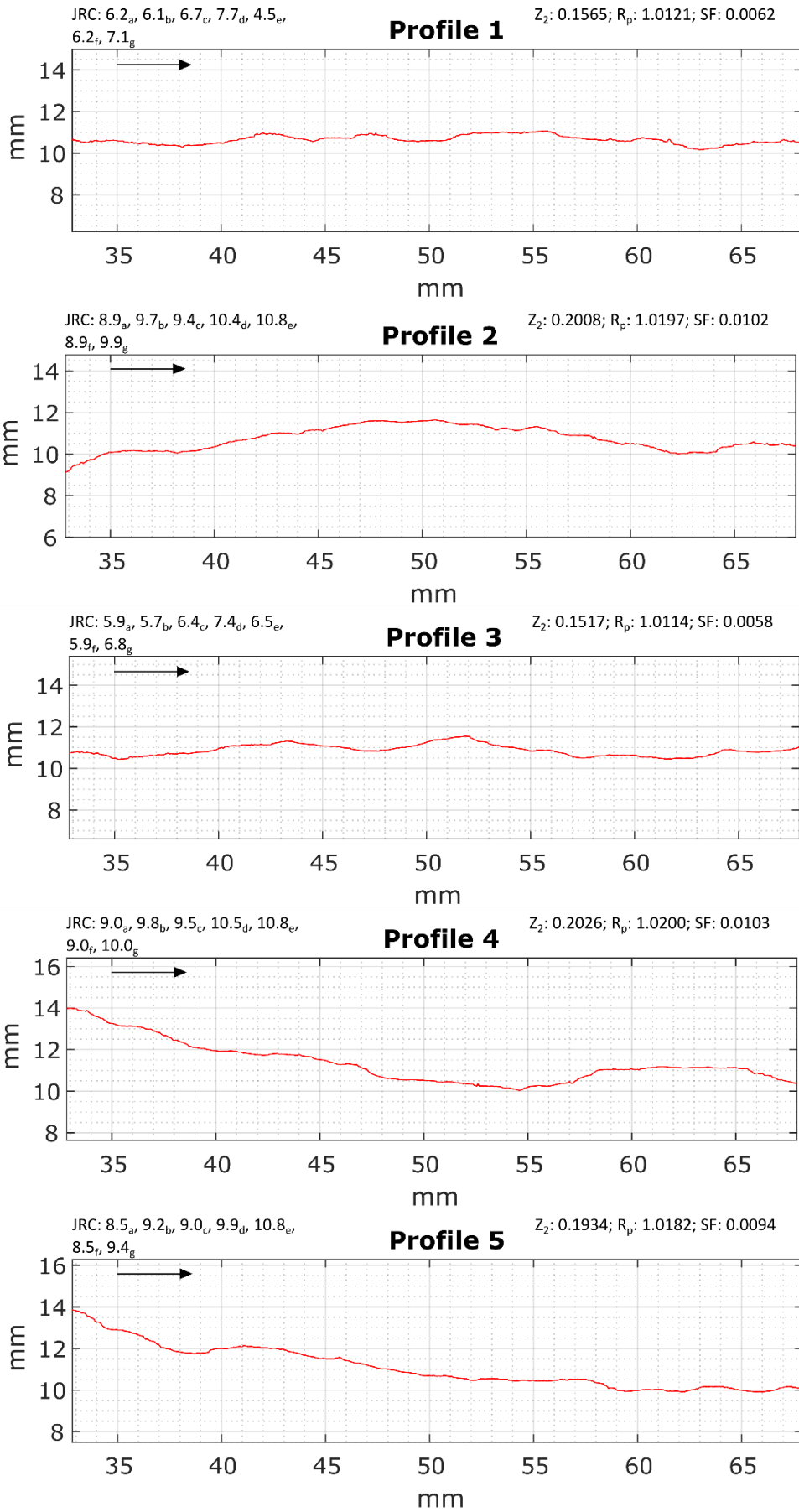


FIGURE 21: Q1 PROFILES BOTTOM

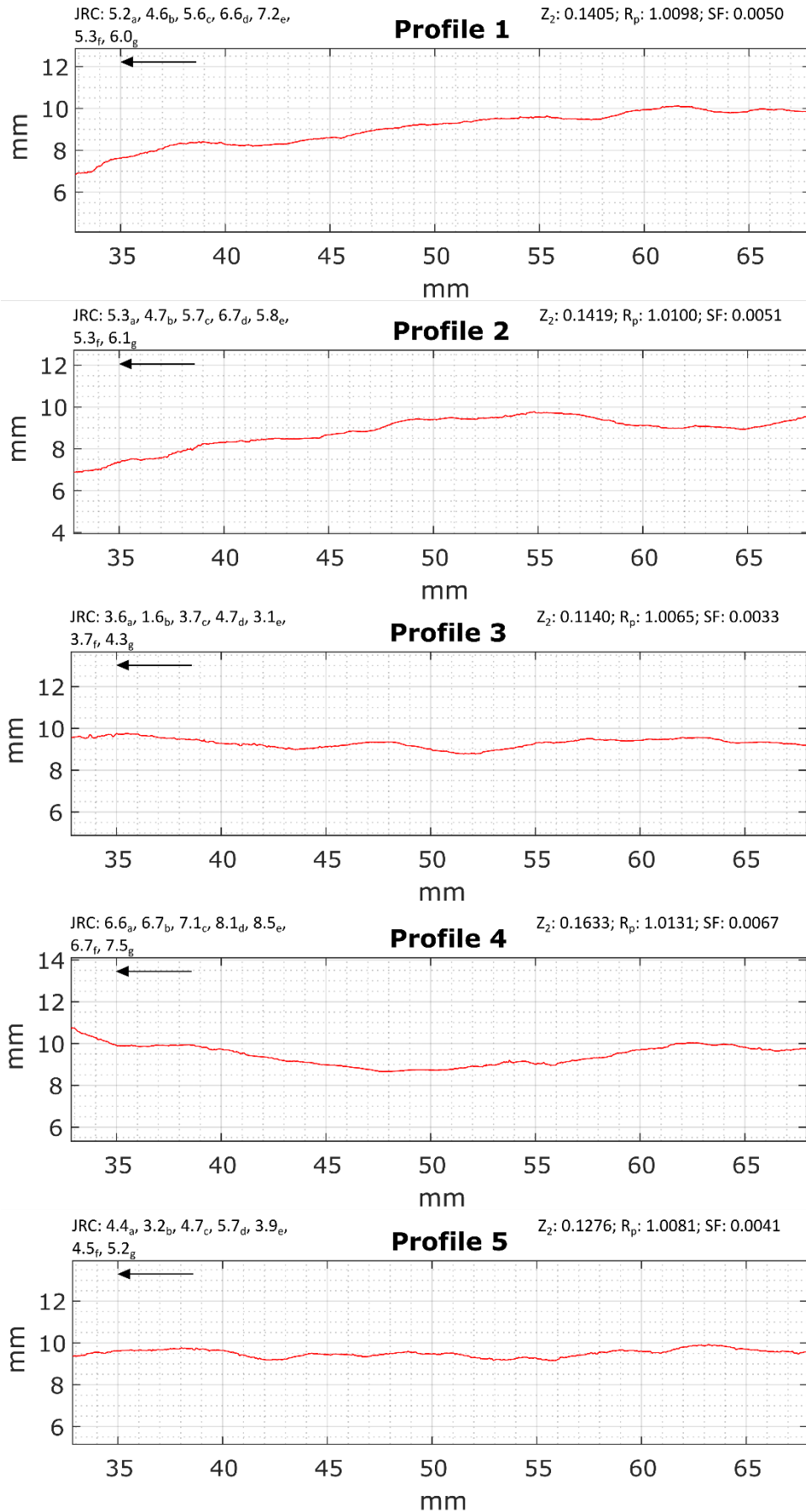


FIGURE 22: Q1 PROFILES TOP

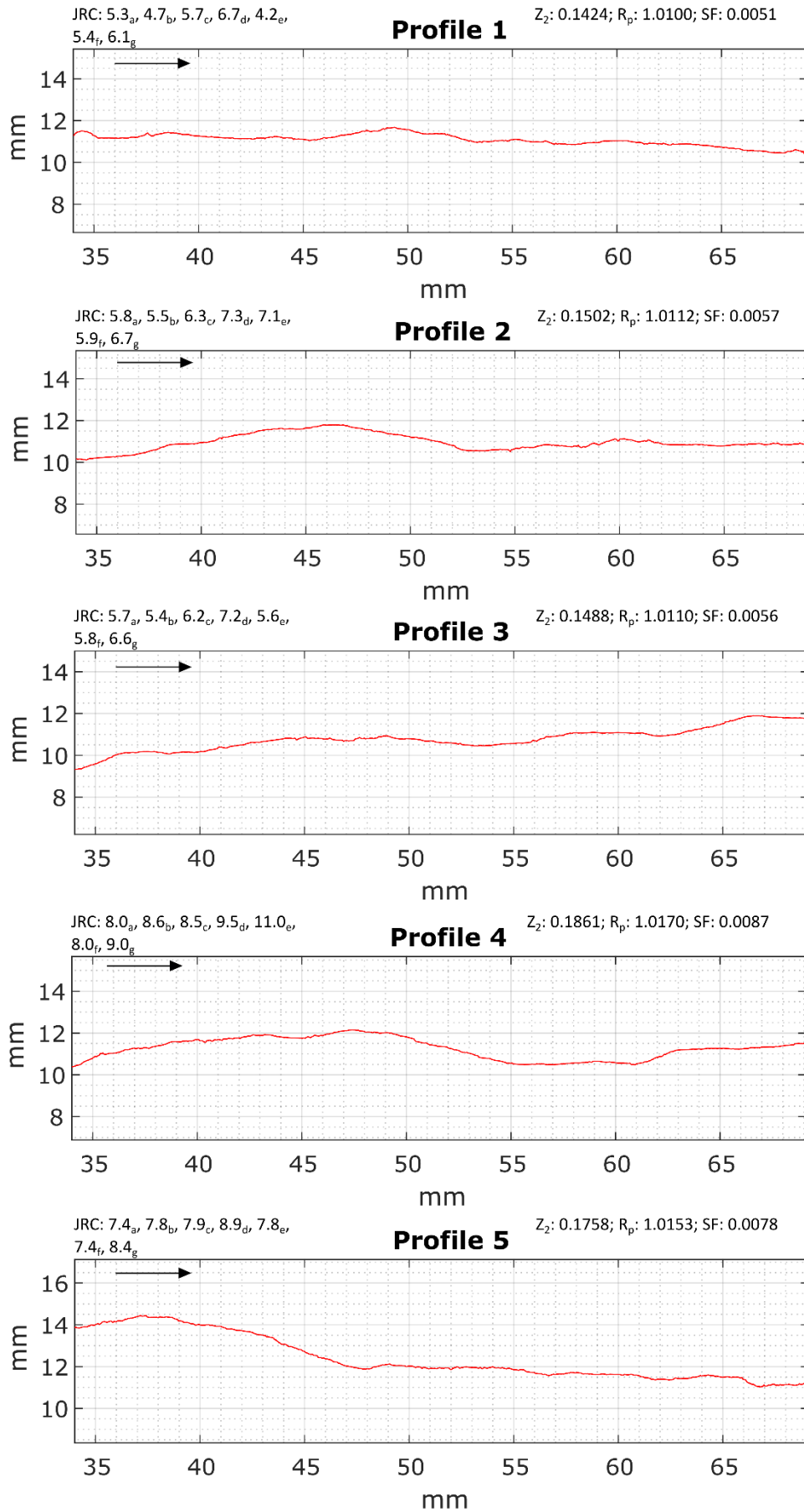


FIGURE 23: R2 PROFILES BOTTOM

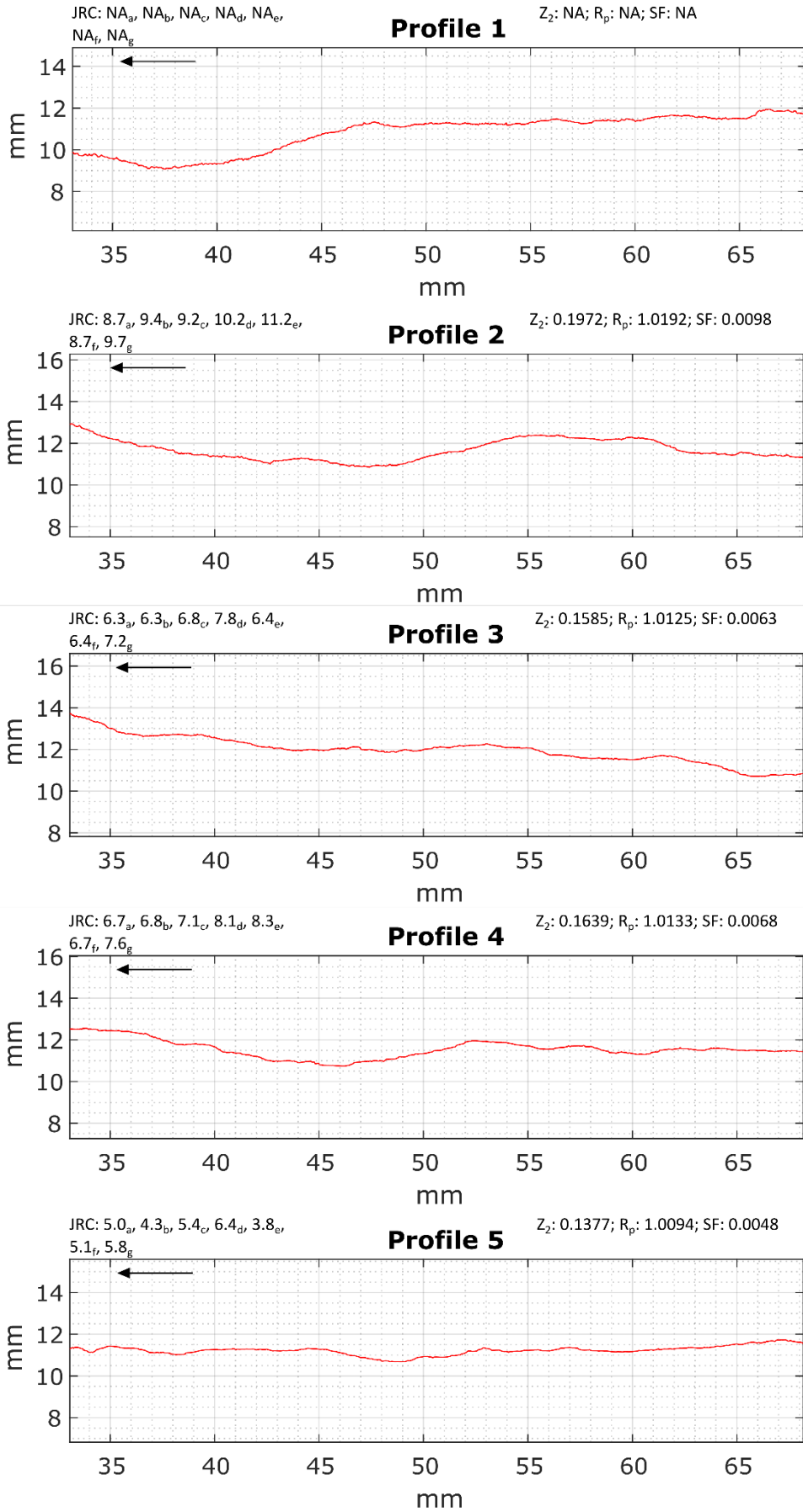


FIGURE 24: R2 PROFILES TOP

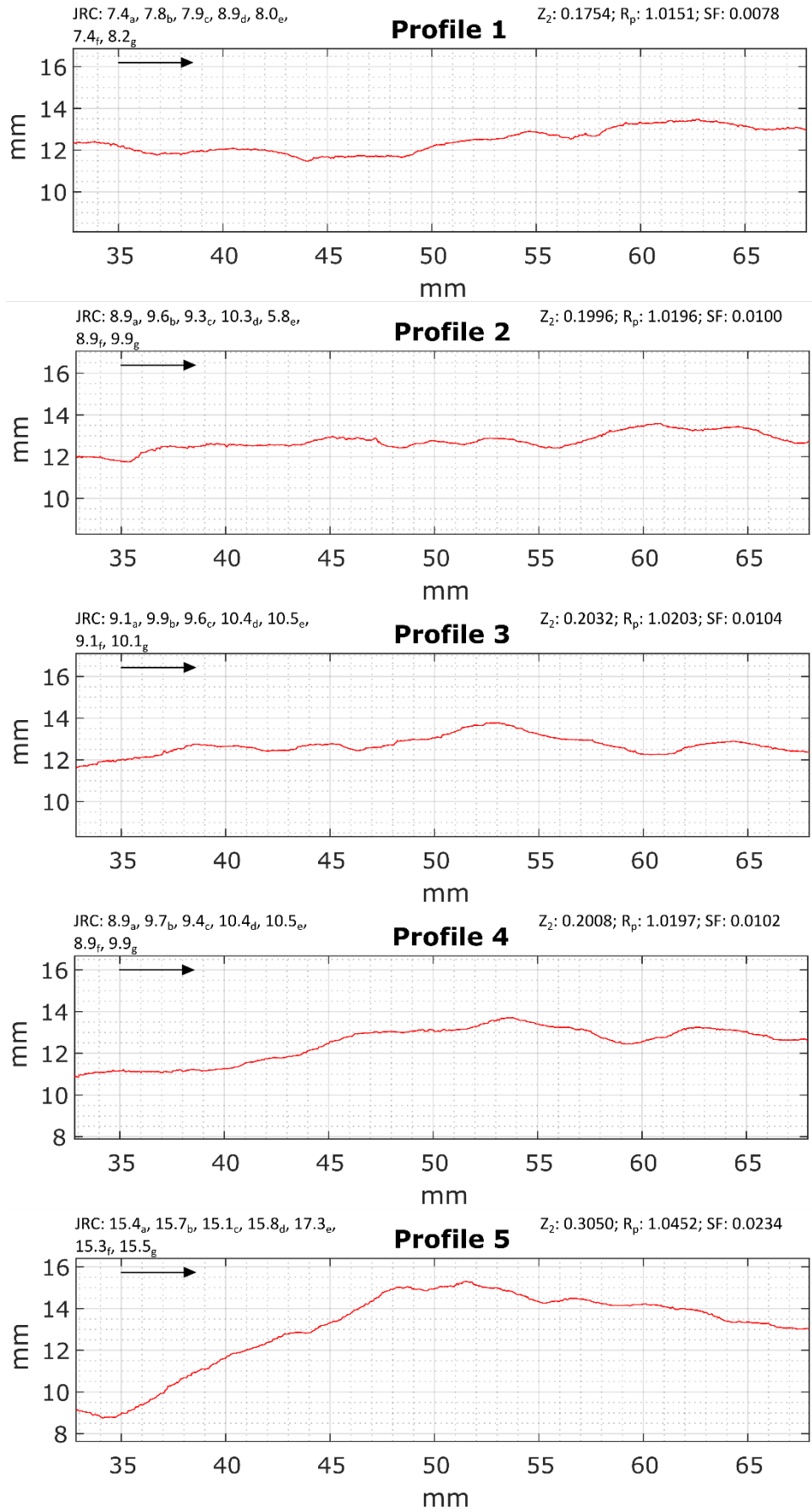


FIGURE 25: S1 PROFILES BOTTOM

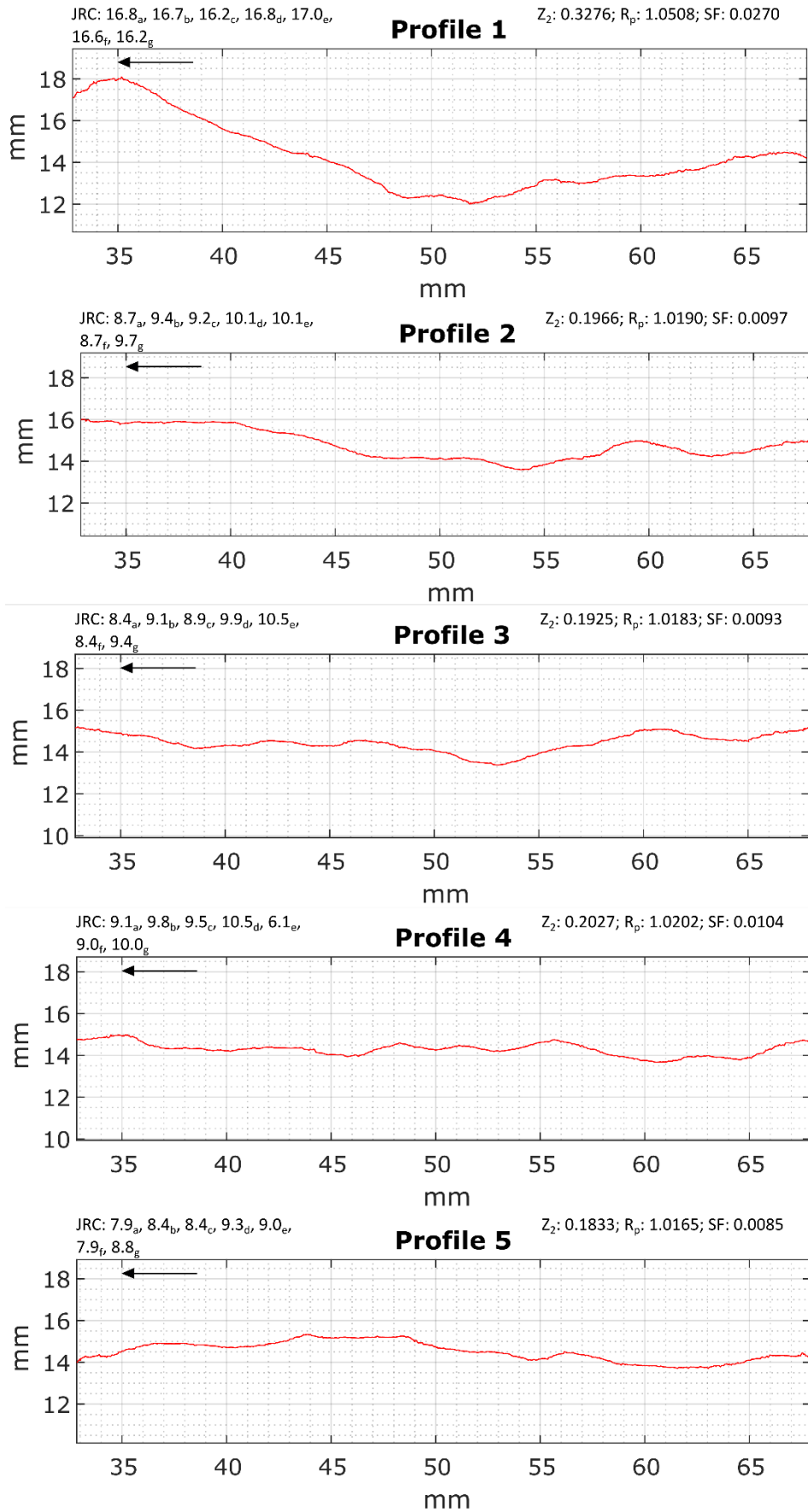


FIGURE 26: S1 PROFILES TOP

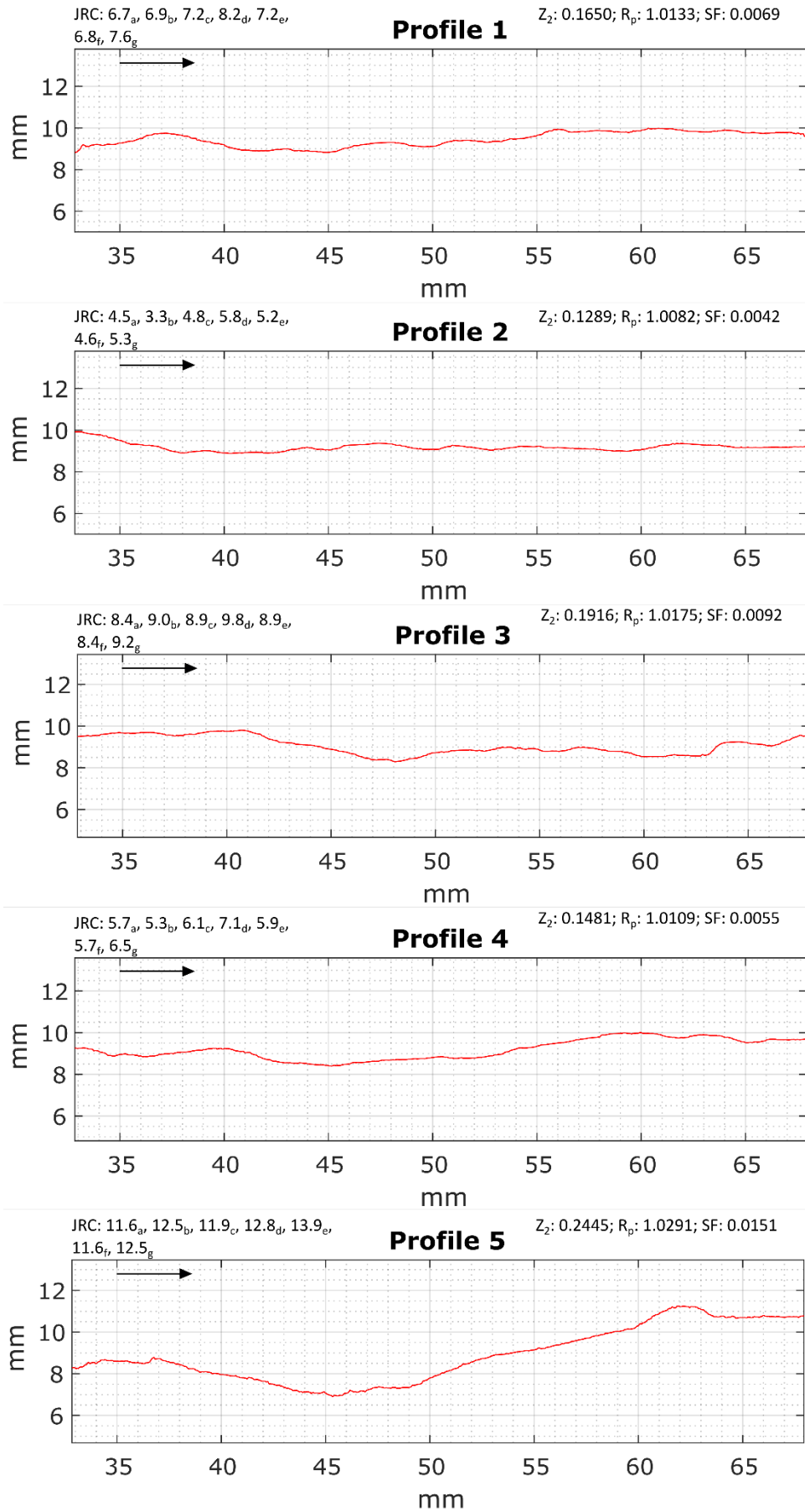


FIGURE 27: T2 PROFILES BOTTOM

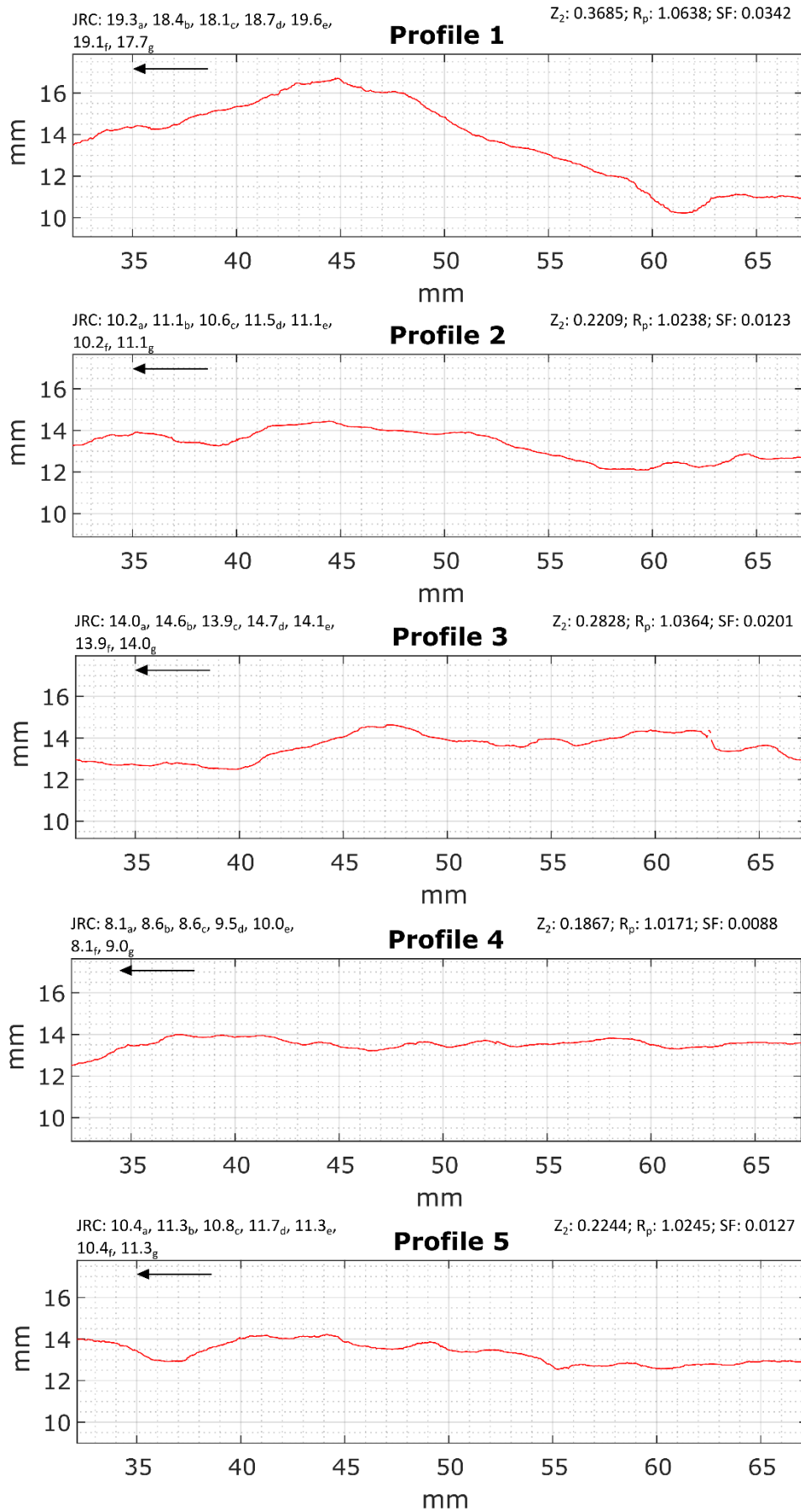


FIGURE 28: T2 PROFILES TOP

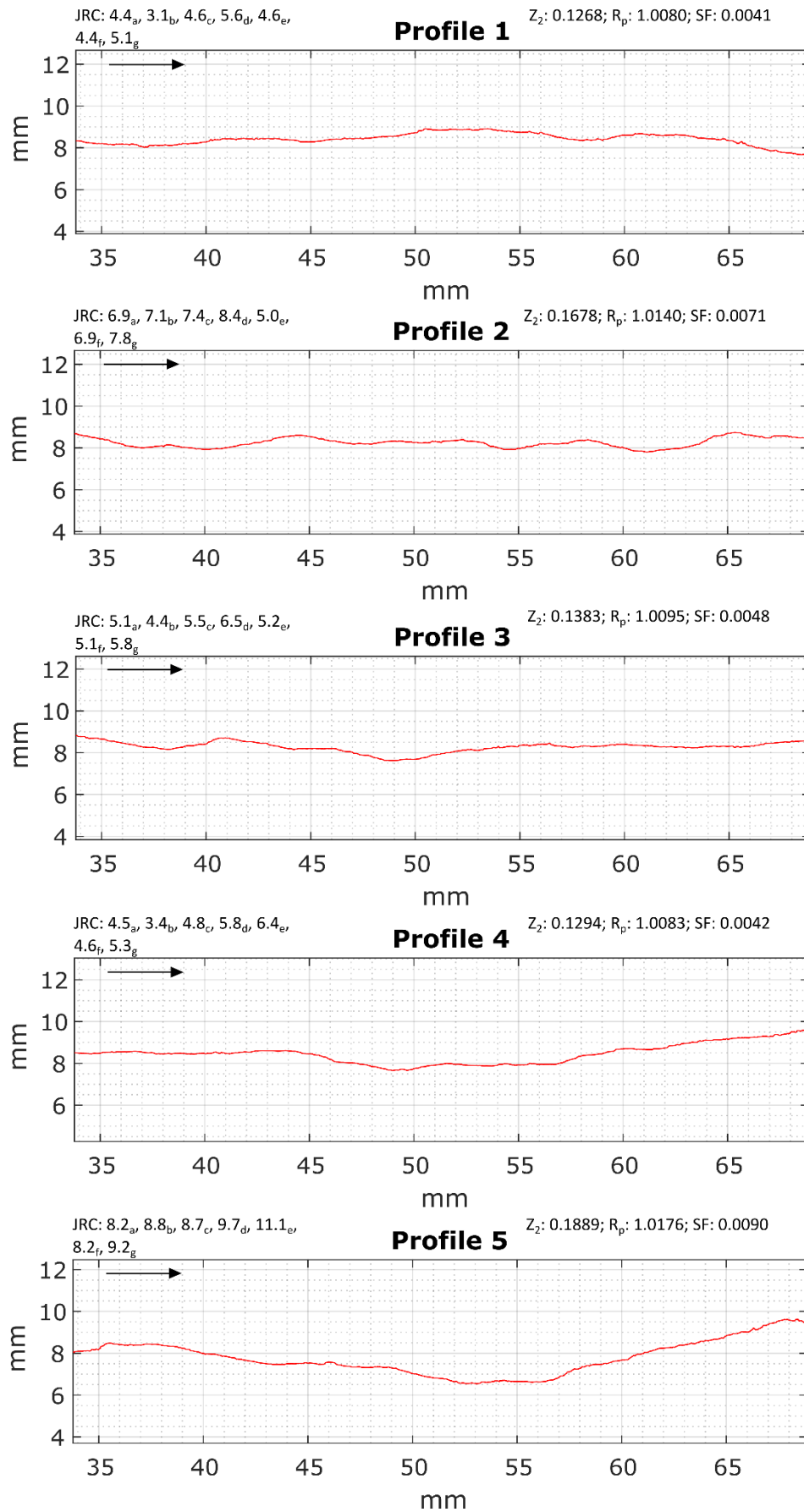


FIGURE 29: U2 PROFILES BOTTOM

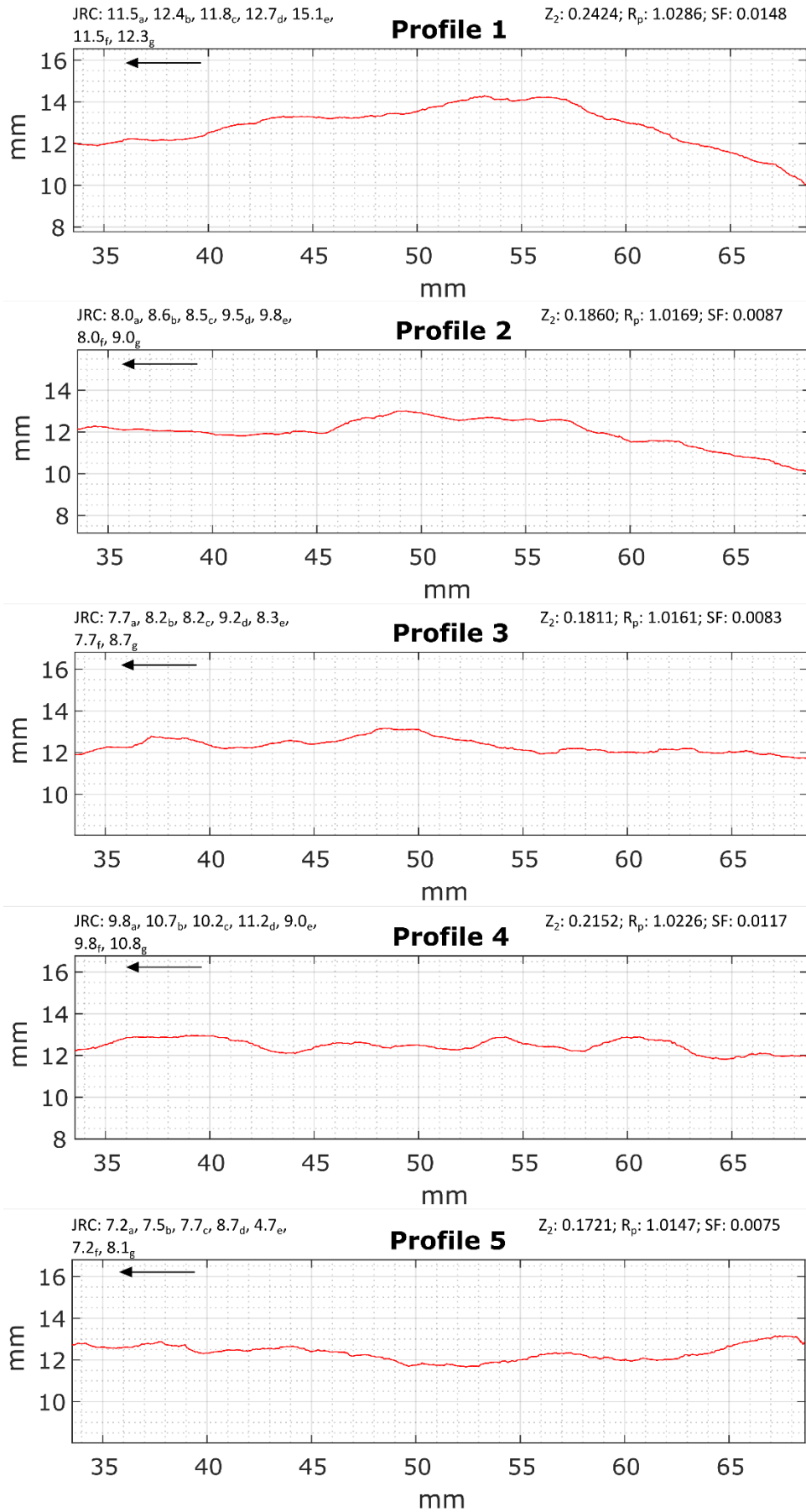


FIGURE 30: U2 PROFILES TOP

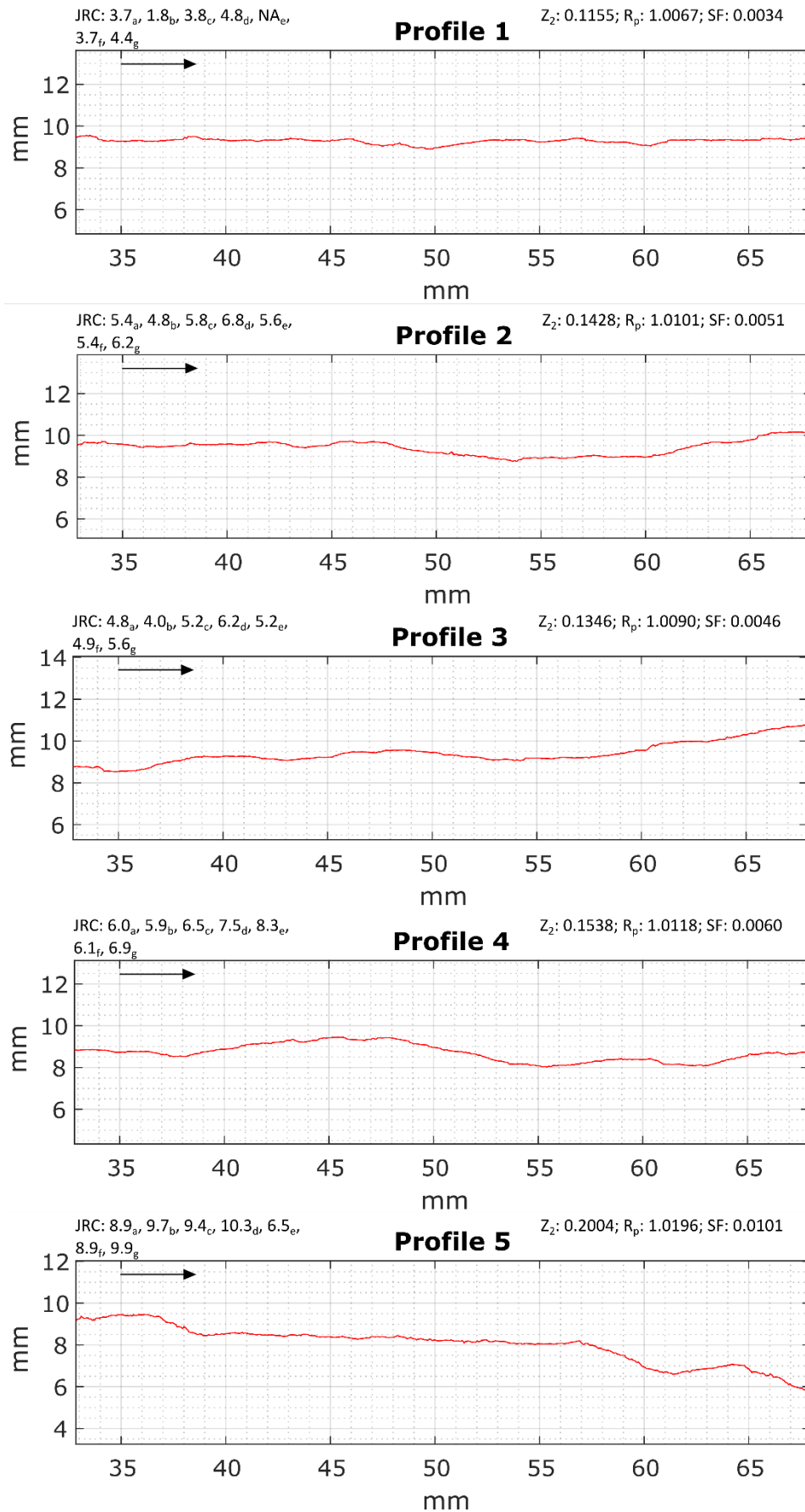


FIGURE 31: V1 PROFILES BOTTOM

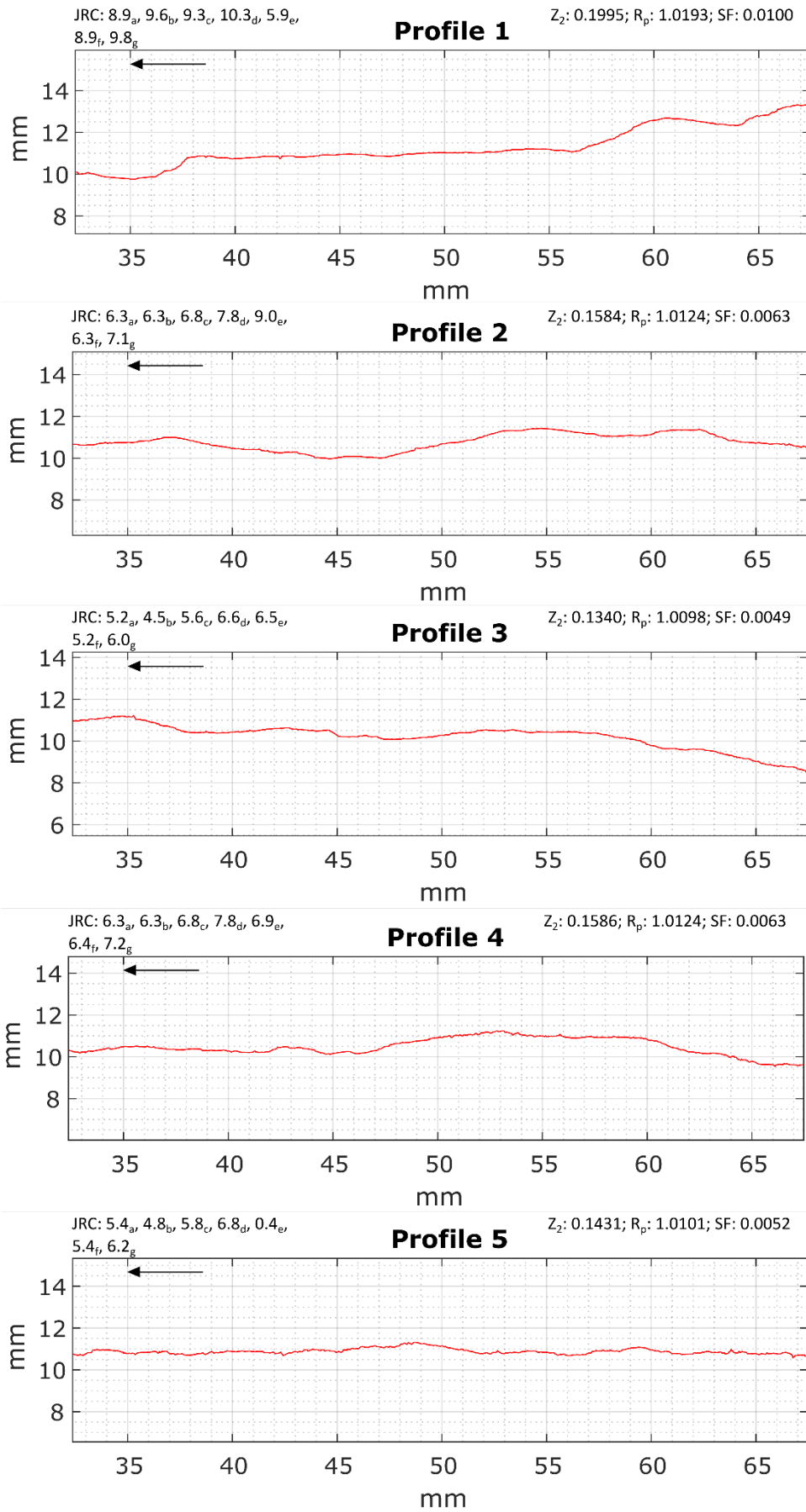


FIGURE 32: V1 PROFILES TOP

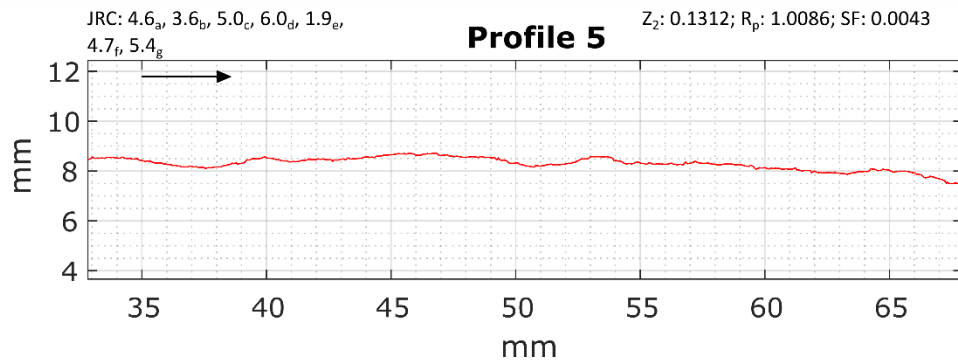
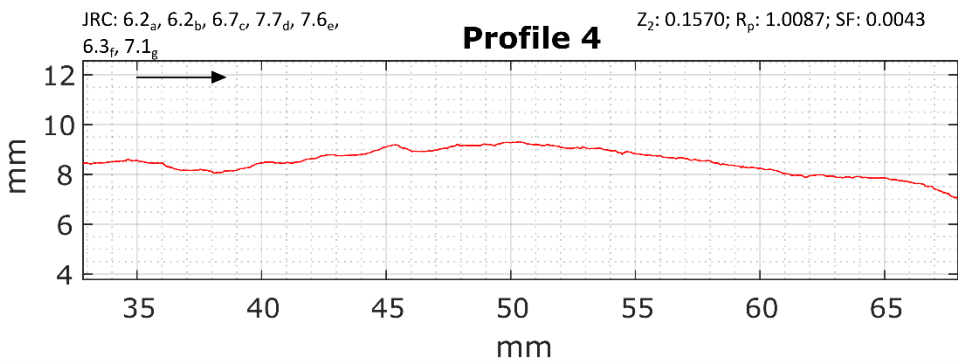
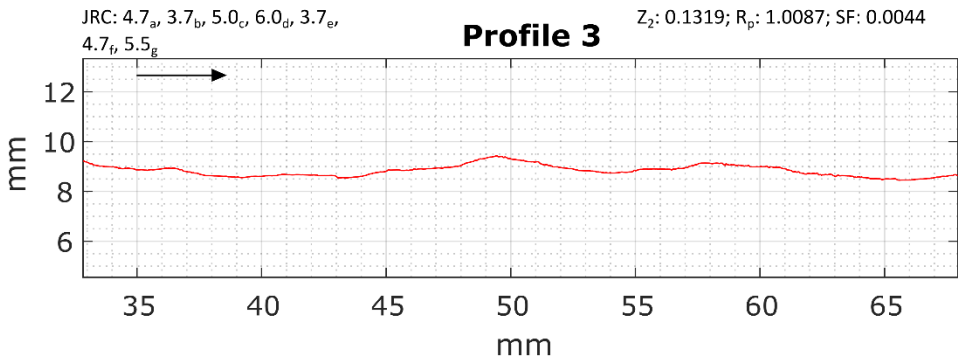
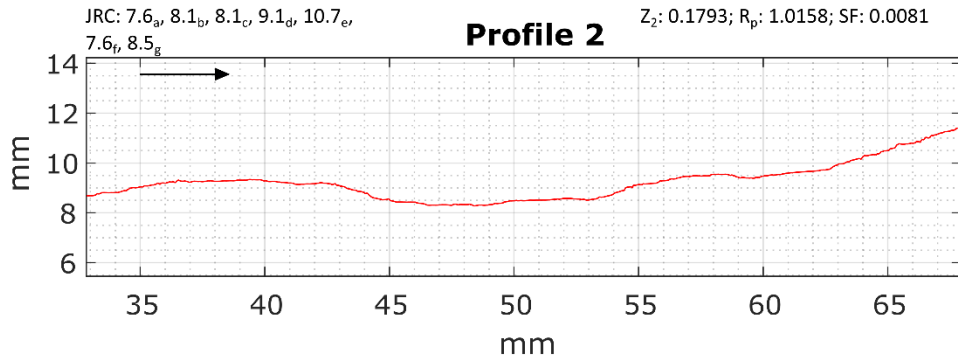
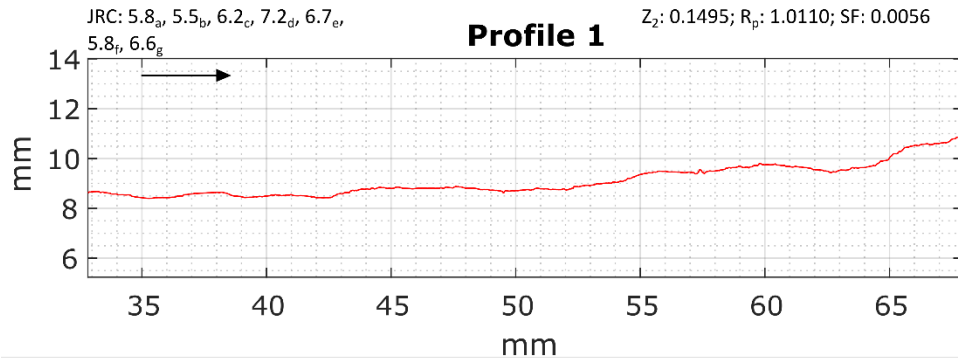


FIGURE 33: W1 PROFILES BOTTOM

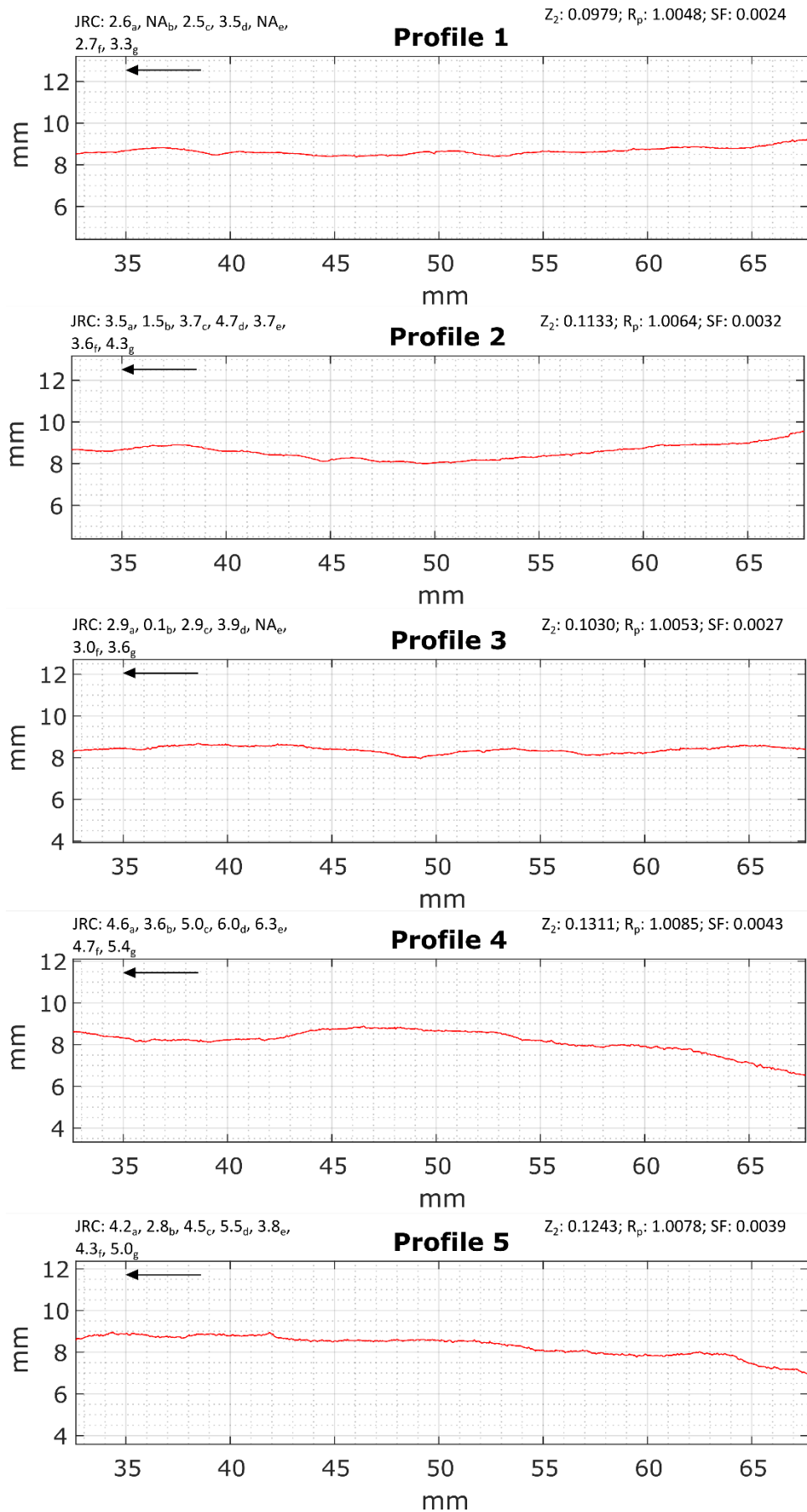


FIGURE 34: W1 PROFILES TOP

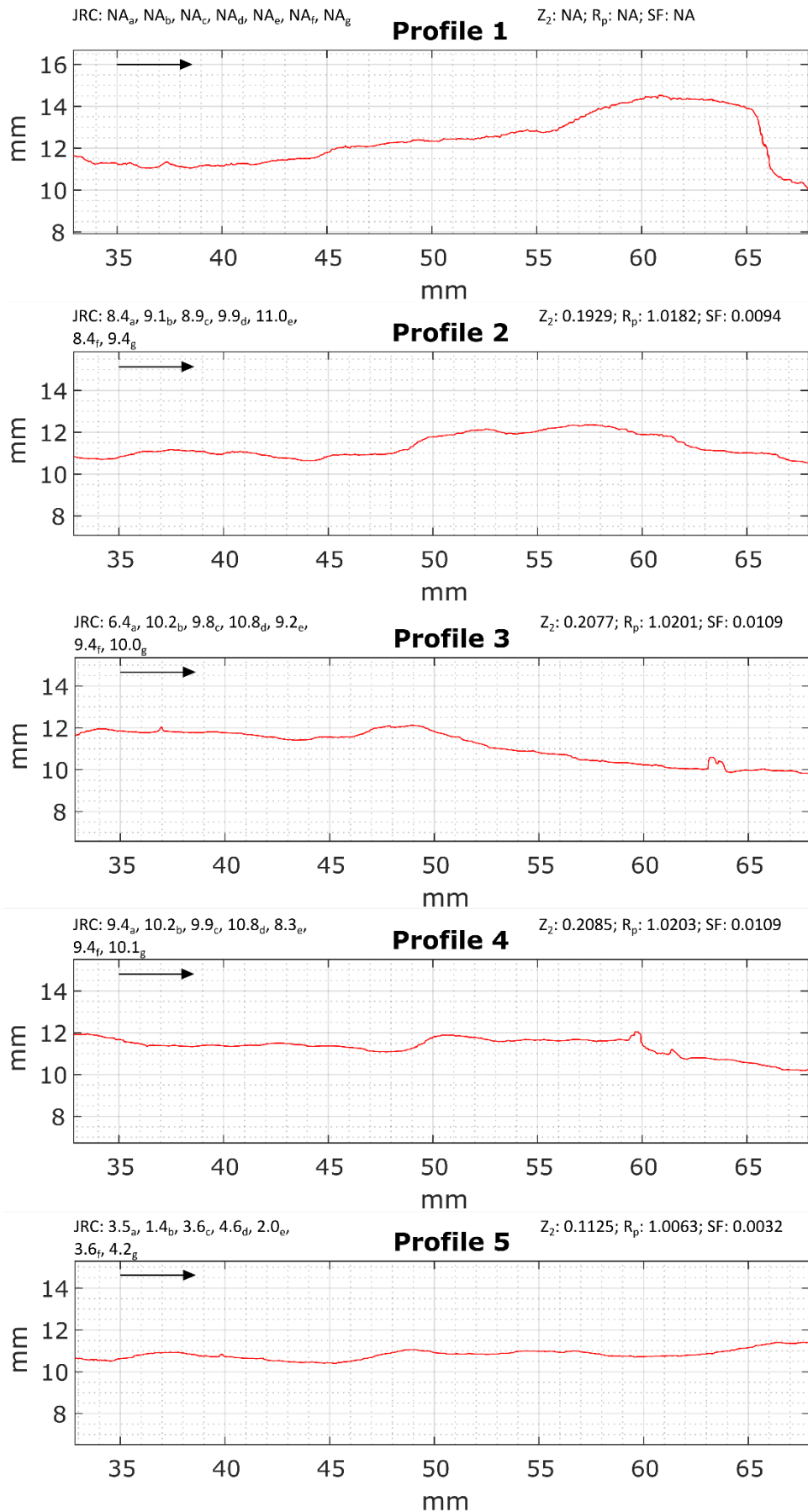


FIGURE 35: X1 PROFILES BOTTOM

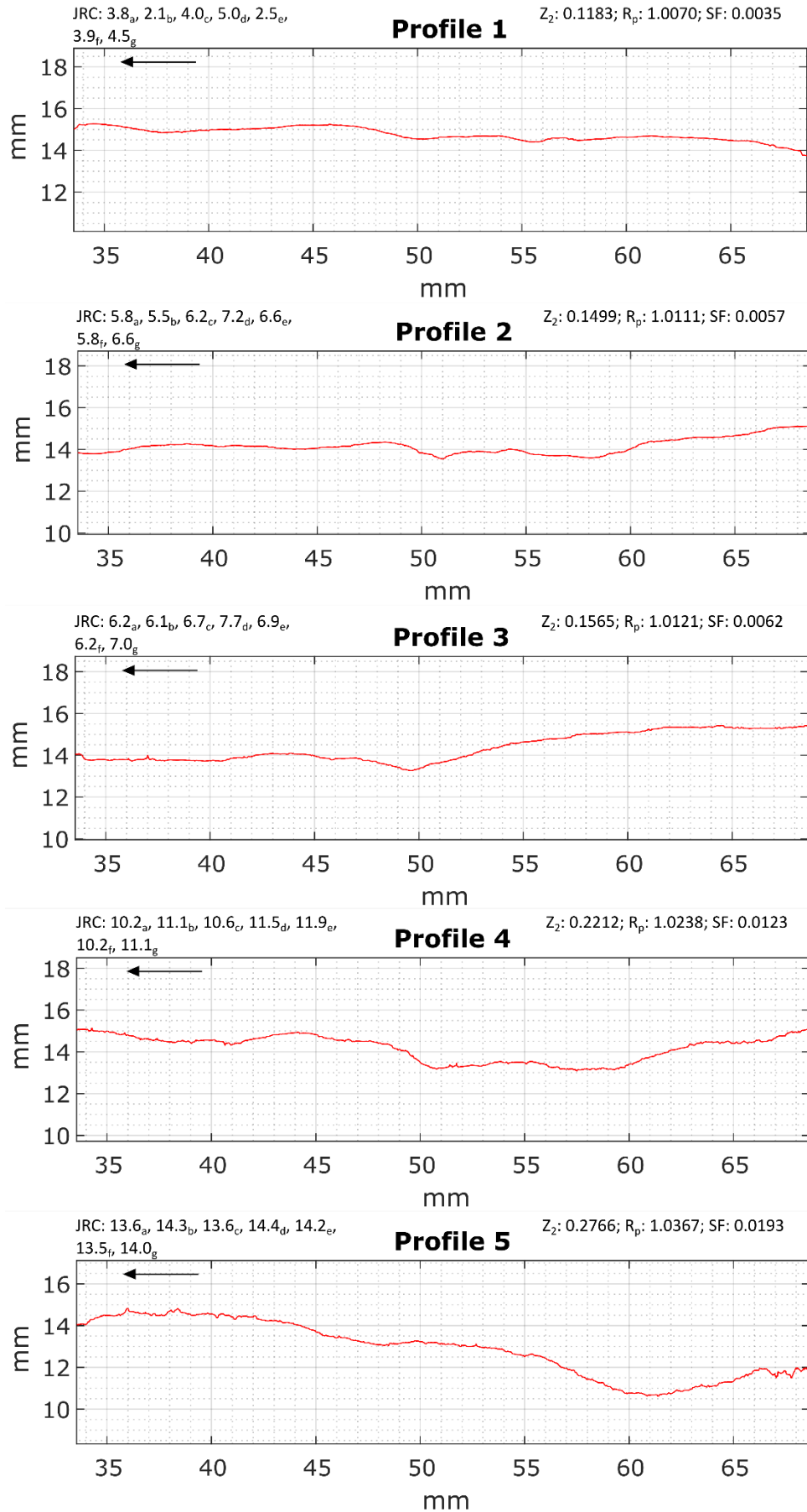


FIGURE 36: X1 PROFILES TOP

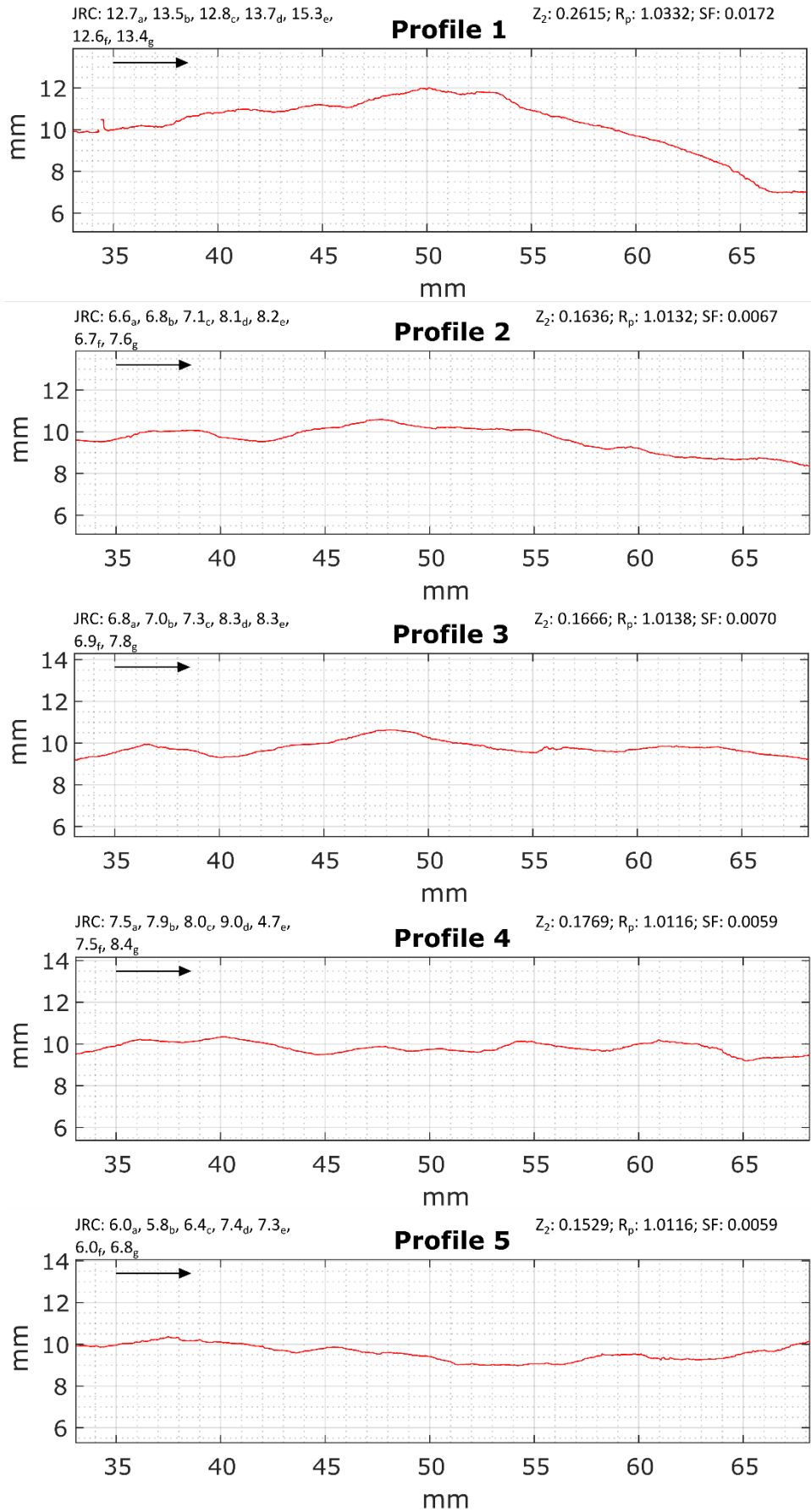


FIGURE 37: Y1 PROFILES BOTTOM

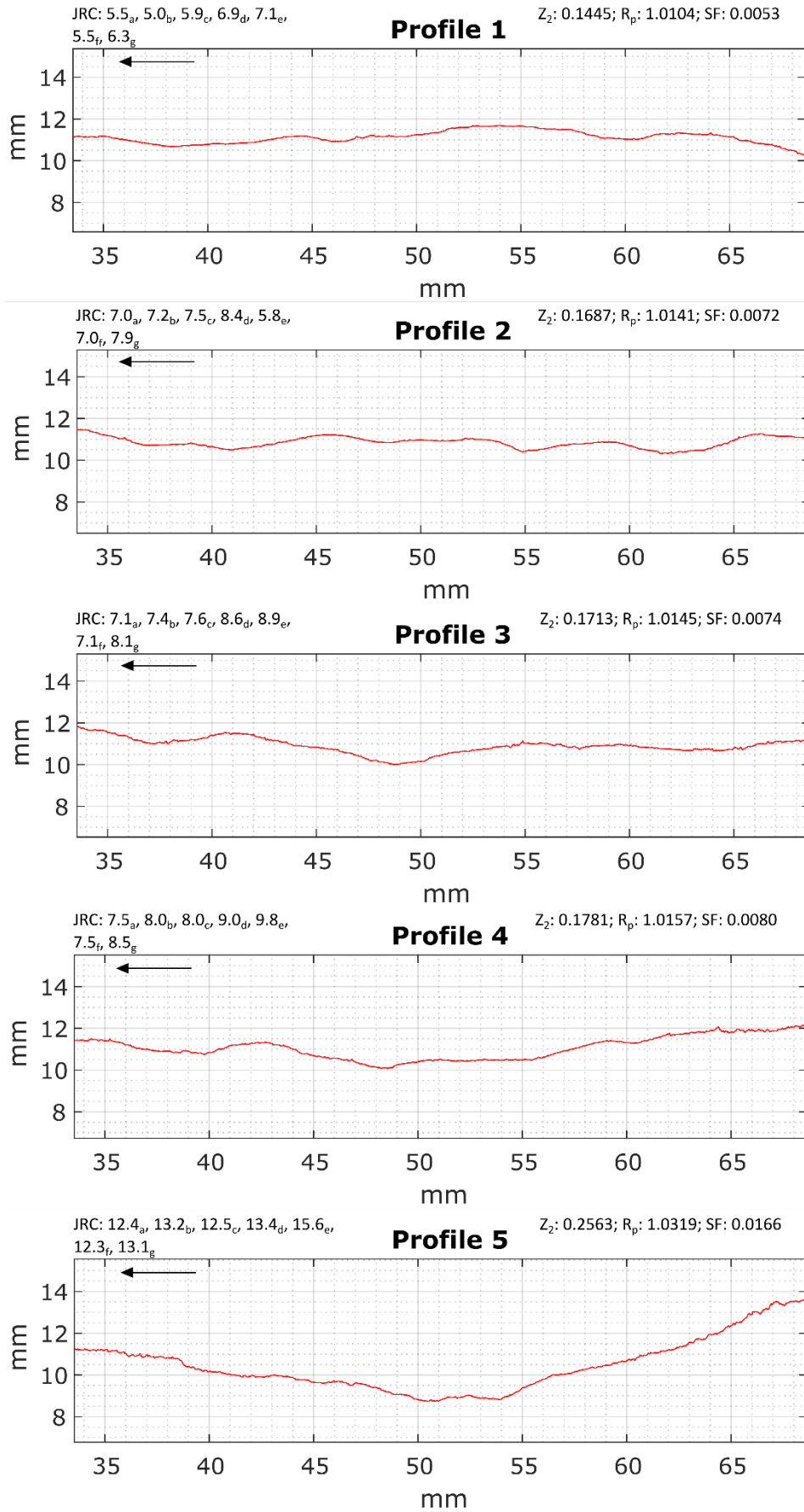


FIGURE 38: Y1 PROFILES TOP

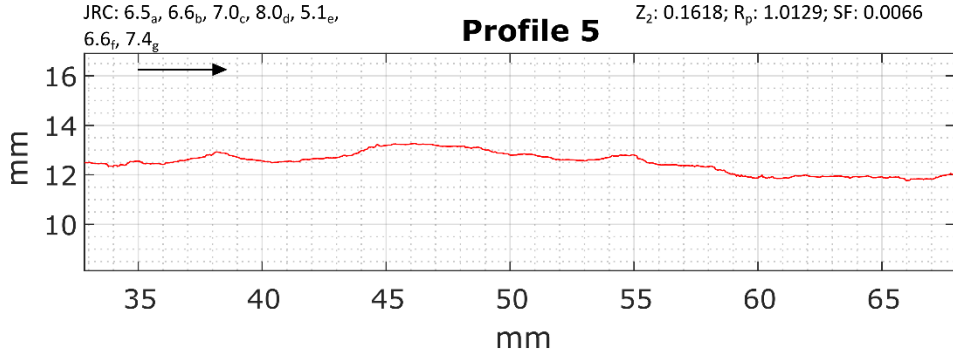
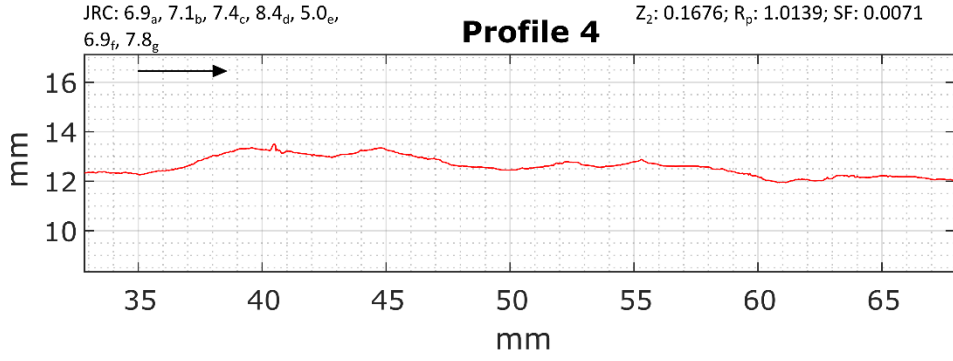
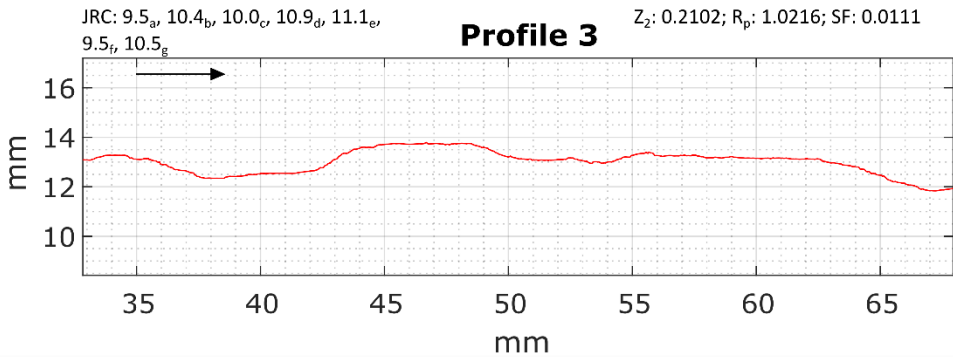
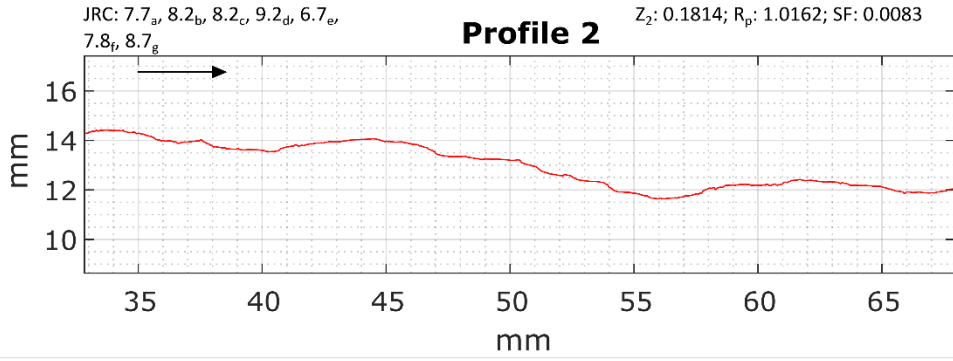
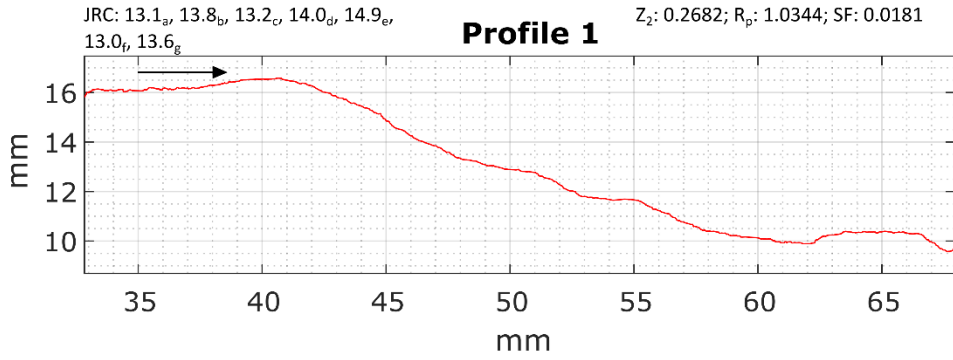


FIGURE 39: Z1 PROFILES BOTTOM

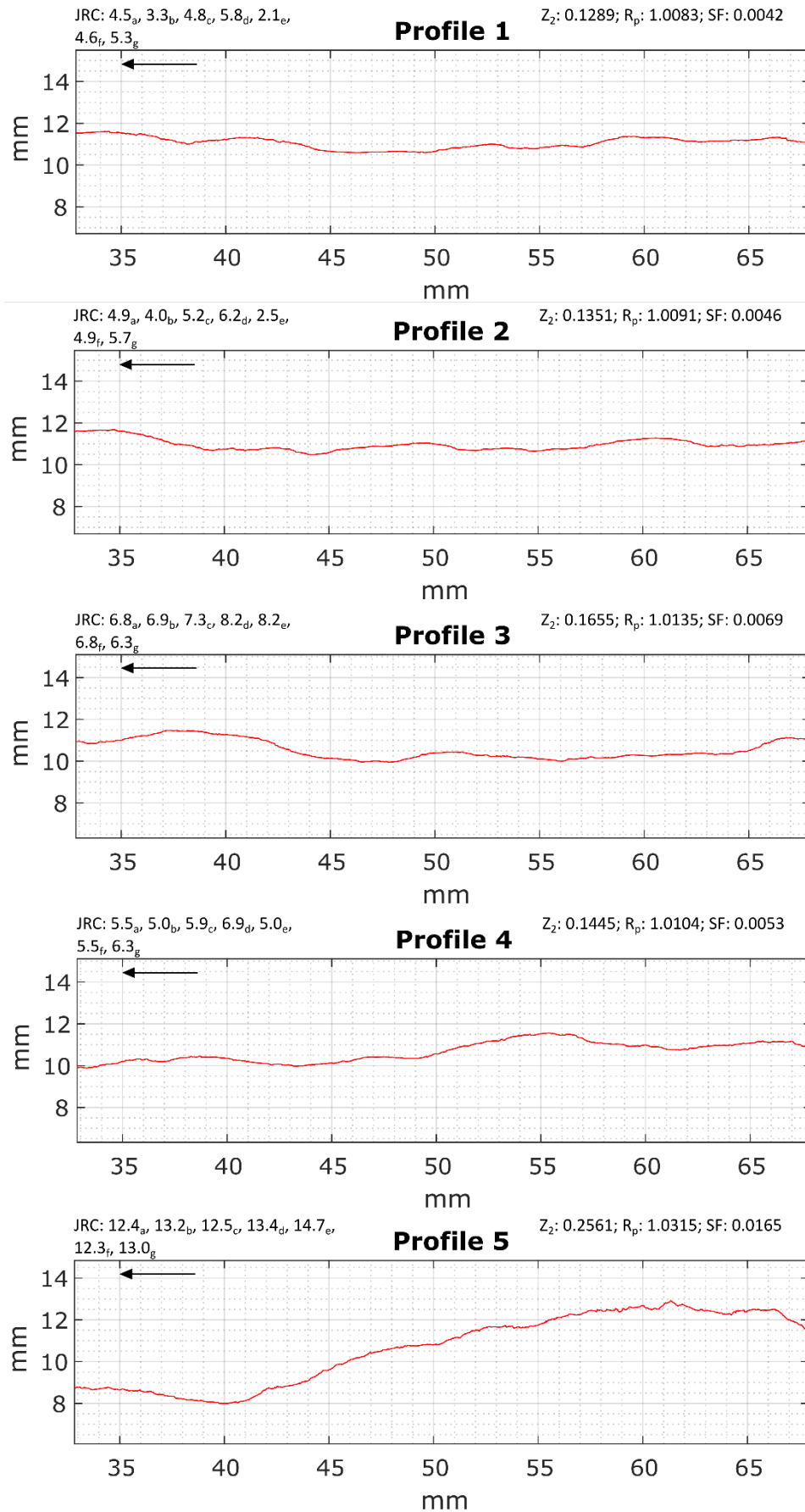


FIGURE 40: Z1 PROFILES TOP

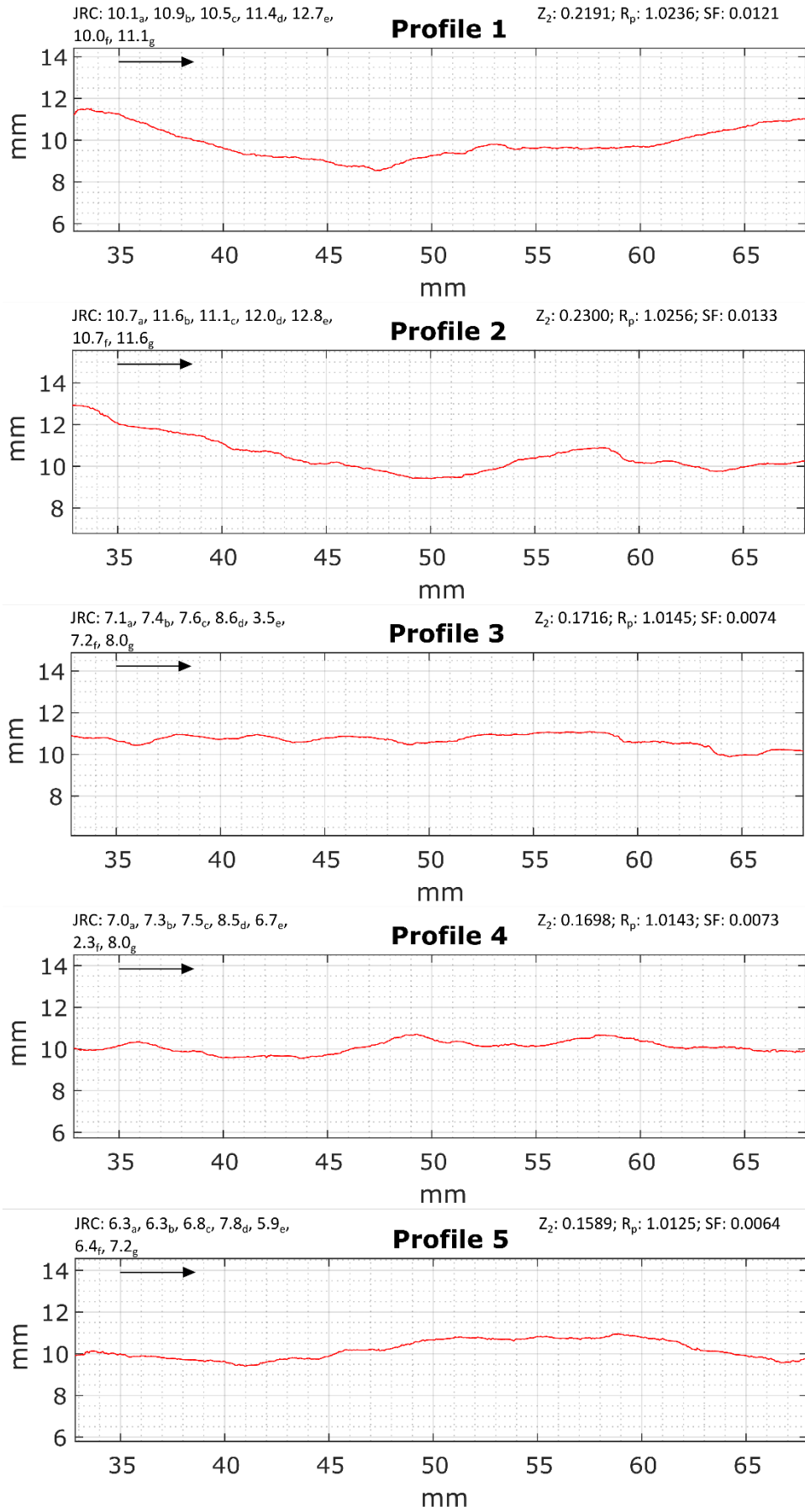


FIGURE 41: ZZ1 PROFILES BOTTOM

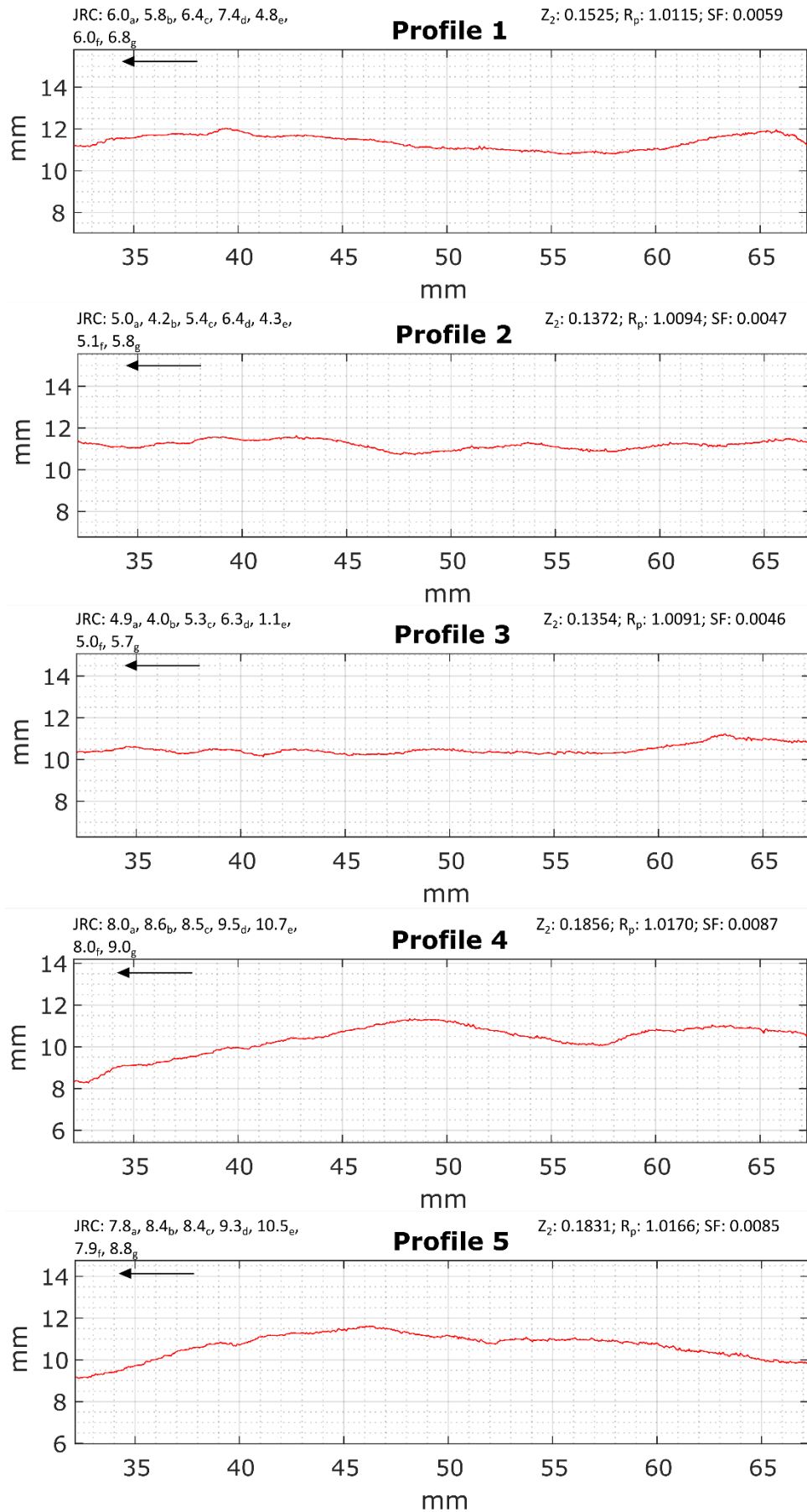


FIGURE 42: ZZ1 PROFILES TOP

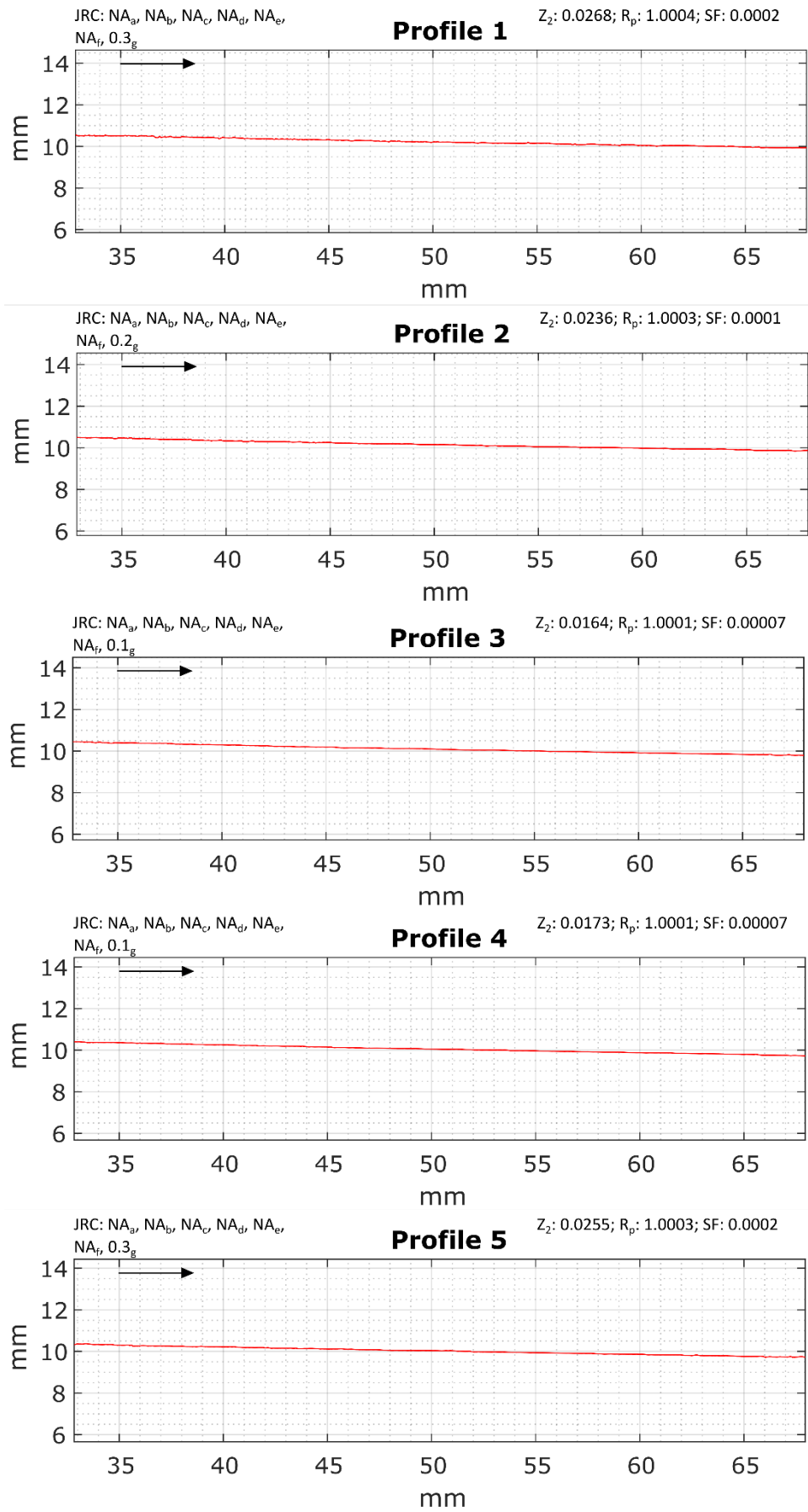


FIGURE 43: SMOOTH PLASTER PROFILES BOTTOM

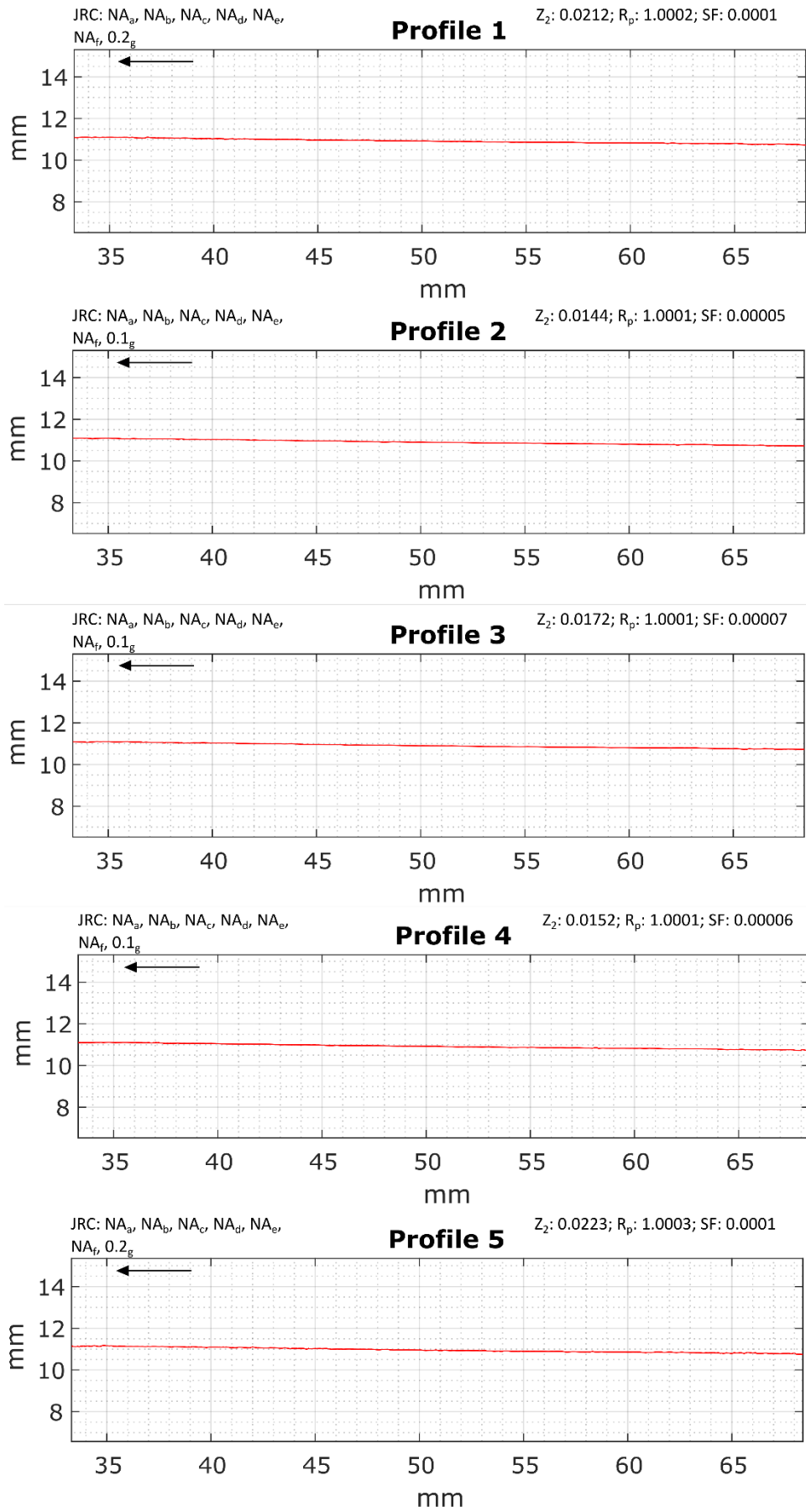


FIGURE 44: SMOOTH PLASTER PROFILES TOP

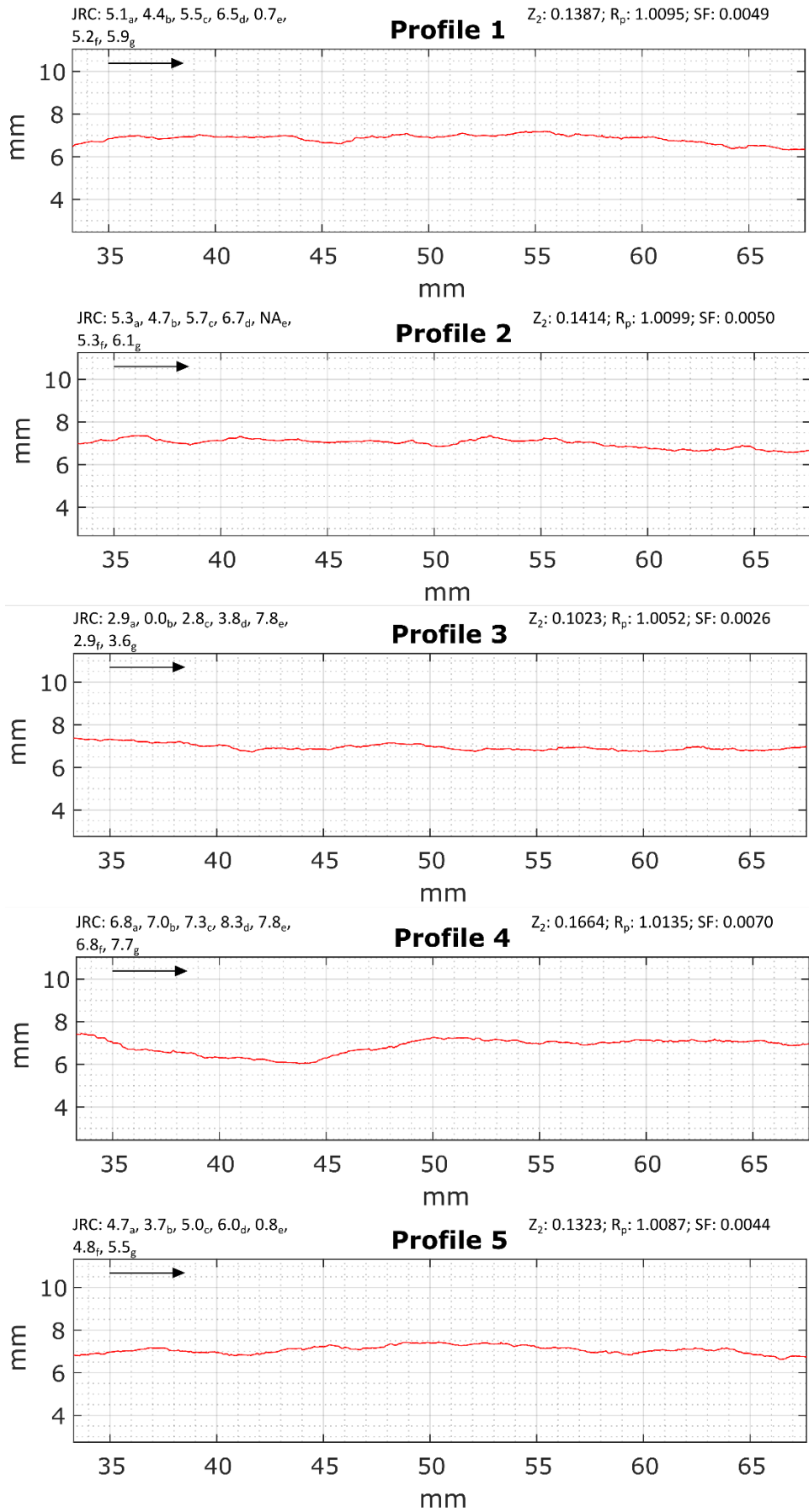


FIGURE 45: SA1 PROFILES BOTTOM

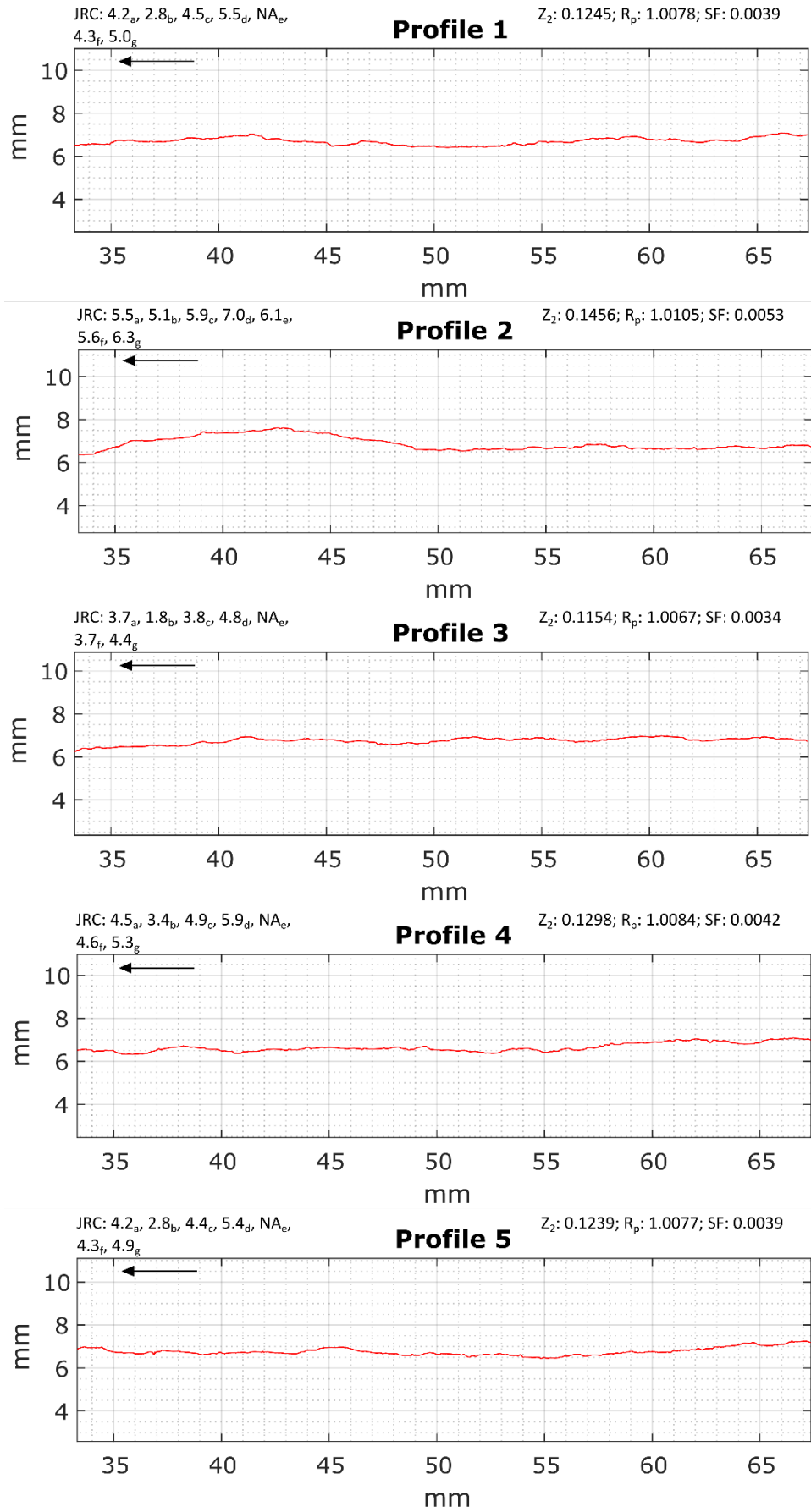


FIGURE 46: SA1 PROFILES TOP

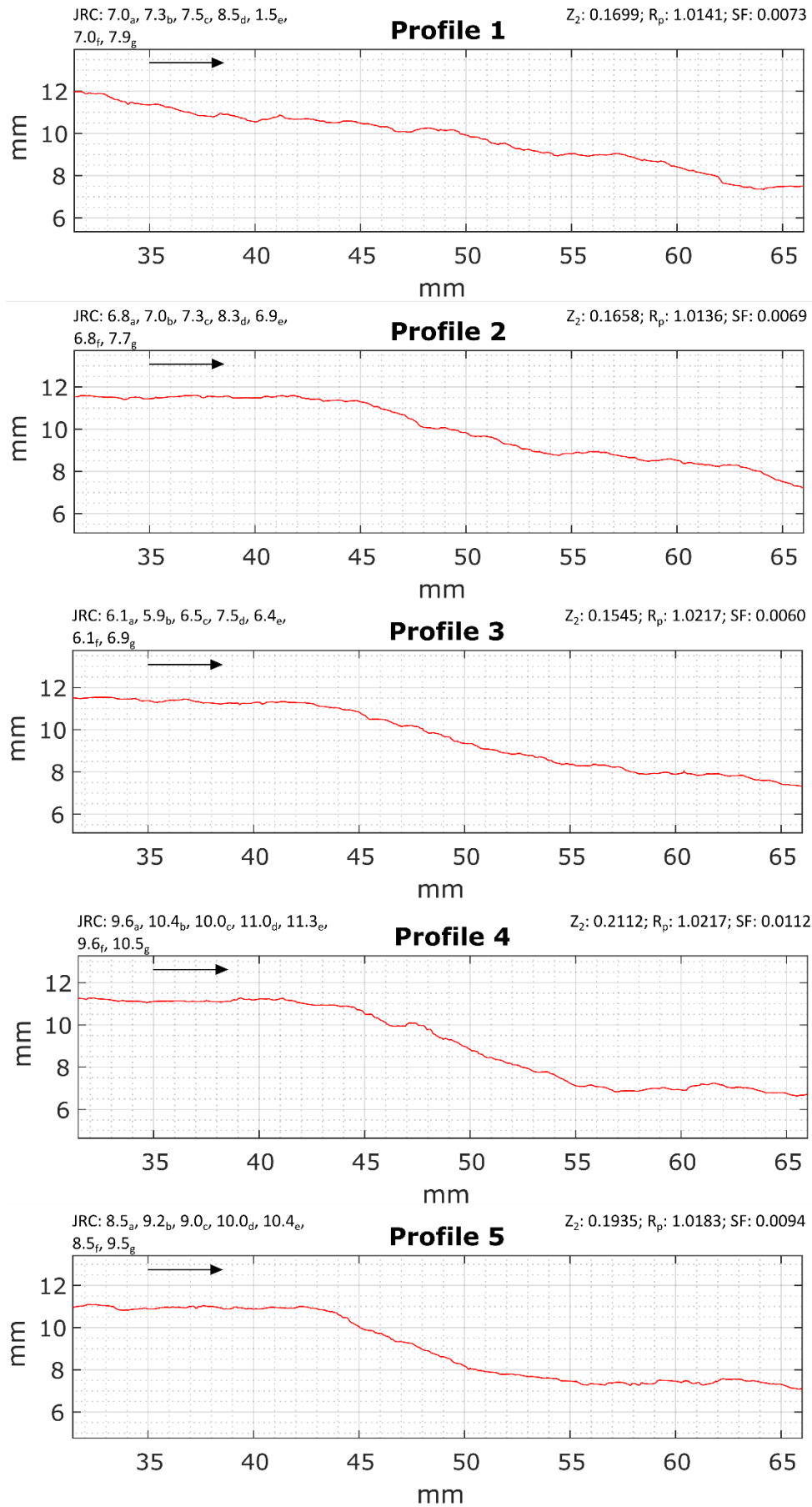


FIGURE 47: SA2 PROFILES BOTTOM

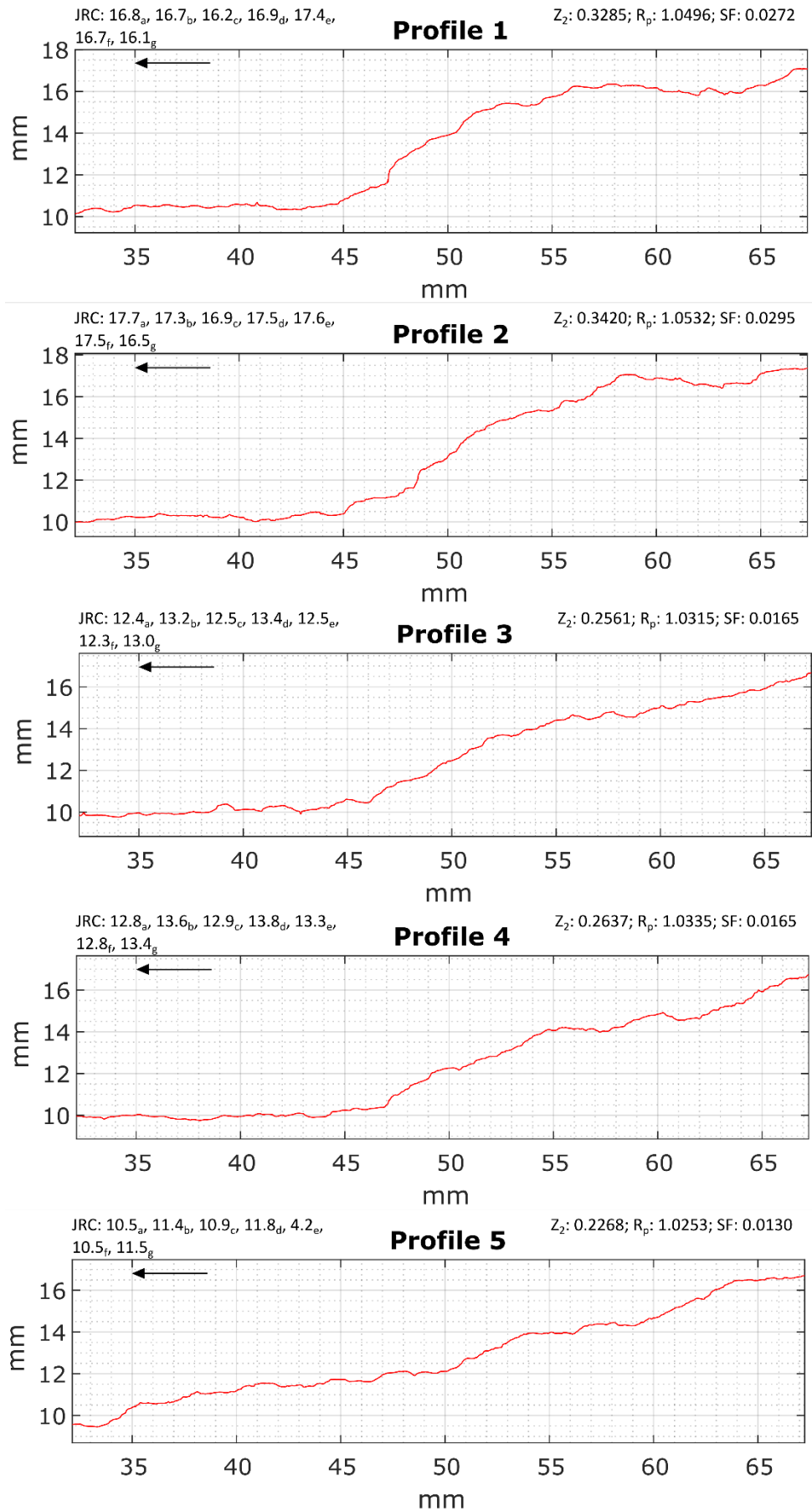


FIGURE 48: SA 2 PROFILES TOP

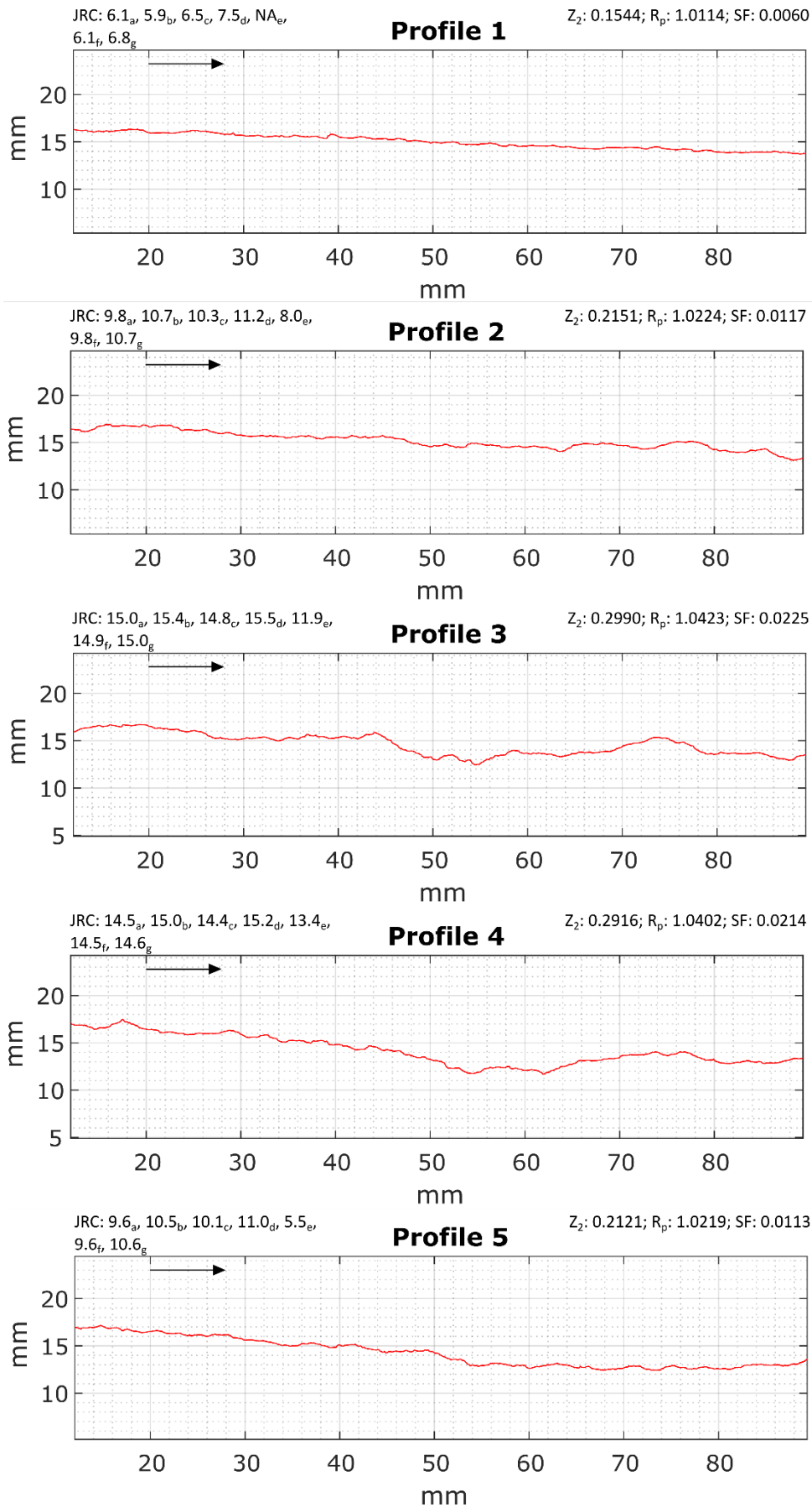


FIGURE 49: SA3 PROFILES BOTTOM

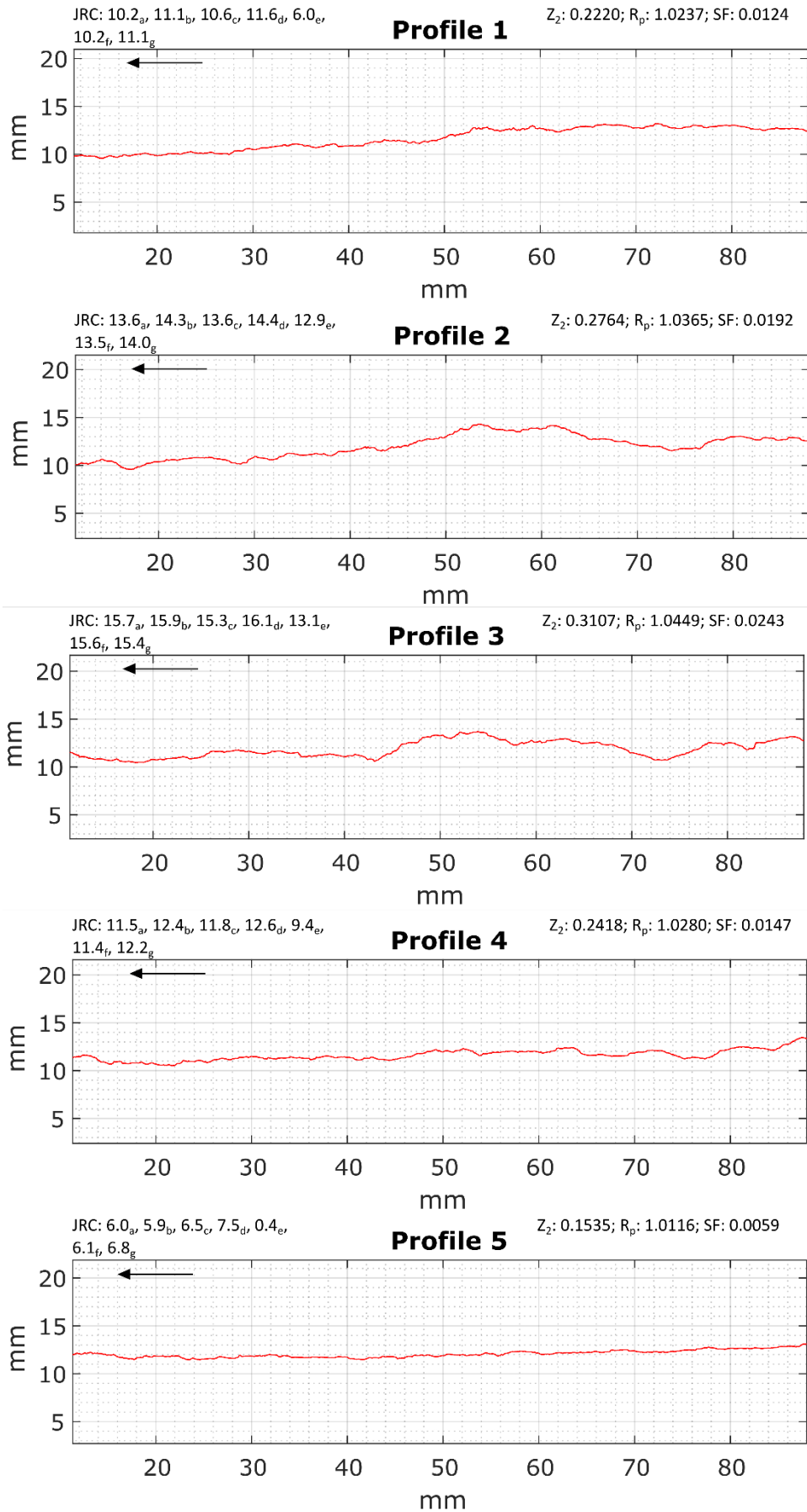


FIGURE 50: SA3 PROFILES TOP

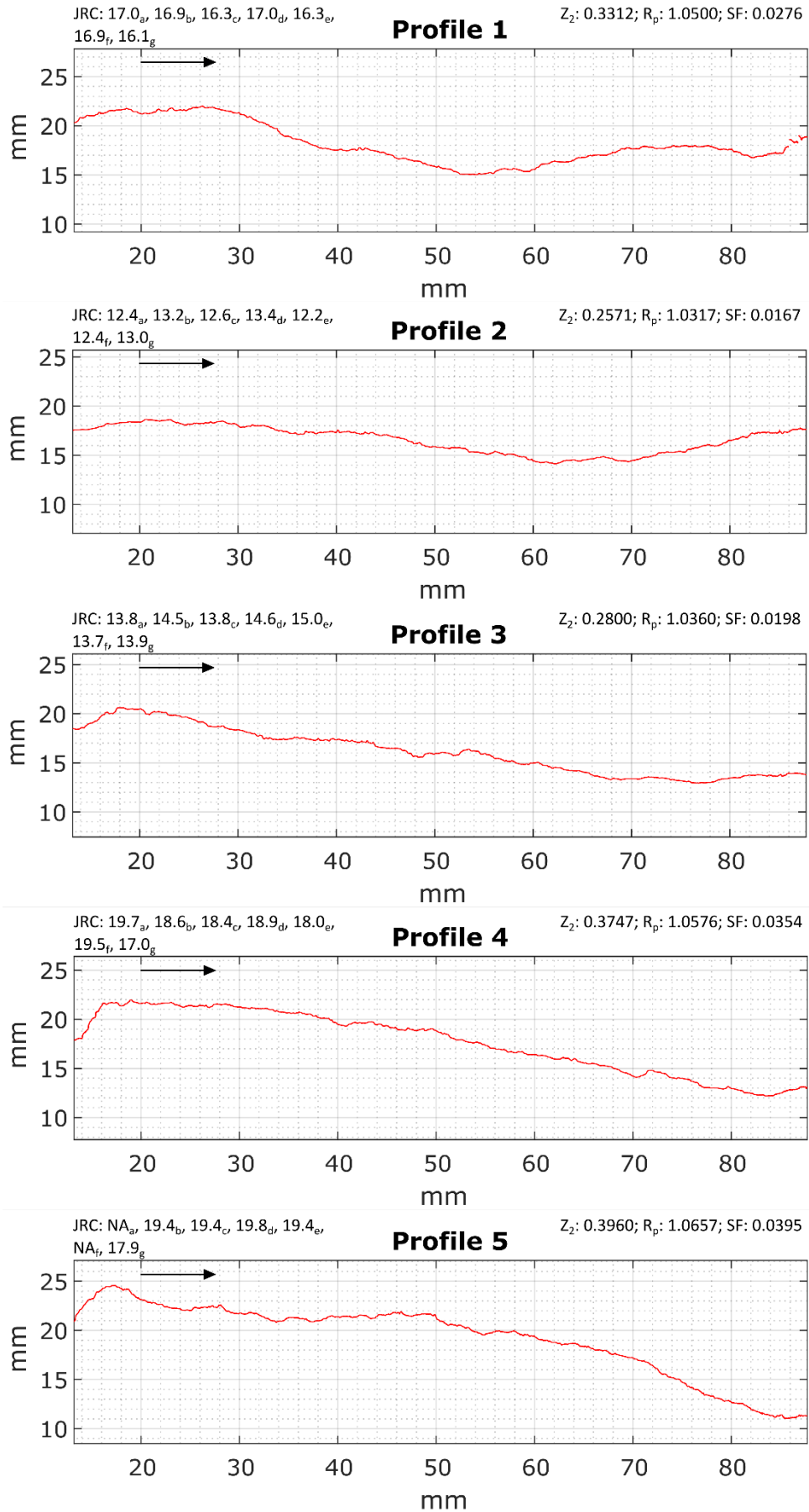


FIGURE 51: SB1 PROFILES BOTTOM

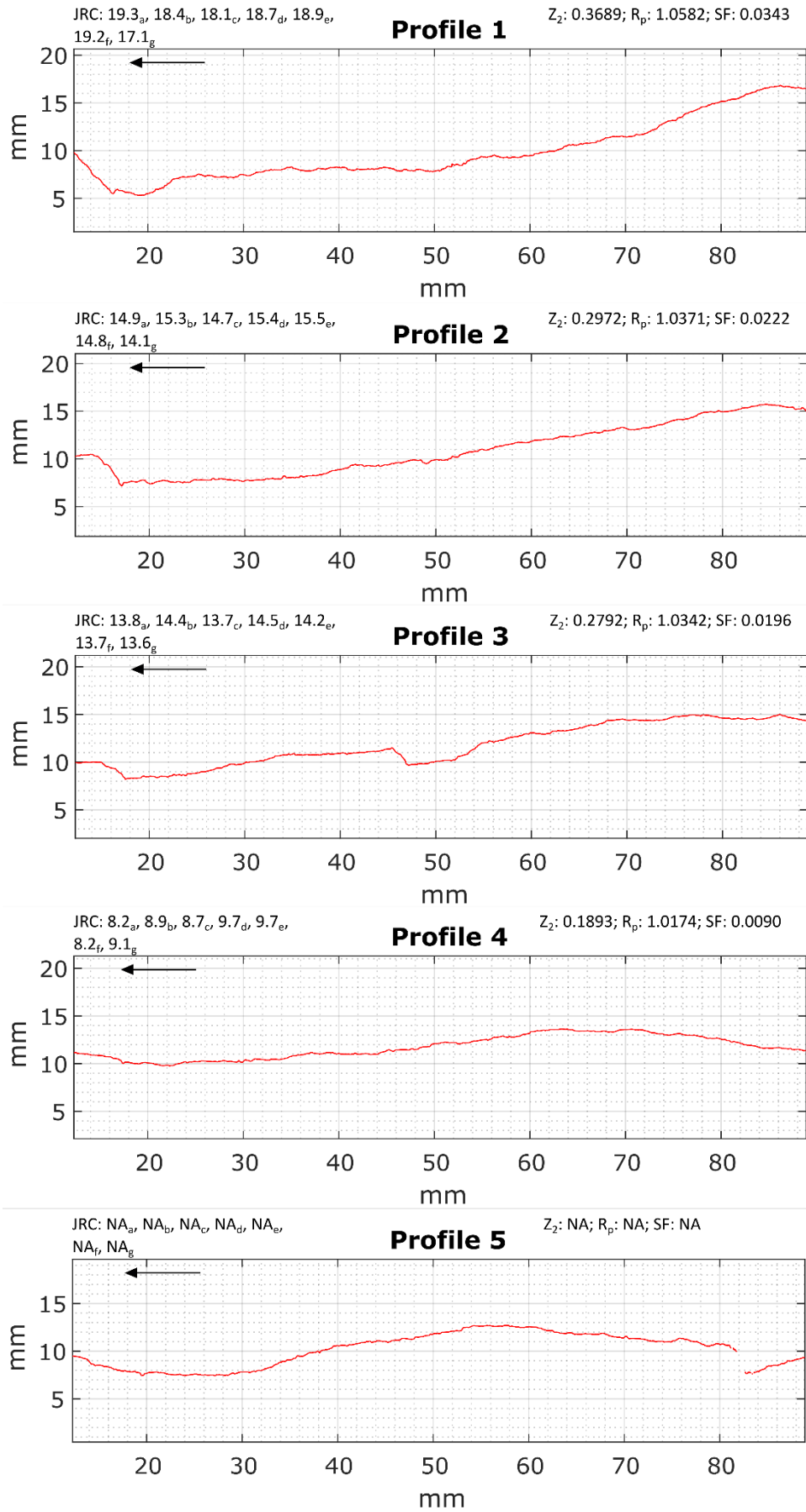


FIGURE 52: SB1 PROFILES TOP

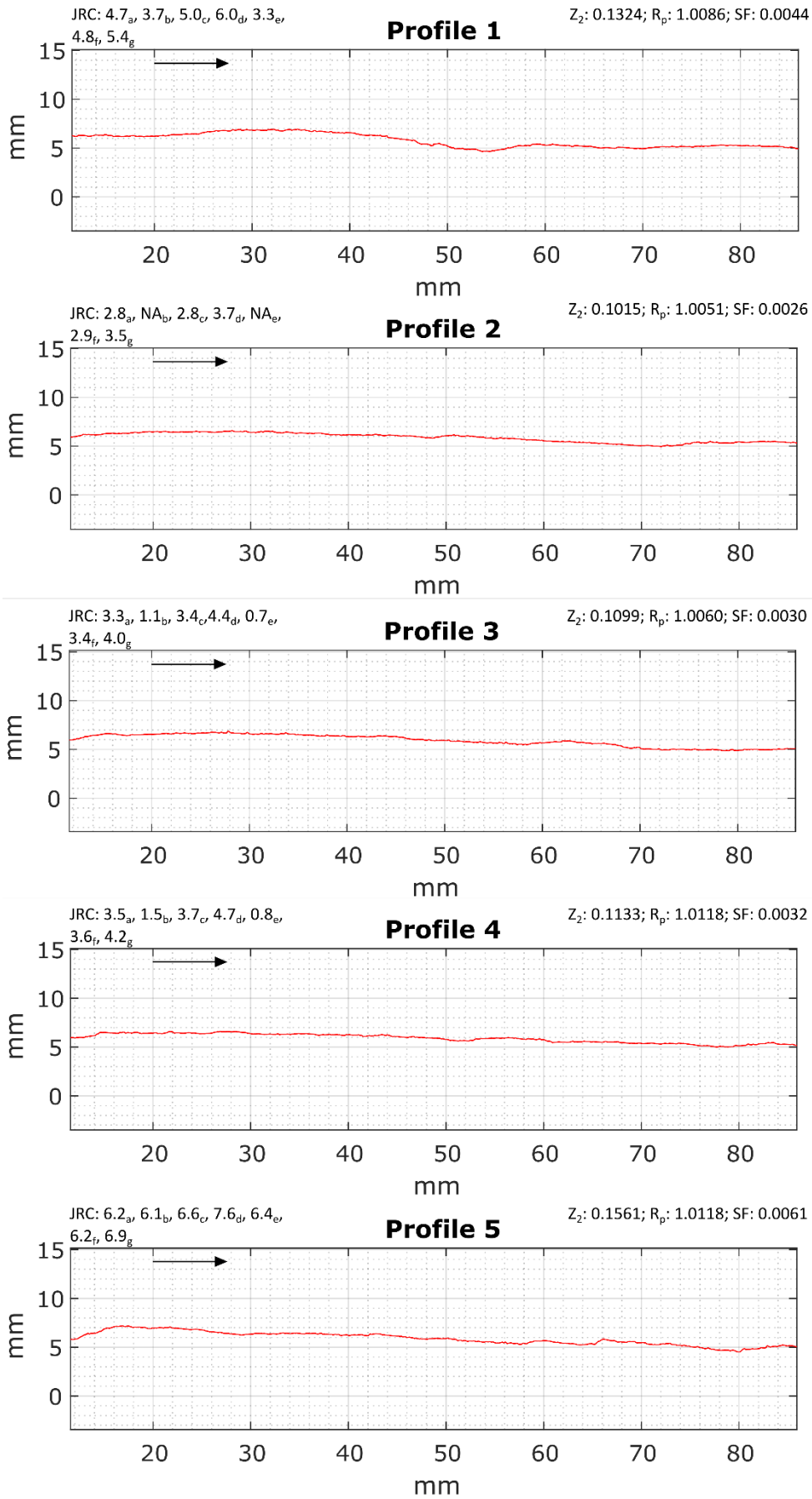


FIGURE 53: SB2 PROFILES BOTTOM

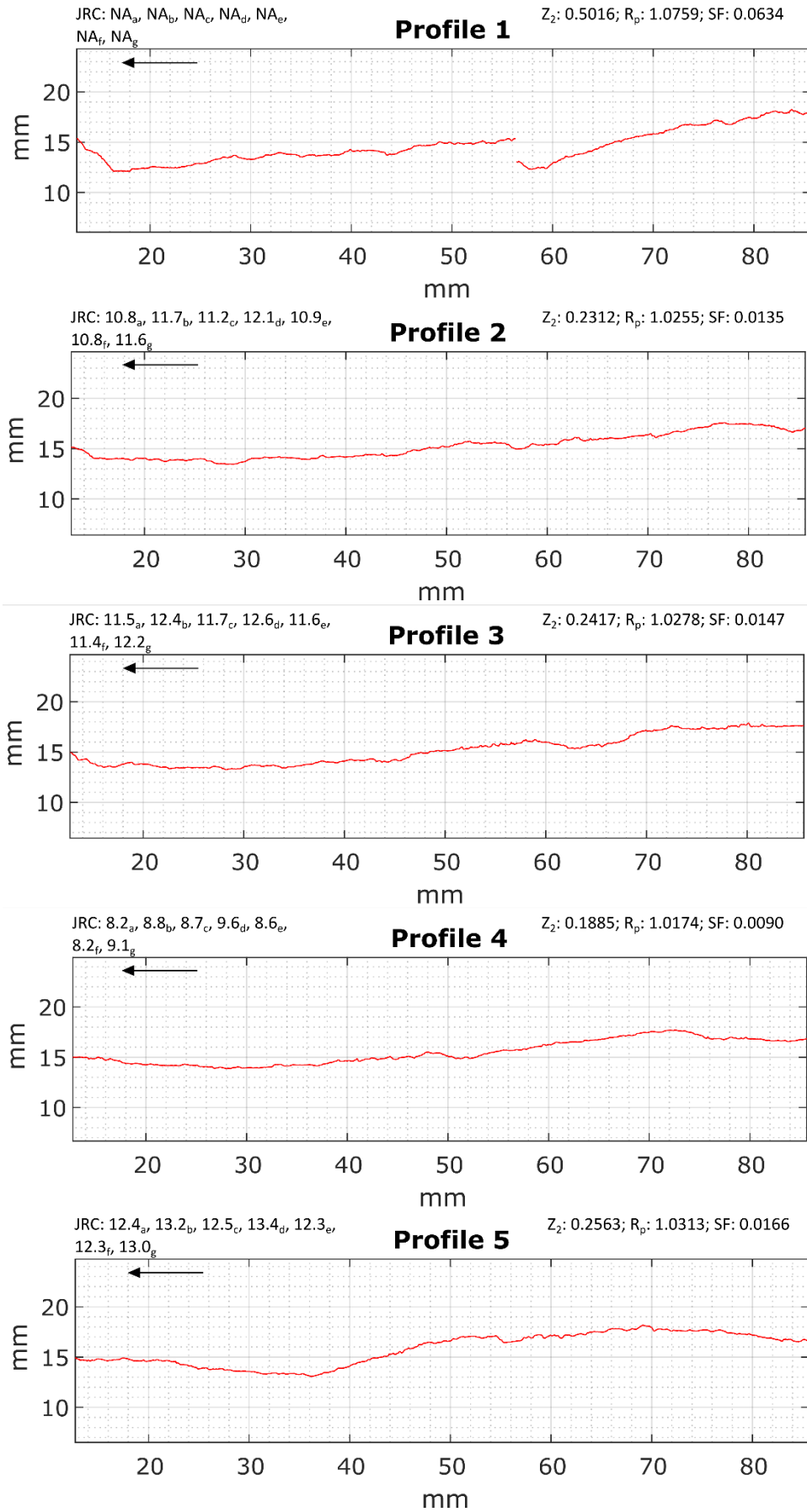


FIGURE 54: SB2 PROFILES TOP

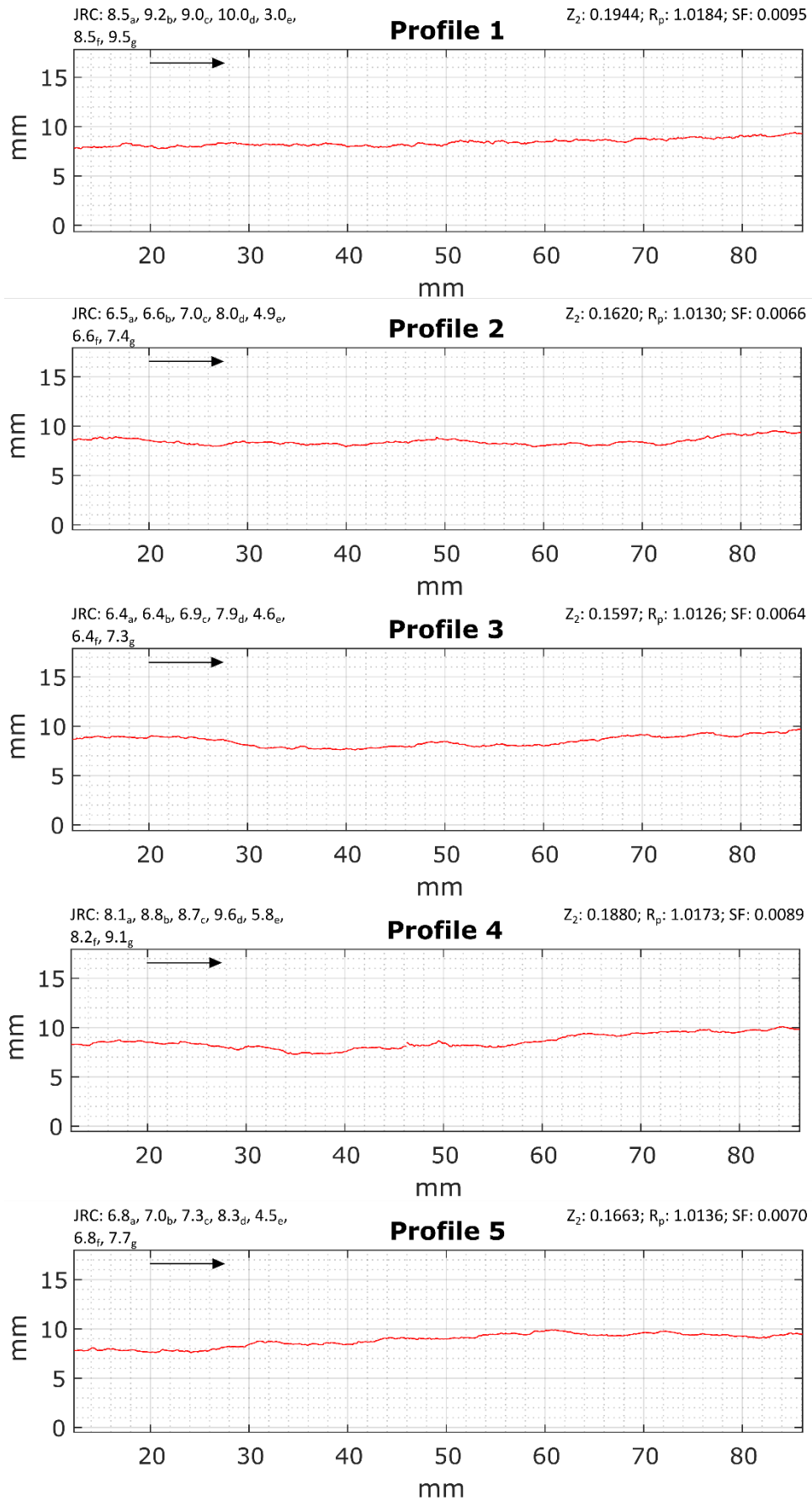


FIGURE 55: SB3 PROFILES BOTTOM

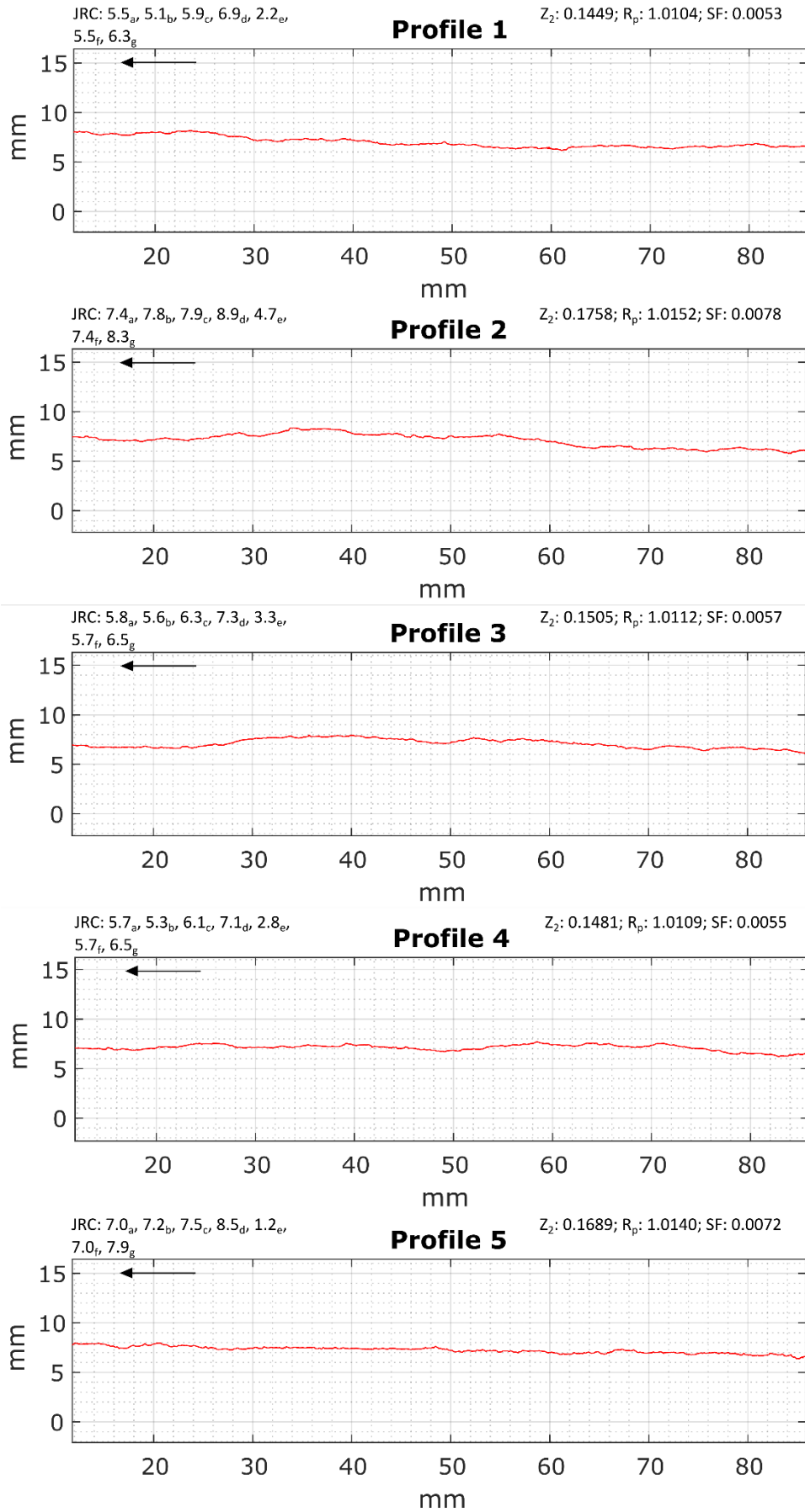


FIGURE 56: SB3 PROFILES TOP